Naval Research Laboratory

Stennis Space Center, MS 39529-5004

NRL/MR/7320--12-9423

Validation Test Report for the Coupled Ocean/Atmosphere Mesoscale Prediction System (COAMPS) Version 5.0: Ocean/Wave Component Validation

Richard A. Allard
Travis A. Smith
Tommy G. Jensen
Philip Y. Chu
Erick Rogers
Timothy J. Campbell

Ocean Dynamics and Prediction Branch
Oceanography Division

Uriah M. Gravois

University of Florida
Gainesville, Florida

Suzanne N. Carroll
Kim Watson

QinetiQ North America
Stennis Space Center, Mississippi

December 31, 2012

REPORT DOCUMENTATION PAGE

Form Approved
OMB No. 0704-0188

1. REPORT DATE *(DD-MM-YYYY)*	2. REPORT TYPE	3. DATES COVERED *(From - To)*
31-12-2012	Memorandum Report	

4. TITLE AND SUBTITLE

Validation Test Report for the Coupled Ocean/Atmosphere Mesoscale Prediction System (COAMPS) Version 5.0: Ocean/Wave Component Validation

5a. CONTRACT NUMBER

5b. GRANT NUMBER

5c. PROGRAM ELEMENT NUMBER
0602435N

6. AUTHOR(S)

Richard A. Allard, Travis A. Smith, Tommy G. Jensen, Philip Y. Chu, Erick Rogers, Timothy J. Campbell, Uriah M. Gravois,[1] Suzanne N. Carroll,[2] and Kim Watson[2]

5d. PROJECT NUMBER

5e. TASK NUMBER

5f. WORK UNIT NUMBER
73-4320-02-5

7. PERFORMING ORGANIZATION NAME(S) AND ADDRESS(ES)

Naval Research Laboratory
Oceanography Division
Stennis Space Center, MS 39529-5004

8. PERFORMING ORGANIZATION REPORT NUMBER

NRL/MR/7320--12-9423

9. SPONSORING / MONITORING AGENCY NAME(S) AND ADDRESS(ES)

Office of Naval Research
One Liberty Center
875 North Randolph Street, Suite 1425
Arlington, VA 22203

10. SPONSOR / MONITOR'S ACRONYM(S)

ONR

11. SPONSOR / MONITOR'S REPORT NUMBER(S)

12. DISTRIBUTION / AVAILABILITY STATEMENT

Approved for public release; distribution is unlimited.

13. SUPPLEMENTARY NOTES

[1]University of Florida, Gainesville, FL
[2]QinetiQ North America, Stennis Space Center, MS 39529

14. ABSTRACT

The ocean-wave component of the Coupled Ocean/Atmosphere Mesoscale Prediction System (COAMPS) has been validated for four test cases: (1) Hurricane Ivan, (2) Okinawa Trough, (3) Florida Straits, and (4) Adriatic Sea. Wave properties including the Stokes Drift Current, wave radiation stress and enhancement of bottom drag are passed from the wave to ocean model NCOM. The ocean model passes surface currents and water levels to the wave model SWAN. Ocean-wave coupling shows improvement and better model predictability in winds, waves, sea surface temperature, currents, sonic layer depth and associated acoustic properties. Comparisons to in situ measurements showed improved wave predictions when surface currents were included. Current-wave model interaction showed substantial improvements in high-wind conditions. The long-term test cases successfully demonstrated the capability of operational COAMPS and ESMF coupler functionality, both in model accuracy and system robustness for operational implementation.

15. SUBJECT TERMS

Model coupling
Waves
Currents
Earth System Modeling Framework

16. SECURITY CLASSIFICATION OF:			17. LIMITATION OF ABSTRACT	18. NUMBER OF PAGES	19a. NAME OF RESPONSIBLE PERSON
a. REPORT	b. ABSTRACT	c. THIS PAGE			Richard A. Allard
Unclassified Unlimited	Unclassified Unlimited	Unclassified Unlimited	Unclassified Unlimited	99	19b. TELEPHONE NUMBER *(include area code)* (228) 688-4894

Standard Form 298 (Rev. 8-98)
Prescribed by ANSI Std. Z39.18

TABLE OF CONTENTS

FIGURES AND TABLES

1.0 INTRODUCTION

A growing understanding of the impacts that large and small scale ocean and atmospheric events (El Niño, hurricanes, etc.) have on weather forecasting has led to the coupling of the Coupled Ocean Atmosphere Mesoscale Prediction System (COAMPS™[1]) model to the Navy Coastal Ocean Model (NCOM) Version 4.0 and the wave models SWAN (Simulating WAves Nearshore) and WAVEWATCH III (WW3™). In a fully coupled mode, COAMPS, NCOM, and SWAN (or WW3) may be integrated concurrently so that currents and water levels, wave-induced stress, bottom drag, Stokes drift current, precipitation, and surface fluxes of heat, moisture, and momentum are exchanged across the air-sea or sea-wave interface. This coupling is facilitated through the Earth System Modeling Framework (ESMF).

The COAMPS system incorporates meteorological observations such as radiosondes, ship reports, and satellite data with ocean observations that provide time-dependent global oceanographic lateral boundary conditions (LBCs) from the Navy Operational Global Atmospheric Prediction System (NOGAPS) (Hogan and Rosmond 1991). Ocean observations are derived from global NCOM, and bathymetry for COAMPS comes from the Digital Bathymetric Data Base, resolution 2-min (DBDB2), unless otherwise noted. Atmospheric, oceanic, and wave forecast output includes surface and upper-air fields, sea surface temperature (SST), three-dimensional (3D) ocean temperature, salinity, velocity, mixed layer depth, acoustic products, significant wave height (SWH), wave period, and wave spectrums. These validation tests primarily focus on the dynamics of wave interaction with near surface ocean currents and the concomitant wave field response to ocean dynamics. Atmospheric data assimilation is achieved through the NRL Atmospheric Variational Data Assimilation System (NAVDAS, Daley and Barker, 2000, 2001)) and ocean data assimilation is facilitated through the Navy Coastal Ocean Data Assimilation (NCODA) 3DVAR system (Cummings, 2005), (Smith, 2011).

The purpose of this document is to build upon the previous atmosphere/ocean Validation Test Report (VTR) (Allard et al., 2010) by evaluating the performance of COAMPS with the additional coupling of the wave component. The focus of the validation testing is to assess ocean/wave coupling rather than ocean/wave feedback to the atmosphere (i.e., the atmospheric model provides forcing to NCOM and SWAN/WW3 but feedback from the wave models is not evaluated). Full 5-way coupling of the models (minus wave to atmospheric feedback) is performed, while "uncoupled runs" have no ocean-to-wave or wave-to-ocean feedback.

[1] COAMPS® is a registered trademark of the Naval Research Laboratory.

Manuscript approved June 19, 2012.

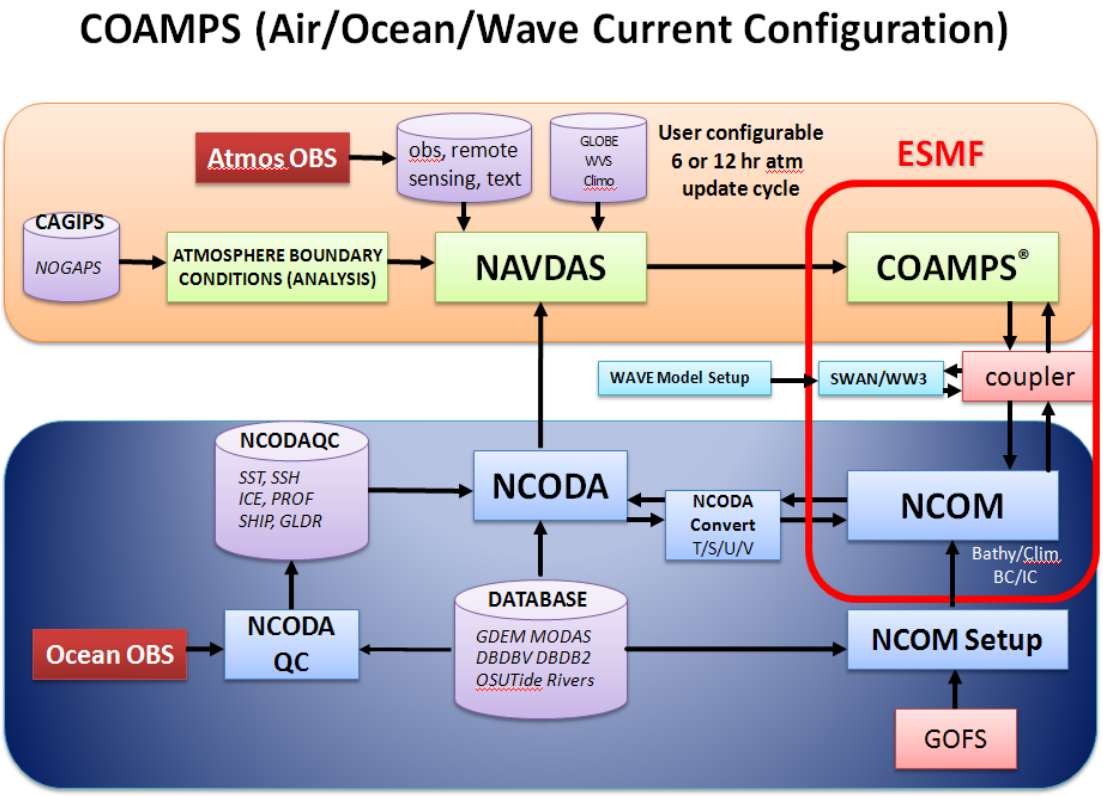

Figure 1: COAMPS flow of execution for the air/ocean/wave configuration.

2.0 MODEL DESCRIPTIONS

2.1 Coupled Ocean/Atmosphere Mesoscale Prediction System (COAMPS)

The Naval Research Laboratory (NRL) Marine Meteorology Division's COAMPS model makes both microscale and mesoscale predictions of the ocean and atmosphere. The COAMPS atmospheric components are used operationally by the U.S. Navy for numerical weather prediction in many regions around the world.

The COAMPS atmospheric model is a finite-difference approximation to the fully compressible, nonhydrostatic equations. Surface fluxes are calculated through the Louis et al. (1979) and Fairall et al. (1996) formulations, according to the Monin-Obukhov similarity theory. The surface energy budget is parameterized through a force-restore method. The Kain and Fritsch (1990) approach is used to parameterize subgrid-scale moist convective processes. The grid-scale evolution of the moist processes is explicitly predicted from budget equations for rain, snow, water vapor, cloud water, and cloud ice (Rutledge and Hobbs 1983). Short- and long-wave radiation processes are parameterized through following Harshvardhan et al. (1987), with an option for a four stream technique following Fu and Liou (1993). In this study, the Fu and Liou radiation scheme is used exclusively. Free-atmospheric turbulent mixing and diffusion and the planetary boundary-layer are modeled using a prognostic equation for the turbulent kinetic energy budget from the Mellor and Yamada (1982) level 2.5 formulation. COAMPS can use an arbitrary number of terrain following vertical levels, but in these tests, COAMPS employs 30-60 vertically-stretched levels.

COAMPS has two data atmospheric assimilation options: the 3D MVOI system and NAVDAS, the three-dimensional variational analysis scheme. Each option includes data analysis and quality control, initialization, and forecast model components (Hodur, 1997; Chen et al., 2003; Daley and Barker, 2000, 2001). Since NAVDAS has been fully evaluated as a viable data assimilation system (Goerss et al., 2003) and has shown improvement over MVOI, NAVDAS is utilized for all the VTR case studies, Data assimilation is initiated by the prior 12 hr forecast and incorporates quality-controlled observations from radiosondes, aircraft, ship, satellite, and surface stations. Both in situ and satellite SST measurements are used in the NAVDAS analysis (Cummings, 2005). COAMPS includes a globally relocatable grid, nested grids, user-defined grid resolutions and dimensions, an option for idealized or real-time simulations, and code that allows portability between mainframes and workstations (Smith et al., 2012).

COAMPS-TC, a modeling option in COAMPS, allows for realistic representations of tropical cyclones. The NAVDAS 3DVAR atmospheric assimilation system contains a tropical cyclone bogusing technique to ingest wind, wind radii, and pressure data provided by the National Hurricane Center and Joint Typhoon Warning Center for an existing tropical cyclone in the Atlantic, Eastern, or Western Pacific basins.

2.2 Navy Coastal Ocean Model (NCOM)

The Navy Coastal Ocean Model (NCOM) Version 4.2 was developed primarily from two existing ocean circulation models, the Princeton Ocean Model (POM) (Blumberg and Mellor 1983; 1987) and the Sigma/*Z*-level Model (SZM) (Martin et al., 1998). NCOM (Martin, 2000) has a free-surface and is based on the primitive equations and hydrostatic, Boussinesq, and incompressible approximations. The vertical mixing is parameterized by the Mellor Yamada Level 2 (MYL2) and MYL2.5 turbulence models. The vertical mixing enhancement scheme of Large et al. (1994) is used for parameterization of unresolved mixing processes occurring at near-critical Richardson numbers. A source term included in the model equations allows for river input and runoff inflows.

As in POM, NCOM employs a staggered Arakawa C grid. Spatial finite differences are mostly second-order centered, but higher-order spatial differences are optional. NCOM features a leapfrog temporal scheme with an Asselin filter to suppress timesplitting. Most terms are handled explicitly in time, but surface wave propagation and vertical diffusion are implicit.

NCOM has an orthogonal-curvilinear horizontal grid and a hybrid sigma and *z*-level grid (Barron et al., 2006) with sigma coordinates applied from the surface down to a designated depth. Level coordinates are used below the specified depth. The second vertical grid choice is the general vertical coordinate (GVC) grid consisting of a three-tiered structure. The GVC grid is comprised of: (1) a near-surface "free" sigma grid that expands and contracts with the movement of the free surface, (2) a "fixed" sigma, and (3) a *z*-level grid allowing for "partial" bottom cells (Martin et al., 2008a,b). A relocatable version of NCOM, called RELO NCOM, is used to generate namelists and grids of NCOM parameters.

2.3 Simulating WAves Nearshore (SWAN) Model

The Simulating WAves Nearshore (SWAN) model is a phase-averaged system based on the spectral action balance equation, treated in discrete form. It is a third-generation model capable of characterizing coastal zones with shallow water, (barrier) islands, tidal flats, local winds, and ambient currents. It performs best when predicting wave conditions in small scale, but is applicable at any scale. SWAN can also accommodate short-crested, random wave fields propagating at the same time from vastly differing directions. It accounts for wave generation due to wind, energy dissipation due to whitecapping, shoaling and refractive propagation (both depth and current induced), bottom friction and depth-induced wave breaking, and nonlinear wave-wave interactions. SWAN can be stationary or non-stationary and is formulated in Cartesian or spherical coordinates. The stationary mode is used only for waves with a comparatively short residence time in the computational area. In other words, wave travel time through the region is minimal compared to the time scale of the geophysical conditions such as wave boundary conditions, tides, wind, and storm surge. A quasi-stationary approach is used with stationary SWAN computations in a time-varying sequence of stationary conditions (SWAN team, 2006).

2.4 Earth System Modeling Framework (ESMF)

COAMPS, NCOM, and SWAN (or WW3) are integrated together through the ESMF. With funding from the Department of Defense and the National Aeronautics and Space Administration (NASA), ESMF was developed by the National Center for Atmospheric Research (NCAR). It was designed to create a flexible, high-performance software infrastructure that was easy to use and featured portability, interoperability, and reuse in climate, data assimilation, numerical weather prediction, and other Earth science applications. The software infrastructure allows various weather, climate, and data-assimilation components to work together on an array of platforms, from laptops to supercomputers. ESMF software is component-based, coupling models together as collections of smaller elements. A component may be a physical domain or a function, such as a coupler or I/O (input/output) system. The framework provides tools for re-gridding, data decomposition, and communication on parallel computers, as well as for common modeling functions. ESMF allows for the passing of variables between ocean and atmosphere in memory and organizes horizontal interpolation between the fields in the different components.

COAMPS passes variables from one model to the other by means of an exchange grid. Bulk fluxes of heat and momentum are calculated on the exchange grid and interpolated back to the model nests. The exchange grid is the resolution of the finest mesh grid. The graphic below depicts most of the variables being passed to and from each model.

All model parameter exchanges were facilitated via the ESMF coupler. Figure 2 represents the ESMF coupler wiring diagram showing the exchange parameters among models.

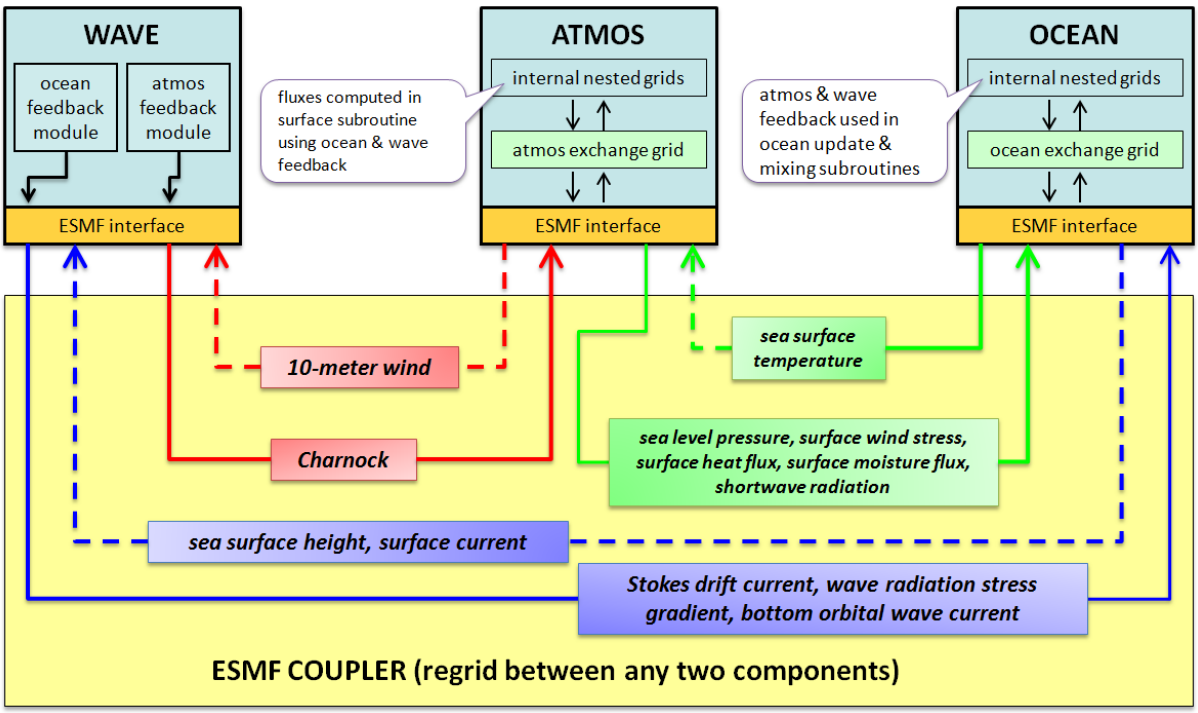

Figure 2: ESMF coupling frame for the COAMPS system and the variables passed between the coupled models.

2.5 Wave-Ocean Coupling

In the forecasting of the battlespace environment, two-way coupling between wave, ocean, and atmospheric models has become a primary navy focus, as it is expected to offer a much more realistic representation of relevant physical processes than can be obtained through traditional one-way coupling. Although waves play a critical role at the air-sea interface, current navy operational forecasting outside the surf zone generally disregards wave model outputs in the computations of the atmospheric and ocean models. This is largely due to the fact that operational two-way coupling presents a number of substantial technical and scientific challenges, such as efficiently transferring data between models running on different spatial grids and with different time steps.

Wave forcing can impact the ocean circulation and associated currents due to the following mechanisms: 1) Stokes drift current (SDC) in which a particle floating at the free surface experiences a net drift velocity in the direction of wave propagation; 2) wave radiation stress due to the horizontal gradients of the energy of surface waves, 3) enhancement of bottom drag in shallow water due to wave orbital motions near the bottom, and 4) waves causing enhanced vertical mixing due to Langmuir cells (LCs) and Langmuir turbulence in the presence of moderate to strong winds (Kantha and Clayson, 2004; McWilliams et al., 1997). All these effects have been incorporated into NCOM version 4.1. NCOM can be run in a standalone mode reading wave input fields from file or as part of the ESMF-based COAMPS in which these forcing fields are passed from SWAN to NCOM.

SDC causes ocean current speeds to increase, but enhanced vertical mixing in the surface mixed layer (increased shear) will decrease currents. The SDC also tends to increase bottom stress. Ocean model water levels can modify the water depth used in wave model calculations. Surface currents ingested by the wave model alter the effective wind speed (wind speed relative to a frame of reference moving with the currents) and produce conservative (kinematic) effects on the wave field analogous to refraction and shoaling produced by depth variations. Horizontal shear in the currents can generate non-conservative effects such as wave propagation from a zero current area to one with opposing currents. The propagating waves may steepen, break more frequently, or be blocked, resulting in persistent breaking at the blocking location. This affects source/sink terms in deep water. Lastly, Doppler shifting has implications for comparisons to data from fixed instruments. Current vertical structure is not used by the wave model. The coupled model system uses the surface currents as representative of the entire vertical range (typically the upper 200 m).

Wave-to-ocean coupling requires modification of the ocean model code. This coupling involves three distinct mechanisms. First, the bottom drag is enhanced by the waves (Grant and Madsen 1979) requiring computation of variables controlling the wave orbital velocity at the bottom. Second, the radiation stress tensor is calculated from the wave field, with the gradients of these tensors used to calculate the local momentum surplus (or deficit), which is provided to the ocean model as a surface stress (Longuet-Higgins and Stewart; 1962, 1964). The third mechanism for wave-to-ocean coupling is through Stokes drift. Stokes drift is computed at every wave model grid point using an integration that considers spectral energy densities,

spectral component wavelengths, and vertical position (Tang et al. 2007). Momentum related to Stokes drift is carried in the wave field and is not associated with the mean Eulerian flow (Ardhuin et al. 2004, 2008). Therefore, the Stokes drift current (SDC) is *not* included in the ocean model prognostic momentum variables but *is* included in computations requiring the observable mean flow, including a) advection of model fields, b) vertical velocity, c) the Coriolis term, d) bottom drag, and e) vertical mixing in the surface mixed layer.

2.6 Ocean-wave coupling and SWAN sensitivity to wave dissipation and drag coefficient

Rogers et al. (2011) introduced observation-based wind input and whitecapping source terms based on earlier work by Donelan et al. (2006), Babanin and Young (2005), Young and Babanin (2006), Tsagareli (2009), Tsagareli et al. (2010), and Babanin et al. (2010). These source terms were adapted and improved for practical application and implemented in SWAN. The wind input source terms in the new parameterization (henceforth referred to as the "Babanin" parameterization) are taken directly from the observational work of Donelan et al. (2006) in high-wind conditions over Lake George, Australia and modified to scale with the friction velocity, u*, and a physical constraint on the total stress. The new dissipation function is observation-consistent insofar as it conforms to two features of dissipation in the real ocean, as reported in the literature during the past decade. The first feature has a two-phase dissipation, for waves of any particular frequency, either due to 1) the instability (and breaking) of waves of that frequency or 2) the destabilization by larger breaking waves (e.g. through turbulence). The second feature creates a wave breaking threshold such that when the local spectral density falls below a spectral threshold no breaking occurs at that frequency. These two features were only recently included together in any numerical model (in Tsagareli 2009 in an academic model and in Ardhuin et al. 2010 in WW3™). Both features contrasted sharply with earlier dissipation terms (e.g. Komen et al. 1984, WAMDI Group 1988, Booij et al. 1999), where all waves are considered breaking at all times and every wave system affects the strength of dissipation of all other systems in a physically implausible manner (Rogers et al. 2003).

As stated above, an evaluation of u* in high-wind conditions is necessary to work in tandem with the new Babanin wave input and dissipation parameterization. The evaluation of u* based on the 10 m wind (U_{10}) input requires the specification of a 10 m ocean surface drag coefficient (C_{10}). There are many formulations of the ocean surface drag coefficient reported in literature, and Figure 3 represents several investigators' u* calculations based on their C_{10} equations (e.g. Wu 1980, Powell et al. 2003, Powell and Ginis 2006). The u* term is calculated through the definition of wind stress, $u^* = \sqrt{C_{10} U_{10}^2}$.

Early C_{10} estimates from Wu (1980) showed u* monotonically increasing with increasing U_{10} based on data collected from 33 experiments under neutral stability for open ocean conditions. However, based upon these experiments C_{10} in high-wind conditions (greater than 30 m s^{-1}) was only hypothetical. In fact, SWAN utilizes the C_{10} formulation from Wu (1980) in the current version. Since the Wu (1980) experiments, it has been observed that C_{10} displays a saturation trend with a subsequent decrease in magnitude for wind speeds greater than 30 m s^{-1} based on field experimentation. Field studies in tropical cyclone conditions (Powell et al. 2003, Jarosz et. al 2007, Sanford et al. 2011) have shown that u* has a tendency to asymptote at a u*

value approximately equal to or less than 2 m s^{-1} (Figure 3.1-5) and even decrease slightly for winds greater than 50 m s^{-1}. Hwang (2011) formulated an empirical equation to capture the saturation and decaying behavior of C_{10} in high-wind conditions based on observations from Felizardo and Melville (1995), Powell et al. (2003), and Jarosz et al. (2007),

$$C_{10} = 10^{-4}(-0.0160U_{10}^2 + 0.967U_{10} + 8.058). \quad (1)$$

The resultant calculation for u* based upon the Hwang formulation for C_{10} is represented in Figure 3 (aqua line). In this study, the Hwang (2011) formulation for C_{10} is tested in SWAN as well as the classic Wu (1980) formulation; however, the rapid decrease of u* to 0 for U_{10} > 68 m s^{-1} in the Hwang formulation has never been verified; therefore, u* is capped here at its maximum value of approximately 2 m s^{-1} for U_{10} > 50 m s^{-1} (Figure 3, hatched magenta line).

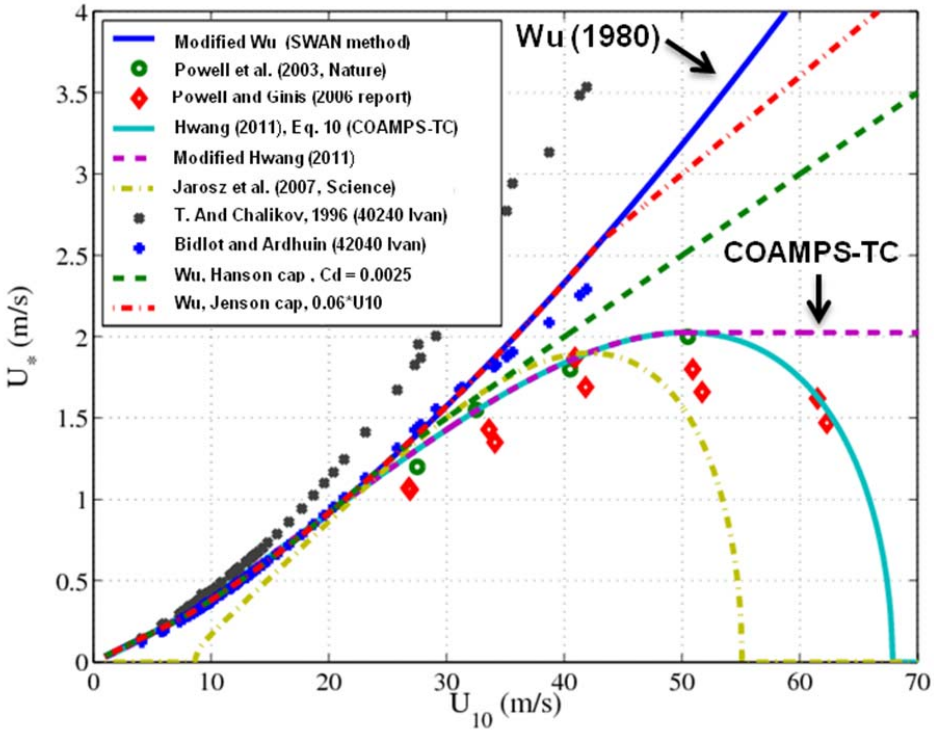

Figure 3: The friction velocity, u*, as a function of 10 m wind, U_{10}, based on ocean surface drag coefficient formulations, C_{10}, from several investigators and observational data studies (Powell et al., 2003 (green circles); Powell and Ginis, 2006, (red diamonds), Jarosz et al., 2007 (yellow dashes), Wu 1980 (blue line), Bidlot (2007) and Ardhuin (2009), (blue crosses), and Tolman and Chalikov (not published, gray Xs)).

The Babanin wave source terms and the modified Hwang drag formulation in SWAN were implemented in COAMPS-TC to test its effectiveness in a severe TC wind event and to investigate the sensitivity of SWAN compared to the first generation Komen wave source terms and Wu drag formulation. Figure 4 shows the results of sensitivity testing of the maximum SWH in the wave grid domain for Hurricane Ivan based on the classic and new SWAN wave

source terms and drag coefficient. Three simulations were tested: 1) Komen-Wu NCOM/SWAN uncoupled (KWunc), 2) Babanin-Hwang NCOM/SWAN uncoupled (BHunc), and 3) Babanin-Hwang NCOM/SWAN coupled (BHcpl). The maximum intensity of Hurricane Ivan for each of the aforementioned sensitivity tests are very comparable, while the forecast tracks were nearly identical to the forecast track shown in Figure 3.1-2. Upon immediate inspection, a 5-6 m difference in the maximum SWH between the KWunc and BHunc simulations is present. The implementation of the Babanin wave source terms, and more importantly, the reduced drag coefficient formulation produces a SWH result that is much more consistent with observations.

Ocean to wave coupling, i.e., passing water levels and currents to SWAN, is important in several ways. First, water levels can modify the water depth used in wave model calculations. Also, surface currents ingested by the wave model alter the effective wind speed (wind speed relative to a frame of references moving with the currents) and produce conservative or kinematic effects on the wave field analogous to refraction and shoaling produced by depth variations. Lastly, horizontal shear in the currents can generate non-conservative effects such as wave propagation, which may steepen, break more frequently, or be blocked, producing persistent breaking at the blocking location. These phenomena ultimately affect the wave model source/sink terms, especially in deep water. The addition of ocean to wave coupling (BHcpl) in COAMPS-TC acted to primarily reduce the maximum SWH throughout the forecast track of Hurricane Ivan (see Sec. 3.1) by an additional 1-2 m (Figure 4) in the presence of winds greater than 50 m s^{-1}. It is important to note that the grid point of maximum SWH in the BHunc simulation is not the same grid point of maximum SWH in the BHcpl simulation; however, a general decrease in maximum SWH between the KWunc and BHcpl simulations is on the order of 7-8 m in the sensitivity tests.

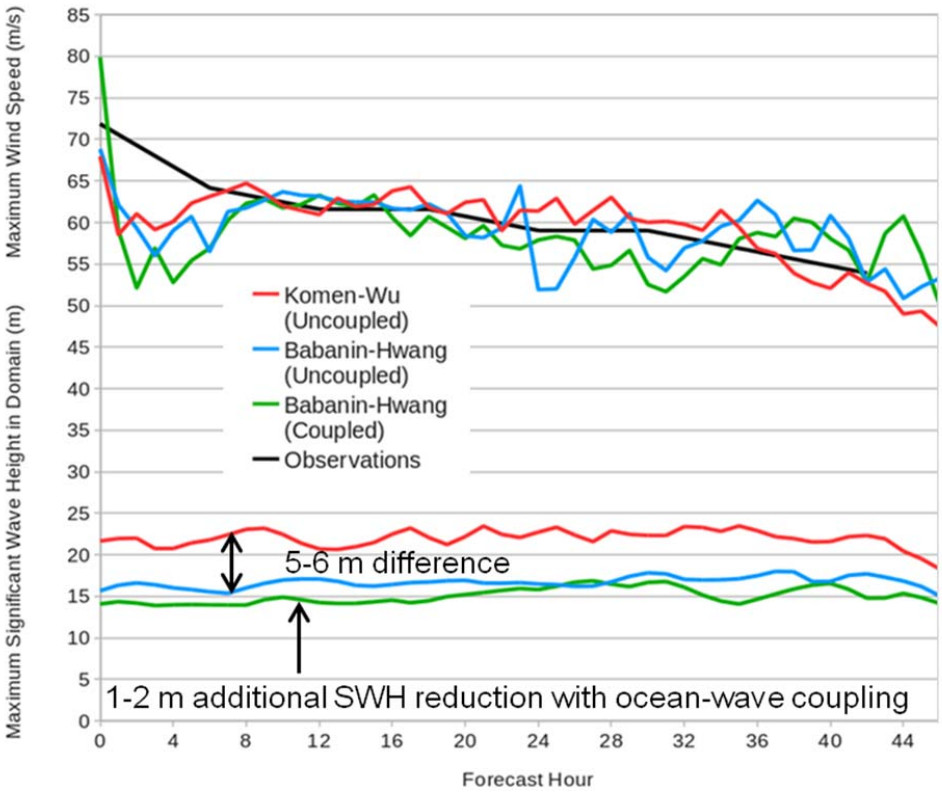

Figure 4: Maximum TC intensity and maximum SWH time series are illustrated for several SWAN sensitivity tests. Sensitivity tests include a combination of both Komen and Babanin wave input and dissipation parameterizations and Wu (1980) and Hwang (2011) surface ocean drag formulations. For this study, three sensitivity tests, Komen-Wu uncoupled (KWunc, red), Babanin-Hwang uncoupled (BHunc, blue), and Babanin-Hwang coupled (BHcpl, green) were completed. The first 48-hours of the 12 UTC September 2004 72-hour forecast are plotted.

2.7 Document Overview

This report details the procedures and results of validating the coupled air/ocean/wave COAMPS system. A description of the purpose of each test, the test area characteristics, model run specifics, and results from each simulation will be presented here, along with graphical output, statistics, and concluding remarks. The user can refer to the COAMPS Version 5.0 User's Guide (Smith et al., 2010), NCOM 4.0 User's Manual and Software Design Description (Barron et al., 2006 and Martin et al., 2008 a, b) and the COAMPS Version 3 Model Description (Chen et al., 2003; http://www.nrlmry.navy.mil/coamps-web/web/docs) for further information on the individual models. An online version of the ESMF User's Guide is available at http://www.earthsystemmodeling.org/esmf_releases/public/last/ESMF_usrdoc/ESMF_usrdoc.html. For NCOM, see Barron et al. (2006) and Martin et al. (2008a). For NCODA, see Cummings and Carroll, 2006. For SWAN, see the SWAN Technical Document (2010) at http://iod.ucsd.edu/~falk/modeling/swantech.pdf. WAVEWATCH III documentation may be found at http://polar.ncep.noaa.gov/mmab/papers/tn276/MMAB_276.pdf.

3.0 VALIDATION TEST DESCRIPTIONS AND RESULTS

The COAMPS has been validated and verified successfully for a number of field cases. This test report concerns the evaluation of ocean/wave coupling only, excluding wave effects on the atmosphere. The atmospheric model is used solely for wind forcing on the ocean and wave models with no wave feedback to the atmosphere. A fully coupled COAMPS run for this VTR will consist of a 5-way coupled atmosphere/ocean/wave run (without wave to atmosphere feedback). Table 1 below provides a summary of test specifications.

Table 1: Test case characteristics.

Test Case	Area/ Program	Lat/Lon	Key Processes	Grid Res.	Time Frame	Obs. Data
1	Hurricane Ivan	0.0°N to 38°N, 65°W to 108 °W	Ocean current impacts on waves and vv.	Atm: 18, 6, 2 km Ocean: 4 km Wave: 8 km	9/01-9/17 2004	Ship ADCPs, SRA flight data, buoy data, GOES-12 satellite imagery
2	Okinawa Trough	17-34 °N, 118-134°E	Strong currents, large tides, steep bathy	Atm: 27 km Ocean: 3 km Wave: 9 km	8/1-10/31 2007	GTS altimetry T&S, ENVISAT SSTs, gliders, AXBTs.
3	Florida Straits	80.8 to 78.8°W and 23.6 to 27.2°N	Strong current impacts on waves.	Atm: 18, 6, 2 km Ocean: 3, 1 km, SWAN: 1 km, WW3: 0.5° and 6.5 km	3/1-5/18 2005	Wellen HF Radar, CMAN buoy, NOS tides, ADCPs
4	Adriatic Circulation Experiment (ACE) 2003 and 2006	43.5°N to 46.0°N, 12.0°E to 15.0°E	Bora winds, ocean eddy response, and wave response.	2003: Atm: 36, 12, 4 km; Ocean: 6, 2 km; Wave: 2 km 2006: Atm: 3km Ocean: 1km Wave: 1 km	2/1-2/21 2003; 3/1-9/30 2006	Ship ADCPs, current meters, drifters, coastal and oil platform met stations, wave data.

3.1 Test Case 1: Hurricane Ivan using COAMPS-TC

3.1.1 Purpose

This study utilizes the tropical cyclone version of COAMPS (COAMPS-TC) (Doyle et al. 2012) to simulate the ocean/wave model interactions in high-wind TC conditions for Hurricane Ivan as it traversed the Gulf of Mexico in September of 2004. New SWAN wave input and dissipation source terms based on high-wind conditions (Donelan et al. 2006, Babanin et al. 2010, Rogers et al. 2011) from observations (Young et al. 2005, Donelan et al. 2006, Babanin

et al. 2007a) are tested in TC conditions, as well as a new formulation of the ocean surface drag coefficient in SWAN that is also based on observations (Hwang 2011). Additionally, ocean to wave model coupling, which includes passing near surface NCOM ocean currents and water levels to SWAN, is explored through observational comparisons of both coupled and uncoupled ocean/wave model interaction simulations for Hurricane Ivan.

3.1.2 Test Area and Observations

The lifecycle of Hurricane Ivan began as a tropical wave on 31 August 2004. It developed into a tropical depression on 2 September near 9.7^{o}N. The system strengthened into Tropical Storm Ivan and continued westward south of 10^{o}N becoming a hurricane on 5 September. After entering the southern Gulf of Mexico (GOM), Ivan turned north-northwestward, becoming a large and intense TC in the central and eastern GOM from 0000 UTC 14 September until landfall at approximately 0700 UTC 16 September 2004, just west of Gulf Shores, AL, at a maximum intensity of 110 kts (130 mph).

Observational data from the GOM was supplied by fourteen ADCPs, five buoys, one SRA flight track, and eight satellite altimeter passes. The combination of these datasets provides a comprehensive spatial and temporal sampling of Ivan as it traversed through the GOM. The fourteen ADCPs were deployed in May 2004 along the outer continental shelf and slope in the northeastern Gulf of Mexico (Figure 3.1-1). Six moorings were deployed along the outer shelf in two rows of three, each with a horizontal spacing of 15 km. The first row of moorings, denoted as M1-M3, had vertical depths of 60 m, while the second row, M4-M6, had vertical depths of 90 m. They were deployed in Trawl Resistant Bottom Mounts (TRBM), which utilized dome-shaped mounting pods known as “Barny” mounts for their barnacle-like shape (Perkins et al. 2000). The moorings were equipped with Sea-Bird Electronics wave/tide gauges and RD Instruments Workhorse ADCPs, which operated at 300 kHz. The ADCP heads were situated about 0.5 m off the sea floor and recorded current profiles with 2 m vertical resolution with an accuracy of 0.5 ± 0.5 cm s^{-1} at 15 minute intervals. ADCPs M1-M3 were deployed down the outer shelf at 60 m depth and M4-M6 were deployed at 90 m. Eight moorings were deployed along the continental slope in two rows of four. The moorings in each row were 15 km apart. The first row, M7-M10, had vertical depths of 500 m, and the second row, M11-M14, had vertical depths of 1000 m. These deep-water moorings consisted of RD Instruments Long Ranger ADCPs, which operated at 75 kHz and were housed in 45-inch diameter Flotation Technology buoys. Vertical current profiles of approximately 500 m were measured every hour with 10 m resolution and an accuracy of 1 ± 0.5 cm s^{-1}. Additionally, the data were filtered for removal of measurement error and high-frequency motions (Teague et al. 2007).

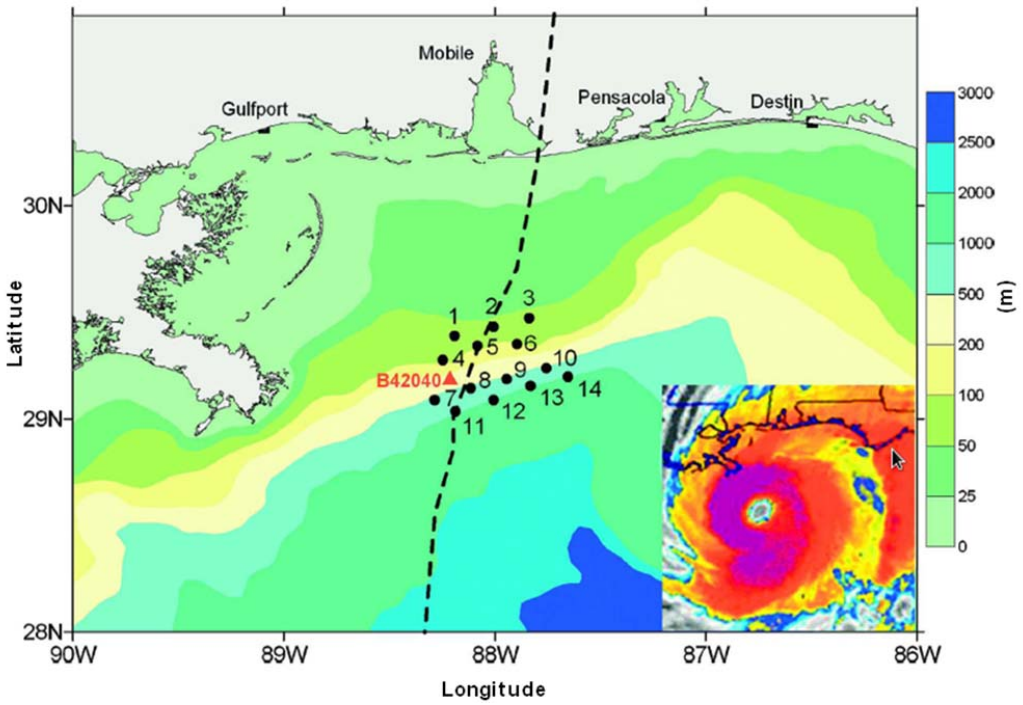

Figure 3.1-1: ADCP array in the northern Gulf of Mexico in September, 2004 (adapted from Teague et al. 2007). Bathymetry contours, the location of NDBC buoy 42040, and the best track of Hurricane Ivan are shown. Inset: Infrared satellite picture of Hurricane Ivan as the hurricane approached the northern GOM coast on 15 September, 2004.

Several National Data Buoy Center (NDBC) buoys were in close proximity to Hurricane Ivan as it crossed the central and northern GOM (Figure 3.1-2). Buoy measurements included atmospheric pressure, wind speed and direction, air and water temperature, wave energy spectra, ocean current velocity, SWH, wave period, and wave direction. Based on NDBC field studies, SWH accuracies are within 0.2 m or 5%, wave periods are within 1 s, and wave directions are within 10 degrees.

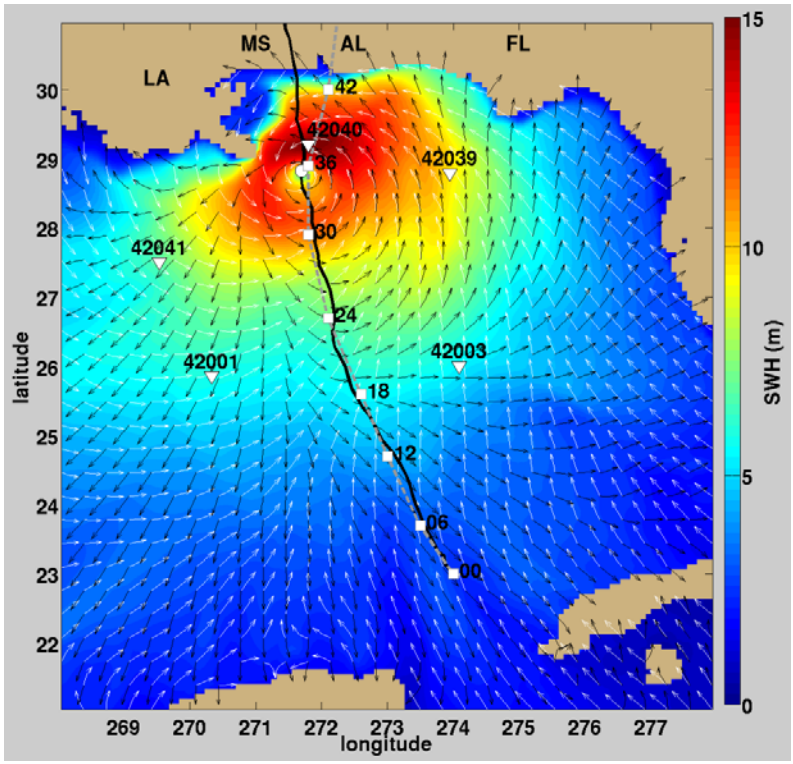

Figure 3.1-2: The locations of NDBC buoys 42001, 42003, 42039, 42040, and 42041 are denoted by white triangles. Hurricane Ivan's observed best track is illustrated by the dashed white line and the model track by the solid black line. The background display shows the COAMPS-TC SWH at forecast hour 41 from the 1200 UTC 14 September 2004 72-hour forecast. Wind (white) and wave direction (black) vectors are plotted.

The European Space Agency's GlobWave project consolidates ocean wind and wave data from multiple satellite instruments. This dataset is quality controlled and available through a single website for easy access. Detailed information can be found in Snaith et al. (2010). The GlobWave altimeter data for the SWAN model validation during 14-16 September 2004 were acquired from three satellites, the European Remote Sensing satellite (ERS-2), ENVISAT, and GFO. These satellite altimeters provided several snapshots of the spatial variations of both Ivan's wind and wave fields along its track over the GOM. Gridded model wind and wave data within 30 minutes of the satellite passing times were spatially interpolated from grid points to the positions along the satellite tracks. Additionally, NASA reconnaissance aircraft (SR-71) used SRA to collect high resolution wave spectra and SSH data for several periods during Hurricane Ivan's lifecycle. The wave spectra from the SRA flight in the southern GOM were used to quantify the performance of SWAN in extreme wind and wave conditions within all four quadrants of the cyclone.

3.1.3 Model Setup

The COAMPS-TC model setup for Hurricane Ivan (Figure 3.1-3) consisted of a triple-nested atmospheric domain with 18, 6, and 2 km horizontal resolution and a total of 60 terrain-

following vertical levels. The outer, course nest extends from the equator to 38°N and from 65°W to 108°W, with horizontal dimensions of 250 × 250. The two inner nests translate in tandem with the cyclone's vortex center. Atmospheric boundary conditions are provided by the Navy Global Atmospheric Prediction System (NOGAPS) model. The TC vortex initialization in NAVDAS is enabled through a TC warning message, including location, wind radii, and intensity information provided by the National Hurricane Center in Miami, FL. Each data assimilation cycle is initiated using the prior 12-hour forecast as background, incorporating quality-controlled observations from radiosondes, aircraft, satellite, ship, and surface stations.

The NCOM configuration (Figure 3.1-3) consisted of one nest (4 km resolution) that encompassed the GOM and the Caribbean Sea. The ocean nest extended from 10°N to 31°N and 67°W to 98°W with horizontal dimensions of 800 × 600. A total of 50 vertical levels, 36 of which were sigma coordinate levels in the upper 190 m of the water column, were used with the Navy's Digital Bathymetric Data Base (DBDB2) data set. NCOM was initialized using global NCOM hindcast data. NCODA 3DVAR ingested observational and global model ocean data including quality-controlled satellite, ship, and profiler data for each update cycle. The ocean model was run with tides and rivers included.

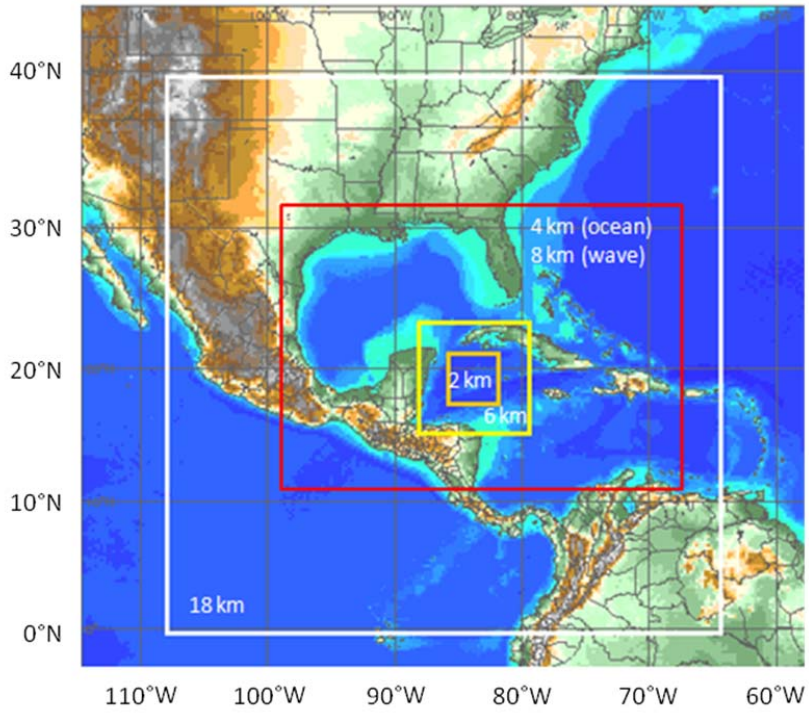

Figure 3.1-3: Atmospheric nests (18 (white), 6 (yellow) and 2 (orange) km) and ocean/wave (4/8 km, red) nest setup for Hurricane Ivan.

The SWAN model configuration consisted of one nest (8 km resolution) that encompassed the exact latitude and longitude dimensions of the ocean nest, with horizontal dimensions of 400 × 300. Thirty-six discrete direction and 25 frequency bands were selected using DBDB2 bathymetry. Boundary conditions for SWAN would normally consist of energy spectra from a

larger global model such as WaveWatch III; however, the TC provided the dominant wave effects in the model, rendering other wave energy inputs insignificant.

The ocean and wave models provided feedback to the atmosphere through the high-resolution NCOM SSTs and SWAN wave age (Moon et al. 2004b), computed from SWAN wave spectra to formulate the atmospheric model Charnock relation to improve atmospheric heat and moisture fluxes in TC conditions.

3.1.3.1 COAMPS-TC Forecast Setup

Spin-up of NCOM and SWAN with 12 hour atmosphere and ocean data assimilation cycles commenced at 0000 UTC on September 1, 2004. Spin-up of Hurricane Ivan's vortex began on 0000 UTC September 10, when the well-developed cyclone was located over the Caribbean Sea, to provide a stable initial state as Ivan entered the Gulf of Mexico on 14 September. Wind forcing was provided by the NOGAPS model prior to 0000 UTC September 10. For each model configuration, two 72-hour forecasts of Hurricane Ivan were generated at 0000 UTC and 1200 UTC 14 September to provide comparison to in situ atmospheric, ocean, and wave data observations for each of the above configurations. Depending upon the data set comparisons, both the 0000 UTC and 1200 UTC forecasts were utilized and each of these forecasts is discussed based on its applicability to a specific observational data set.

3.1.4 Results

3.1.4.1 Ocean to wave coupling in COAMPS-TC

Low errors in forecast track and intensity of Hurricane Ivan in relation to the observational data allowed for acceptable statistical comparisons to be generated for evaluating the ocean/wave coupling in COAMPS-TC for Hurricane Ivan. Both the ocean/wave uncoupled and coupled model COAMPS-TC simulations produced intensity errors that were generally 5 m s^{-1} or less (Figure 3.1-5). For low cross track errors of less than 20 nm (37 km), the track was nearly identical for all simulations of Hurricane Ivan as the cyclone traversed the GOM for both the 0000 UTC and 1200 UTC 14 September 2004 forecasts, which allowed for direct comparisons between the coupled and uncoupled model simulations (Figure 3.1-2).

3.1.4.2 Comparisons to NDBC Buoys

To directly compare observational data to the sensitivity of ocean to wave coupling in the Hurricane Ivan forecasts, data from several NBDC buoys were analyzed during Hurricane Ivan's passage over the eastern and central GOM. NBDC buoy 42040, just offshore of the northern GOM coast and within the ADCP array (Figure 3.1-1), was directly impacted by the inner core of Hurricane Ivan. Surface currents at buoy 42040 are normally quite weak at this location, generally less than 10 cm s^{-1}; however, as the cyclone passed over the buoy, near surface currents exceeded 2 m s^{-1} as measured by ADCP M1 (see Figure 3.1-10). Figure 3.1-6 (left) is a plot of SWH for both BHunc and BHcpl simulations compared to observations at buoy 42040. Although along-track lag time was present (about 6 hours), the BHunc simulation produced SWH of 17-18 m, while the BHcpl simulation produced maximum SWH between 15-

16 m, a difference of approximately 2 m. The addition of the strong, hurricane-induced surface currents into SWAN lowered the SWH to a more reasonable value when compared to the uncoupled model at buoy 42040.

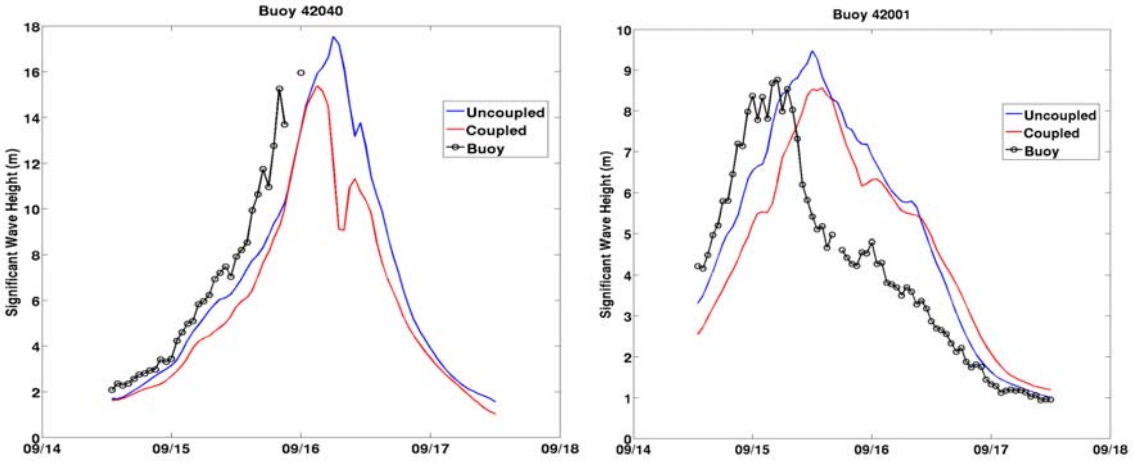

Figure 3.1-6: Uncoupled (blue, BHunc) and coupled (red, BHcpl) comparisons to NDBC buoy observations (black) of SWH for the 1200 UTC 14 September 2004 72-hour forecast. Left: Buoy 42040 Right: Buoy 42001.

Another NDBC buoy (42001) located outside of Hurricane Ivan's inner core also showed improvements in ocean to wave model coupling. Surface ocean currents in September 2004 revealed a very large warm core eddy that had shed from the Loop Current and was centered just east of buoy 42001. Pre-Hurricane Ivan surface currents at buoy 42001 were on the order of at least 0.5 m s^{-1}. Inclusion of the surface currents in the BHcpl simulation reduced the SWH substantially at buoy 42001 when compared to the uncoupled model (Figure 3.1-6, right). For both buoys 42040 and 42001, the presence of strong surface currents, whether or not hurricane-induced, acted to improve the SWH in SWAN at these particular locations. Results from other buoys in the BHcpl simulation, far from the region of strongest winds and in areas of weak surface currents, showed modest differences from the BHunc simulation.

3.1.4.3 Scanning radar altimeter (SRA) and satellite altimeter comparisons

Although useful in point comparisons, the array of NDBC buoys in the GOM could not adequately capture the evolving wave field in each quadrant of a tropical cyclone. As a TC translates in a certain direction, it is unlikely that fixed buoys would provide enough information about the wave field in each quadrant relative to the TC's center. In addition, not all buoys provide directional wave spectra, which further reduce the quantification of the wave field. The SRA, on the other hand, is an airborne instrument with high spatial and temporal resolution along the flight tracks, and it has been successfully used to observe the wave field in the vicinity of a TC (Wright et al. 2001).

For the purpose of this study, the SRA flight track that best fit the simulation window began at 2008 UTC 14 September and completed at 0347 UTC 15 September, a flight duration of 7 hours and 39 minutes (Figure 3.1-7). A similar study of Hurricane Ivan (Fan et al. 2009), employing WW3 instead of SWAN, used offline and pre-computed atmospheric and oceanic fields to force the wave field in order to make comparisons to the SRA data. However, the fully-coupled air/sea/wave COAMPS-TC system used here exchanged relevant fields as frequently as desired, which may or may not be as beneficial as pre-computed forcing.

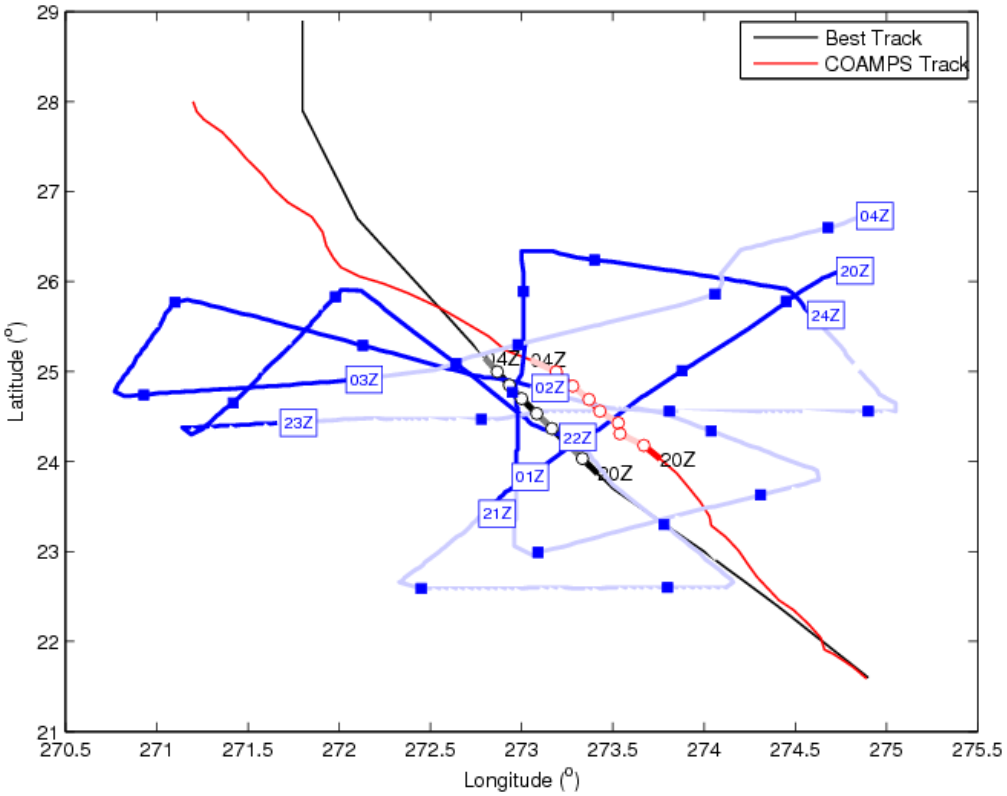

Figure 3.1-7: Flight track of the airborne SRA (blue line) starting at 2000 UTC 14 September, 2004 and ending at 0400 UTC 15 September, 2004 at 04Z. Full hours are printed in boxes and 15 minute intervals are denoted as blue squares. Flight segments starting with even (odd) hours are colored dark (light) blue. The observed (black) and simulated (red) TC tracks are shown. Circles on both tracks represent hourly locations of the storm centers.

The output fields from SWAN were interpolated to the locations of the airborne sensor along the flight track at 15 minute intervals (e.g. 2000 UTC, 2015 UTC, 2030 UTC…) for the 0000 UTC 14 September forecast. The first (last) SRA measurements at 2008 UTC (0347 UTC) were used for comparison with SWAN data at 2000 UTC (0400 UTC). The SRA data were not regularly spaced in time, so data chosen were those measurements closest to the regular 15 minute intervals. The maximum time discrepancy was less than four minutes, except for the first and last set of measurements. In order to properly gauge the wave response in the model, the track error calculations (which were small) were adjusted accordingly to provide the best

possible comparison between the model simulation and SRA observations. The two parameters used for the validation of SWAN, SWH and mean wave propagation direction (MWPD), were calculated from the directional spectra:

$$SWH = 4\sqrt{\iint E(\omega,\vartheta)d\omega d\vartheta} \tag{2}$$

$$MWPD = tan^{-1}\frac{\iint \sin\vartheta\, E(\omega,\vartheta)d\omega d\vartheta}{\iint \cos\vartheta\, E(\omega,\vartheta)d\omega d\vartheta} \tag{3}$$

where $E(\omega,\vartheta)$ is the variance density spectrum as a function of frequency (ω) and azimuthal angle (ϑ). For the SRA data, both derived parameters were readily provided. Additionally, if the wave spectrum was bimodal, both primary and secondary propagation directions were given.

For the 0000 UTC 14 September BHcpl forecast, the preliminary comparison between SRA and SWAN indicated that SWAN overpredicted the SWH by 1-2 m at a few locations (Figure 3.1-8). However, this result was a significant improvement over the classic SWAN wave physics parameterizations. The mean error (ME) in the BHcpl simulation was 1.62 m and the root mean square error (RMSE) was 2.55 m; however, when the comparisons were adjusted for track error, the SWH ME was reduced to 1.25 m and the RMSE was reduced to 1.78 m. The largest differences in SWH are mostly attributed to the peaks in the simulated SWH. The associated times (2045, 2200, 2315, 0045, 0215, and 0315 UTC 14-15 September 2004) and corresponding locations of the maxima, when superimposed on the flight track, revealed a consistent pattern with the SRA to the northeast, or even over the eye of the TC, while the simulated storm track was at least 10 nm (18.5 km) to the east of the observed track. Further SRA analysis involving the wind field, especially the radius of maximum wind velocity, was beyond the scope of this paper. On the other hand, the modeled MWPD was very close to the observed value (Figure 3.1-8). The bias was very small, approximately -5^{o}, and the RMSE was 34.2^{o} when adjusted for track error. The propagation direction was captured very well; however, the SWAN waves were propagating to the left of the actual wave field (MWPD ME of -24.71^{o} when adjusted for track error); therefore, they were shifted by about a quarter of a quadrant (22.5^{o}).

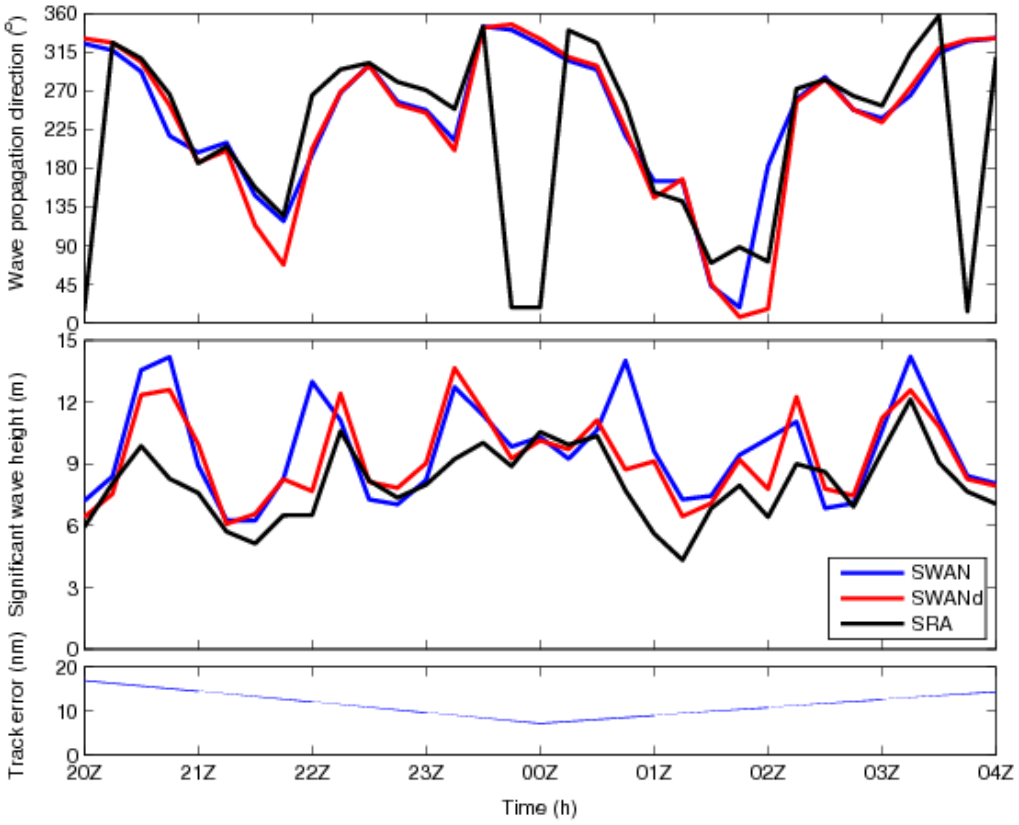

Figure 3.1-8: The airborne SRA measurements (black) of SWH as a function of wave propagation direction (top), significant wave height (middle), and track error (bottom) beginning on 2000 UTC 14 September, 2004 and ending on 0400 UTC 15 September, 2004. SWAN (blue) and track-adjusted SWAN (red, SWAN displaced (SWANd)) results are shown.

In addition to the flight SRA data, several satellite altimeter measurements of winds and SWH were also compared to model results. Three satellites, ENVISAT, ERS-2, and GFO provided numerous passes that yielded useful observational information. Figure 3.1-9 shows the ground passes made by each of the satellites for 14-16 September 2004. However, the position of each pass was such that measurements within the inner core of Ivan were not sampled. Statistical analyses of all measurements taken during the period indicated that the BHcpl simulation for both the 0000 UTC and 1200 UTC forecasts showed improvement in SWH, especially in regions where larger SWH were measured.

Figure 3.1-9 represents a model data comparison during an ERS2 pass that was nearest the inner core of Ivan. The spatial plots of SWH for both the uncoupled and coupled simulation in Figure 3.1-9 clearly show the overall decrease in SWH values when NCOM currents are passed to SWAN in the coupled simulation. The specific comparison of SWAN to the ERS2 pass at the bottom of Figure 3.1-9 indicates that the maximum SWH is approximately 1-2 meters less in the coupled model than in the uncoupled model. The coupled model result was in better agreement with the observations, especially in the region of higher SWH.

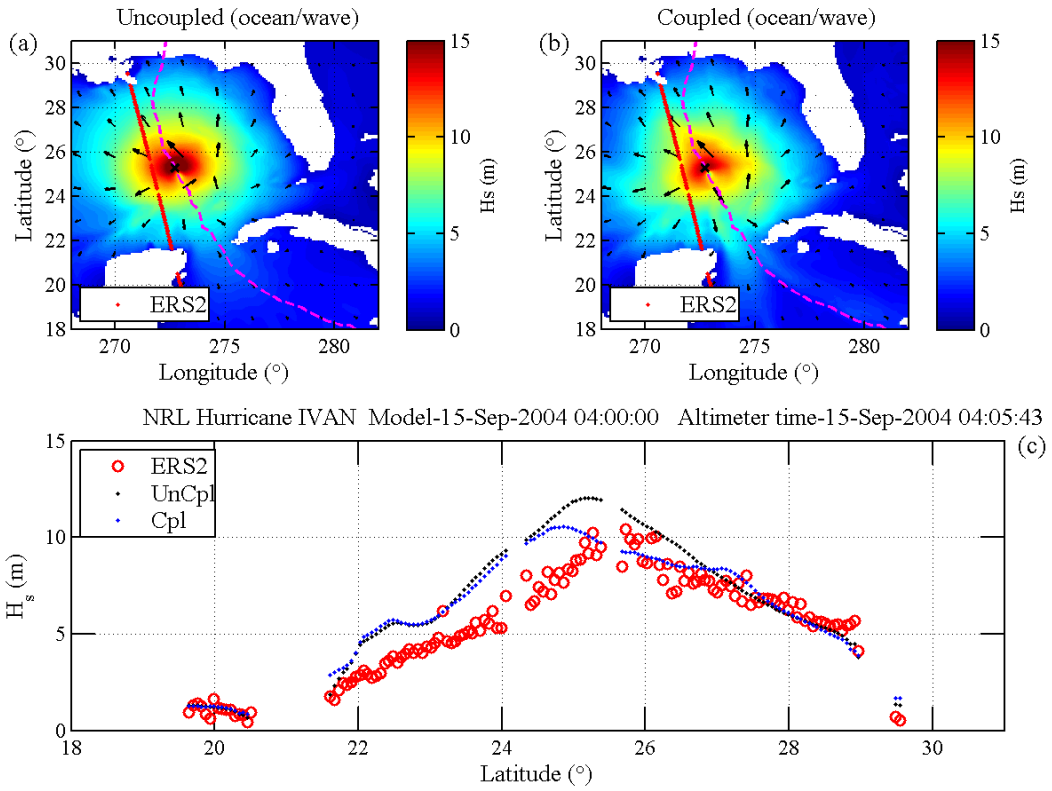

Figure 3.1-9: SWH comparison to the ERS2 satellite altimeter pass at 0400 UTC 15 September. Spatial SWH fields are shown in the a) Uncoupled SWH (BHunc) and b) coupled SWH (BHcpl) simulations. The red dots show the ERS2 altimeter pass measurements in relation to Ivan's path (hatched magenta line) and center of circulation (marked as X) on 0400 UTC 15 September. c) The SWH measured from ERS2 (red circles) is directly compared to the coupled (BHcpl, blue dots) and uncoupled (BHunc, black dots) simulation for 0400 UTC 15 September.

Figure 3.1-10 shows statistics for all 806 measurements taken by satellite compared to the 1200 UTC 14 September 72-hour BHcpl and BHunc forecasts. The BHcpl RMSE was 0.974 m compared to 1.25 m for BHunc, which indicates a consistent reduction in SWH in the ocean/wave coupled simulation. These results are consistent with the lowering of the SWH in the sensitivity tests when ocean to wave model coupling is included.

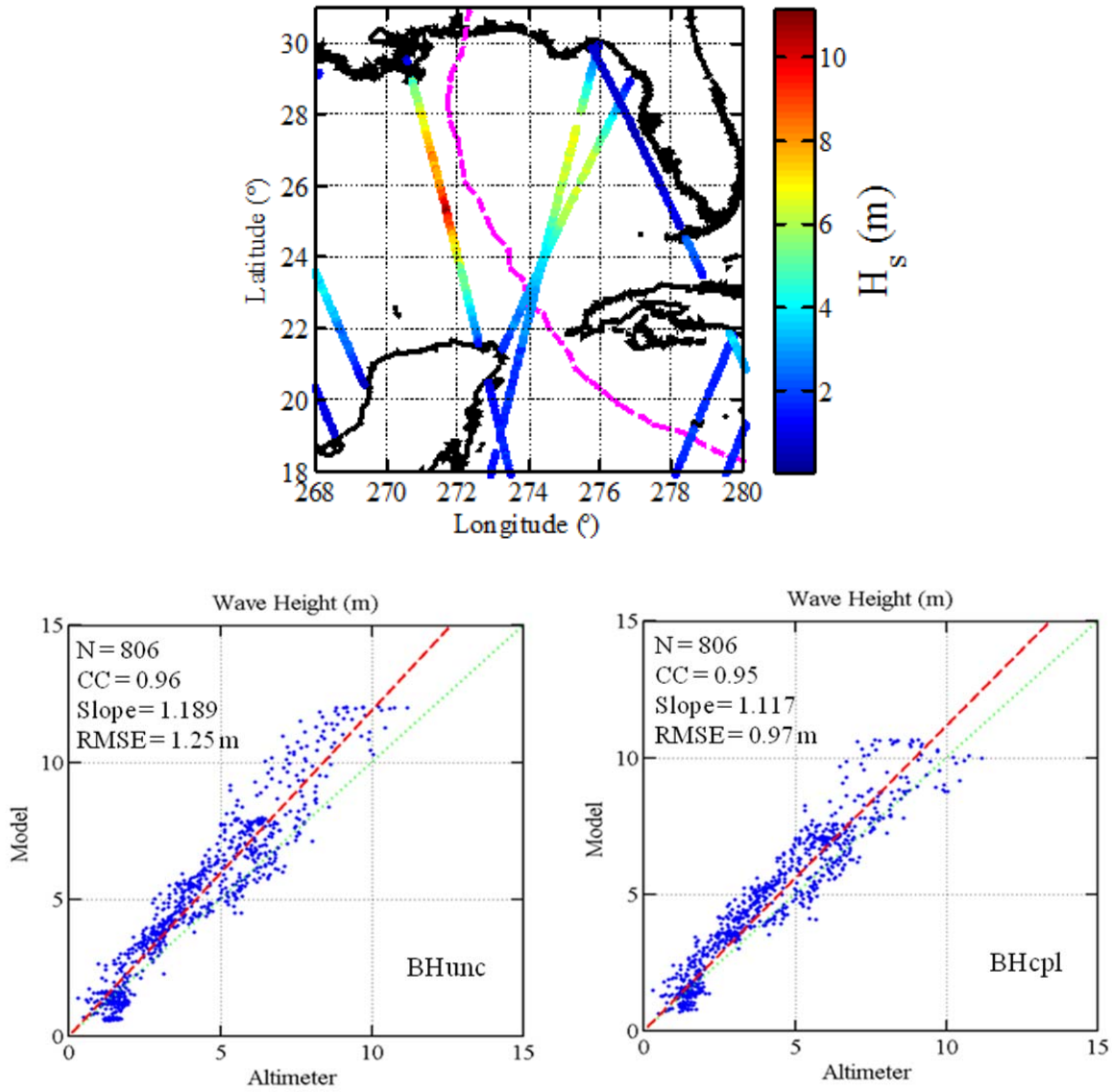

Figure 3.1-10: Satellite altimeter paths with SWH (H_s) for 1200 UTC 14 September 2004 forecast (top). Statistical analysis for all N=806 observations for BHunc (bottom left) and BHcpl (bottom right).

3.1.4.4 Wave - ocean coupling ocean current response in COAMPS-TC

NCOM was allowed to spin-up with NCODA ocean data assimilation for several weeks prior to the arrival of Hurricane Ivan into the GOM to allow pertinent ocean circulation and surface features to develop, thus providing a good initial state for the cyclone's passage over the GOM. As stated previously, the 1200 UTC 14 September 2004 72-hour forecast track of Hurricane Ivan brought the cyclone directly over the 14 ADCP current profilers deployed along the outer continental shelf and upper slope of the GOM just south of the Mississippi and Alabama coasts. The ADCP data indicated that the shelf currents followed Ekman dynamics

with overlapping surface and bottom layers during Ivan's approach and transitioned to a dominant surface boundary layer as the wind stress peaked with Ivan's passage (Teague et al. 2007). In addition, Hurricane Ivan generated very strong surface and subsurface currents on the shelf and slope. For example, the ADCP M1 measured currents in excess of 200 cm s^{-1} (2 m s^{-1}) during the forced stage response, while currents on the slope at depths > 50 m commonly exceeded 50 cm s^{-1}.

To compare the observed ocean current response near and below the surface in the COAMPS-TC simulations, we followed Kuzmic et al. (2007) for calculations of the magnitude of the complex correlation coefficient(s) (CCC, Eq. 4) and the angular displacement, or mean directional error (MDE, Eq. 5), between the measured ADCP and NCOM model currents in the BHunc and BHcpl simulations (Kundu (1976))

$$CCC = \frac{\langle u_o u_m + v_o v_m \rangle + i\langle u_o v_m - u_m v_o \rangle}{\sqrt{\langle u_o^2 + v_o^2 \rangle} \cdot \sqrt{\langle u_m^2 + v_m^2 \rangle}} \tag{4}$$

$$MDE = \tan^{-1}\left[\frac{\langle u_o v_m - u_m v_o \rangle}{\langle u_o u_m + v_o v_m \rangle}\right] \quad , \tag{5}$$

where u and v are the east-west and north-south, observed (o) or modeled (m), demeaned velocity components. The brackets in each equation represent the time average of each component. The CCC and MDE were computed for the ADCP moorings as a function of depth based on the closest corresponding NCOM level to each ADCP bin. Inherent in the computation, the CCC accounts for both the current speed and direction in its calculation of the correlation coefficient.

Table 3.1-1 summarizes the statistical results at each of the ADCP moorings in Figure 3.1-1. Every calculation was made at the closest possible grid point to the moorings, paying close attention to the model bathymetry. For each ADCP, there were 13 or 14 bins directly comparable to NCOM's vertical depth levels. As stated previously, the M1-M6 ADCPs were shallow-depth moorings that were located either on the shelf or slope while the M7-M14 ADCPs were located off the shelf in much deeper water. To accurately gauge the ocean response to Hurricane Ivan, the lag time within the forecast was factored into each calculation. It is important to note that these calculations are very sensitive to along and cross track errors, whether in distance and/or time, and the lag time adjustments were necessary to reduce errors as much as possible. Since the model track was quite good, the lag time was simply calculated by comparing the best-track location and times with the model track times and shifting the model track forward in time to better match the best track from observations.

Table 3.1-1: ADCP array ocean current statistical comparisons for the BHcpl simulation. The magnitude of the complex correlation coefficient (CCC) and mean directional error (MDE) are computed. The CCC and MDE are also averaged over all the bins.

SHALLOW ADCPs	# BINS	TOP BIN DEPTH (m)	BOT. BIN DEPTH (m)	CCC (BHcpl)	MDE (deg, BHcpl)
M1	13	6	52	0.81	7.02
M2	14	4	54	0.80	11.68
M3	13	6	54	0.78	10.98
M4	13	10	82	0.80	11.86
M5	13	11	83	0.81	14.34
M6	14	9	81	0.82	15.12
	AVERAGE OF ALL SHALLOW WATER ADCPs:			0.80	11.83
DEEP ADCPs					
M7	13	52	492	0.70	4.78
M8	13	52	492	0.84	10.98
M9	13	50	492	0.77	8.02
M10	13	50	500	0.85	15.67
M11	13	53	493	0.82	14.87
M12	13	53	513	0.72	16.54
M13	13	50	500	0.72	12.54
M14	13	52	502	0.78	11.40
	AVERAGE OF ALL DEEP WATER ADCPs:			0.78	11.85

For each shallow-water ADCP, current measurements were taken in intervals of 15 minutes. Within every 15 minute interval, each ADCP recorded several measurements (or pings). These measurements were then averaged every 15 minutes and velocities recorded. NCOM currents were then compared to the ADCP currents throughout the 72-hour 1200 UTC September 14 forecast, which included the best track and intensity forecast of Hurricane Ivan over the ADCP array in the BHcpl simulation (the BHunc simulation produced similar results).

The lag adjusted CCC and MDE for the shallow ADCPs were very good when compared to the model results (CCC and MDE values were averaged over the bins in Table 3.1-1). Statistics for the period encompassing the forced ocean response to Hurricane Ivan indicated mean CCC values of greater than 0.8 and mean MDE values of less than 15^{o} in the BHcpl simulation throughout the water column for almost all of the shallow ADCPs. In fact, the MDE calculations for the top 3-4 bins nearest the surface were generally less than 10 degrees for all the shallow ADCPs, indicating a very good ocean response to the intense wind forcing (and good Ivan track) near the surface. Figure 3.1-11 shows a vertical velocity plot of the observations and NCOM results at ADCP M1. For ADCP M1, the top most bin was located at a depth of 6 m. The upper-ocean response in the model was quite similar to the response recorded at M1; however, stronger velocities extended a little further in depth at the ADCP than in the model.

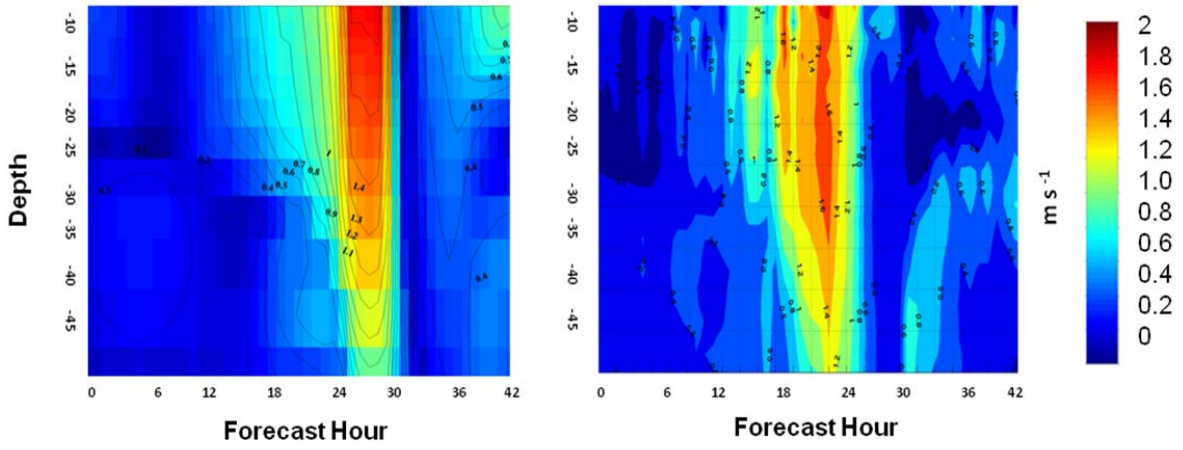

Figure 3.1-11: Current velocity vertical profile for NCOM (left) and observations (right) at the location of ADCP M1.

For the deep M7-M14 ADCPs, the mean CCC and MDE were comparable to shallow ADCPs, although the forcing effects of Ivan on currents were generally negligible below 60 m. In fact, the largest errors in MDE for the deep ADCPs occurred due to the model overestimating the depth at which direct effects of the surface forcing were being measured. At some of the deep ADCPs, the forcing in the model registered at least 20 m below what was measured by the ADCP current observations. This equated to MDE values of less than 10^{o} in the topmost bins of the deep ADCPs, while some of the ADCP bins just below the top few had MDE values greater than 20^{o}. This, in turn, increased the overall mean MDE for some of the deep-water ADCPs.

Errors in the MDE can be attributed to several factors for both the shallow and deep-water ADCPs. The model track was excellent as Ivan approached the southwestern edge of the ADCP array nearest to M11. It is important to emphasize that the differences between Hurricane Ivan's track and intensity versus those in the BHcpl simulation were very minimal, which allowed for a direct comparison of CCC and MDE. However, an almost due north model track in both simulations continued past ADCP M11, which was west of the observed track of Hurricane Ivan. This deviation in track as Ivan exited the ADCP array is likely due to some of the MDE statistical errors. Errors in the initial condition and representation of the ocean current velocities at the beginning of a forecast are always critical; however, the use of 3DVAR ocean assimilation leading up to the 72-hour forecast reduced this error for each of the ADCPs. Overall, the ocean current velocity and direction response for Hurricane Ivan in COAMPS-TC was satisfactory.

3.2 Test Case 2: Okinawa Trough

3.2.1 Purpose

The purpose of this test case is to validate the COAMPS coupled ocean-wave prediction system and to quantify the interactions among winds, waves, and currents. The Okinawa Trough region was selected due to its highly dynamic nature: complex geometry, sharp bathymetry gradient, strong Kuroshio currents, large barotropic and internal tides, and frequent typhoon passage. All of these features provided an excellent opportunity to evaluate air-ocean-wave interactions. In addition, all the numerical experiments in this test case were carried out over a four month period (7/1-10/31/2007), a long-term simulation that allowed us to assess the robustness and stability of the coupled system.

3.2.2 Test Area and Observations

The Okinawa Trough is a seabed feature of the East China Sea. It is an active, initial back-arc rifting basin which formed behind the Ryukyu arc-trench system in the western Pacific Ocean. A large section of the Trough is more than 3,300 feet (1,000 meters) deep and its maximum depth is 8,912 feet (2,716 meters). The study region encompasses the Okinawa Trough, Ryukyu Islands of Japan, Taiwan and Luzon Strait from 17-34° N and 118-134°E (Figure 3.2-2).

In this test case, satellite-derived altimetry from the European Space Agency's GlobWave project was the primary source of wind and wave observational data. The satellites from which wind speed and wave height data were derived included ENVISAT, Jason-1 and GFO satellites. The ENVISAT, Jason-1 and GFO have repeat cycles of 35, 10, and 17 days, respectively. As a result, from August through October of 2007, data along three satellite tracks were used to validate COAMPS wind and wave predictions. Satellite ground tracks in the model domain are shown in Figure 3.2-1.

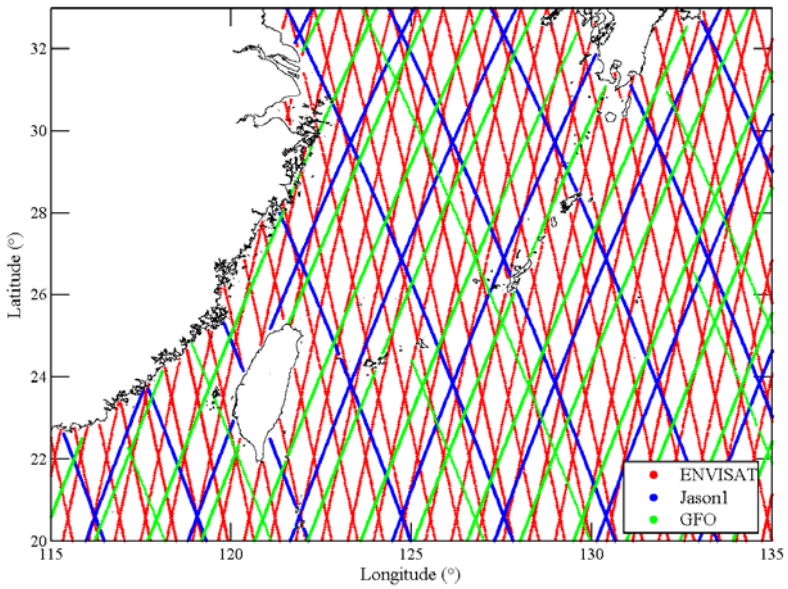

Figure 3.2-1: Satellite altimeter tracks in Okinawa Trough region, July 1- Nov 1, 2007.

Observational data come from several sources. An extensive naval exercise was conducted to collect more than 7000 subsurface T and S profiles using gliders and expendable bathythermograph. 1400 additional T and S subsurface profiles came from the World Meteorological Organization Global Telecommunications System. Surface currents were evaluated using a surface drifter data set from World Ocean Circulation Experiment (WOCE). The validation procedure and results are described in Section 3.2.4. Sonic Layer Depth (SLD) and related acoustic properties were evaluated using a combination of AXBT, gliders and profile data.

3.2.3 Model Setup

In the COAMPS atmospheric component, the test case domain spanned from 17 to 34°N and from 118 to 134°E with a horizontal resolution of 27 km (Figure 3.2-2). The open boundary and initial conditions were derived from the 1° NOGAPS. COAMPS provided atmospheric forcing parameters such as wind stress, dew point depression, insolation, longwave, latent, and sensible surface heat fluxes, surface evaporation and precipitation rates, and atmospheric pressure.

The NCOM ocean component test case domain spanned from 17 to 34°N and from 118 to 134°E with a horizontal resolution of 3 km. The grid had 535 x 628 horizontal grid points with 50 vertical layers. Global 1/8° NCOM provided the initial and boundary conditions. Each cycle had 12 hours of hindcast and 12 hours of forecast. Tidal and river forcing were turned on. Tidal forcing fields were interpolated from the global OTIS (Oregon Tidal Inverse Software) database (Egbert and Erofeeva, 2003) and river forcing was obtained from the NCOM river database (Barron *et al*., 2006). The time step was set at 30 seconds.

As in NCOM, the SWAN wave component model domain stretched from 17 to 34°N and from 118 to 134°E with a horizontal resolution of 9 km with 36 direction bins and 24 frequencies. The grid has 187 x 214 horizontal grid points. The time step was 60 seconds. Open boundary conditions were provided by global WW3.

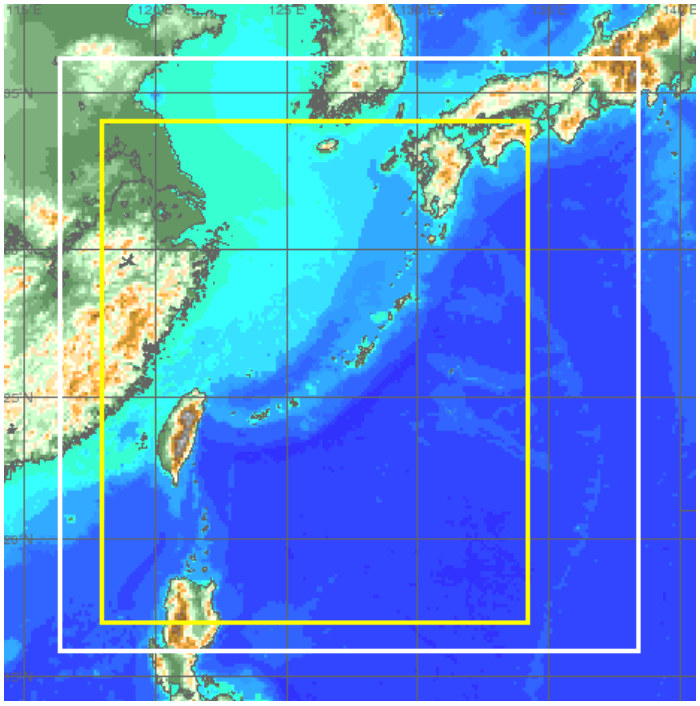

Figure 3.2-2: COAMPS model grid domains for the Okinawa Trough. The white box frames the COAMPS 27 km resolution atmosphere domain. The NCOM 3 km and SWAN 9 km domain is represented by the yellow box.

The numerical experiments performed with various coupling strategies, and the differences among the experiments, are defined as follows:

- Uncoupled (sometimes referred in this test case as 1-way coupling) represents an atmosphere-to-wave feedback scheme only. The atmospheric portion of COAMPS was run as a single nest of 27 km.
- 4-way coupling represents atmosphere-to-ocean, ocean-to-atmosphere, ocean-to-wave and atmosphere-to-wave feedback scenarios.
- 5-way coupling is defined as 4-way coupling plus the wave to ocean feedback, which adds Stokes drift and radiation stress terms back to the NCOM current computation.

3.2.4 Results

These numerical experiments were performed in order to evaluate the ocean-wave coupling effect on wind, waves, SST and currents. This section describes the validation procedures and the impact of coupling on each environmental variable. The results are shown in the following figures and summarized in the tables.

3.2.4.1 Impact of ocean-wave coupling on winds

During an initial test, wind speed data for different coupling experiments were compared with satellite altimeter data. The scatter plots for uncoupled vs. 4-way coupled cases are shown in Figure 3.2-3. Their statistics are summarized in Table 3.2-1. COAMPS-predicted wind speed was highly correlated with satellite altimeter data (R = 0.84) and approximately 10% lower than the altimeter data. Ocean-wave coupling improved the ratio slightly.

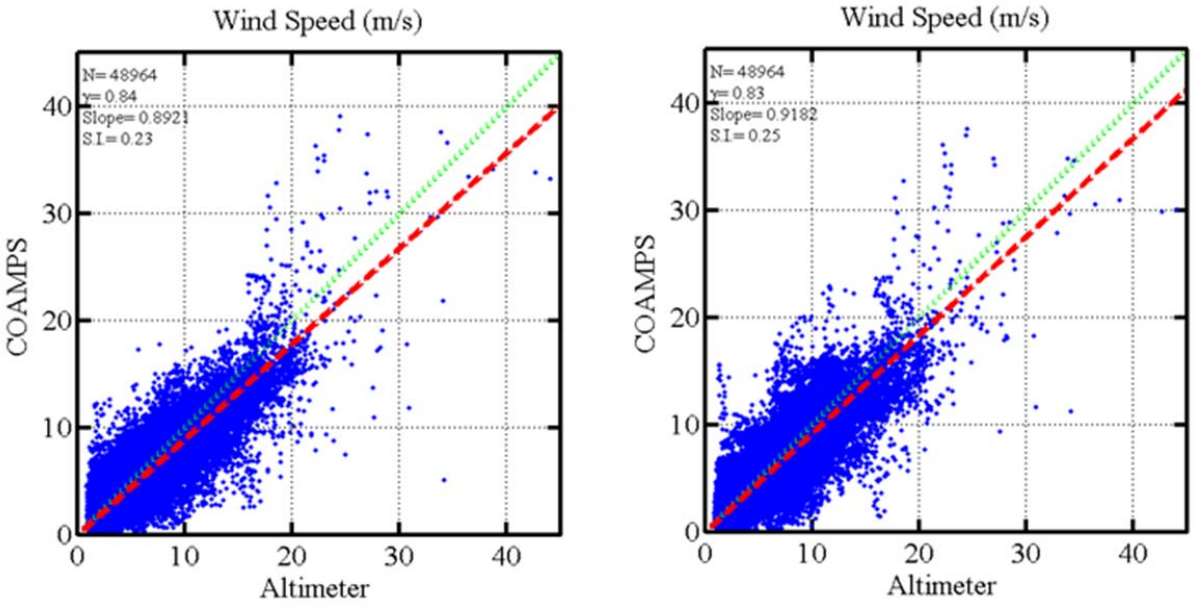

Figure 3.2-3: Comparison of uncoupled (left) and 4-way coupled (right) COAMPS wind speeds vs. altimeter data.

Table 3.2-1: Statistical summary of altimeter wind validation for wind speed.

COAMPS Wind Speed vs. Altimeter (N=48964)			
	Ratio	**Correlation**	**SI**
Uncoupled	0.89	0.84	0.23
4wayCpl	0.92	0.84	0.24
5wayCpl	0.92	0.83	0.25

3.2.4.2 Impact of ocean-wave coupling on waves

Scatter plots comparing the significant wave heights for different coupling experiments with satellite altimeter data are shown in Figure 3.2-4. Their statistics are summarized in Table 3.2-2. The SWAN-predicted wave heights were highly correlated with satellite altimeter data (R=0.84-0.88) and were also under estimated, as was the COAMPS-predicted wind speed.

Scatter Index (SI) is defined as the ratio of RMSE to mean, where a small SI value indicates better skill and less spread.

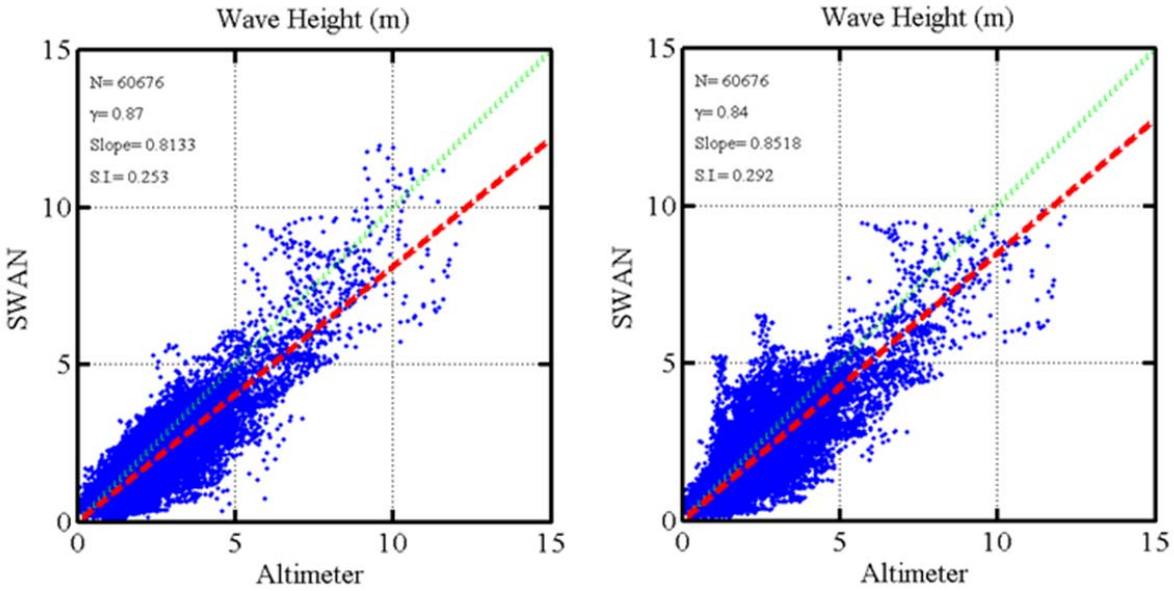

Figure 3.2-4: SWAN wave height vs. altimeter data for uncoupled (left) and 5-way coupled (right) with NCOM.

Table 3.2-2: Statistics summary of altimeter wind validation for wave height.

SWAN Wave Height vs. Altimeter (N=60679)			
	Ratio	**Correlation**	**SI**
Uncoupled	0.81	0.87	0.25
4wayCpl	0.88	0.88	0.26
5wayCpl	0.85	0.84	0.29

Figure 3.2-5 shows the wave height differences between the uncoupled and 5-way coupling experiments. The surface signature of Kuroshio can be seen clearly in this region. Additional numerical experiments show the the difference between the 1-way and 4-way coupling is less than that between the 4-way and 5-way, pointing to the significance of wave-ocean feedback. Another region showing a large difference due to ocean-wave coupling is the south east corner of the model domain. Similar spatial patterns are also observed in the wind field difference plot. This could be due to passage of the four major typhoons along this track, whereby strong wind caused strong current and interacted with waves during the three months validation period.

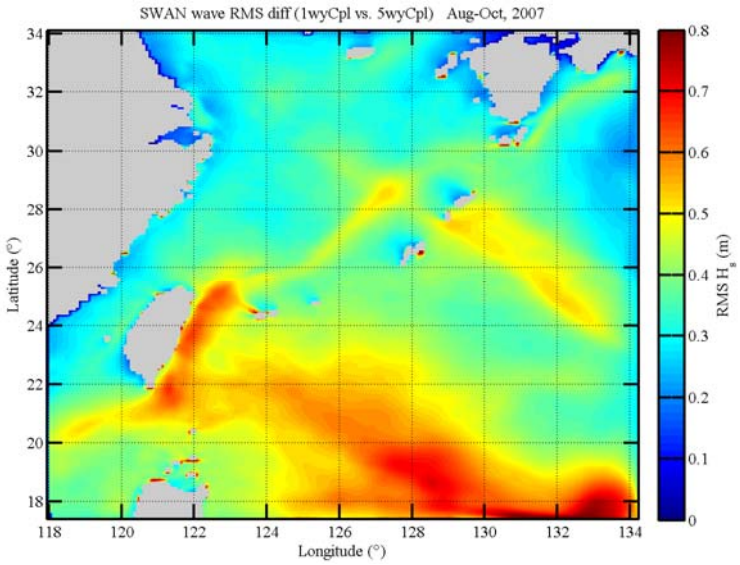

Figure 3.2-5: SWAN significant wave height RMS difference between the uncoupled vs. the 5-way coupled cases for August through October 2007.

In addition to the three month long-term average statistics, we also evaluated the ocean-wave impact during those strong wind (typhoon) events. Figures 3.2-6 to 3.2-9 depict the wind speed, wave heights and satellite altimeter data in the successive typhoon events Sepat, Nari, Wipha, and Krosa. Coupling shows improvement in predicted wind and waves in terms of CC and RMSE during typhoon Sepat and Wipha. Little or no improvement was noticed in the other two events.

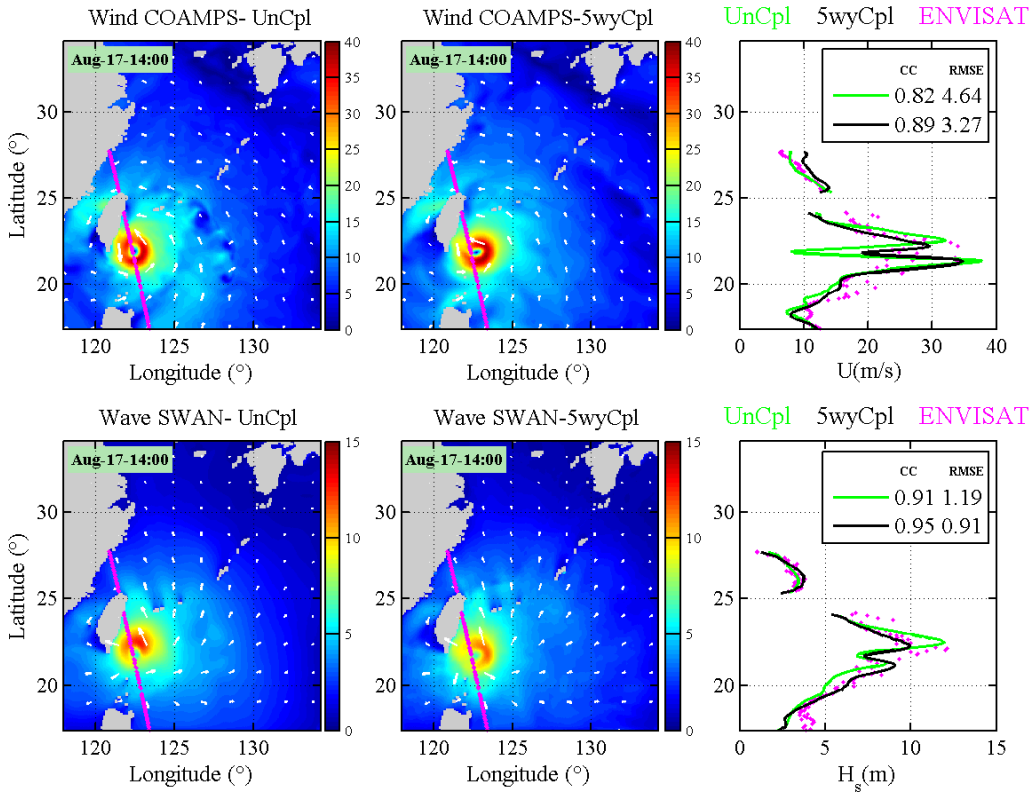

Figure 3.2-6: COAMPS wind speed and direction (top) and SWAN wave magnitude (bottom) for the uncoupled (left column) and 5-way coupled (middle column) simulations. Plots (right column) of model comparisons with uncoupled COAMPS (green) and 5-way coupled (black) against ENVISAT observations (pink), are shown for 17 August 2007 during Super Typhoon Sepat.

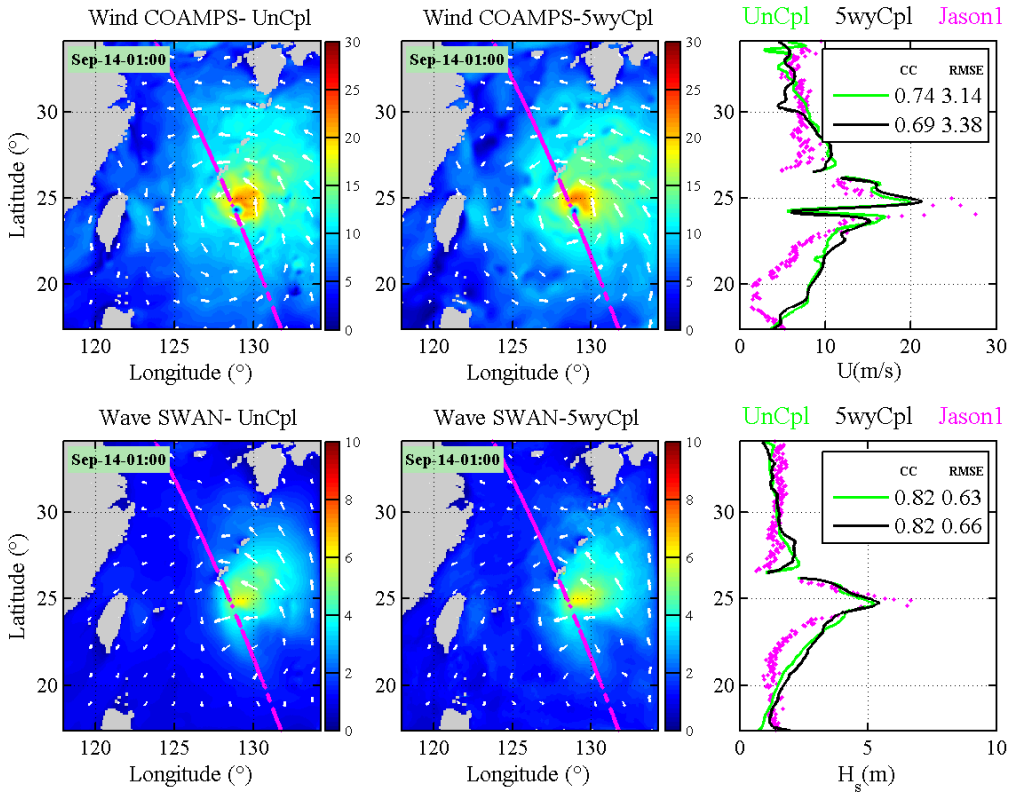

Figure 3.2-7: COAMPS winds (top) and SWAN waves (bottom) during Super Typhoon Nari on 14 September 2007, for the uncoupled (left column) and 5-way coupled (middle column) runs. Plots of model comparisons (right column) for the uncoupled run (green) and 5-way coupled run (black) with Jason1 observations (pink).

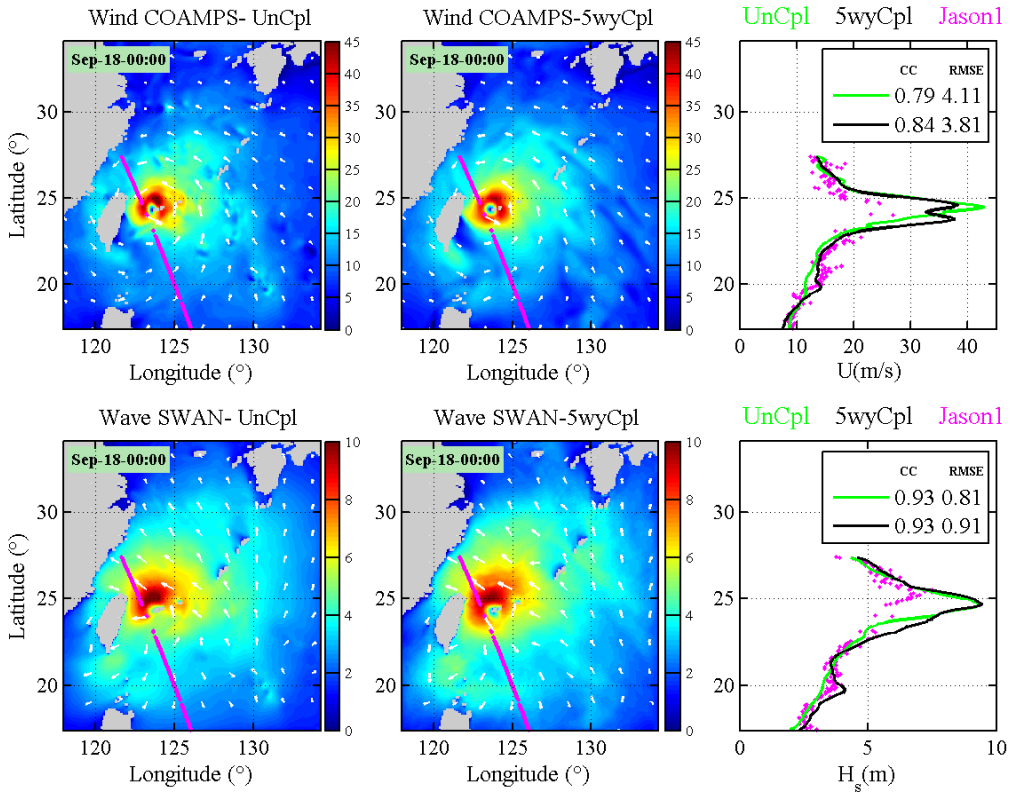

Figure 3.2-8: Typhoon Wipha wind from COAMPS (top) and wave from SWAN (bottom) 18 September 2007, uncoupled (left), 5-way coupled (middle). Model comparisons (right) - uncoupled (green), 5 way coupled (black) with Jason1 observations (pink).

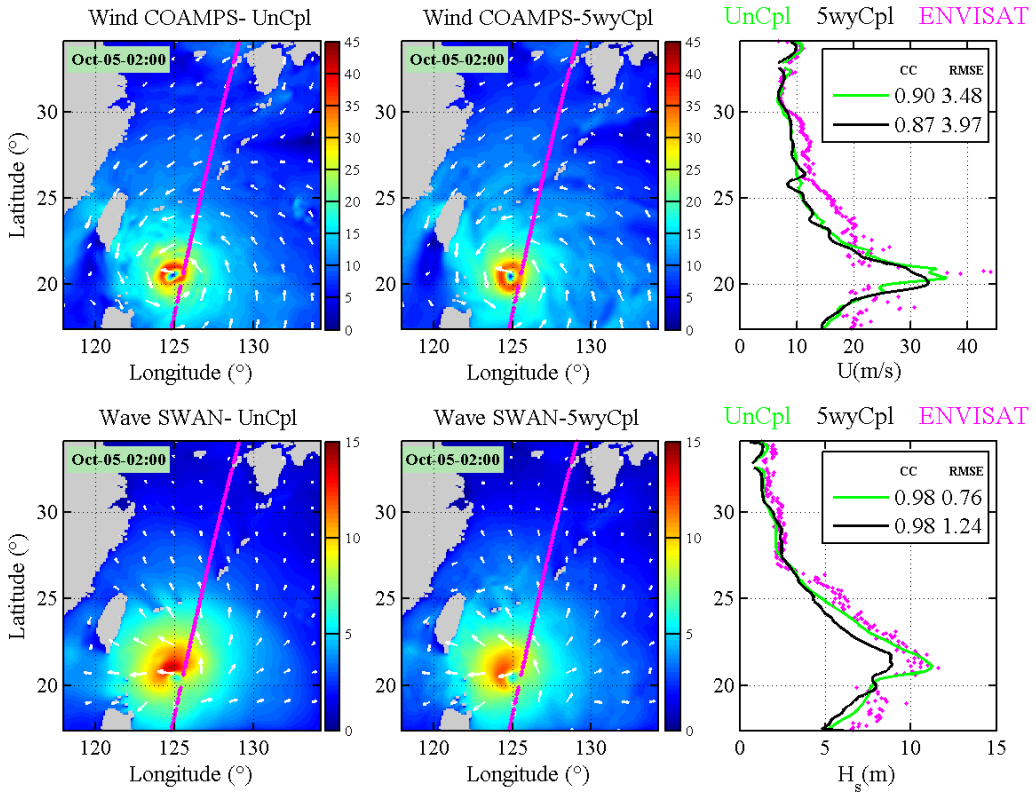

Figure 3.2-9: Typhoon Krosa wind from COAMPS (top) and wave from SWAN (bottom) 5 October 2007, uncoupled (left), 5-way coupled (middle). Model comparisons (right) - uncoupled (green), 5-way coupled (black) with ENVISAT observations (pink).

3.2.4.3 Impact of Ocean-Wave Coupling on SST

The impact of ocean-wave coupling on sea surface temperature was evaluated. Figure 3.2-10 shows snapshots of COAMPS predicted SST on August 21, 2007, two days after the passage of typhoon Sepat. The typhoon-induced SST cooling and cold wake were clearly observed in both uncoupled and coupled cases. In addition, both cases showed upwelling in Taiwan's east coast and the cold dome of the NE coast of Taiwan along the Kuroshio path. In the coupled case with ocean-to-wave coupling, the upwelling and surface cooling effects were more pronounced. The SST cooling due to the typhoon passage was also verified with satellite-derived SST fields. The AMSR-E and TMI derived SST on the same date are shown in Figures 3.2-11 and 3.2-12, respectively. It should be noted that in both cases NCOM SST was fed back to the atmospheric COAMPS model.

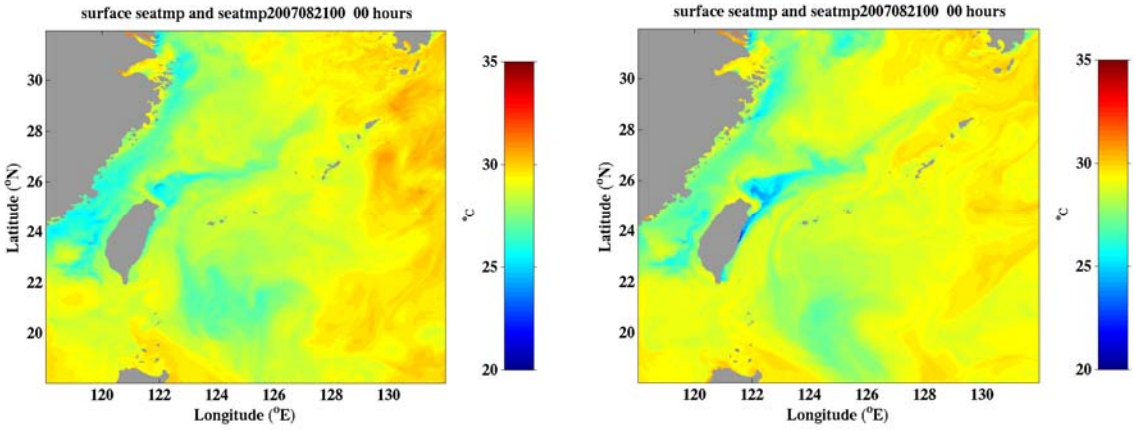

Figure 3.2-10: SST in Okinawa Trough region – uncoupled (left), 5-way coupled (right).

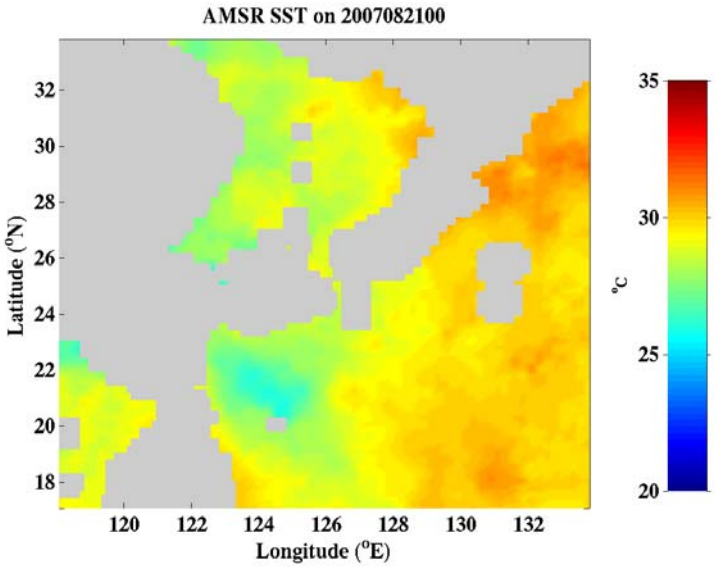

Figure 3.2-11: AMSR-E derived SST in Okinawa Trough region on 8/21/2007.

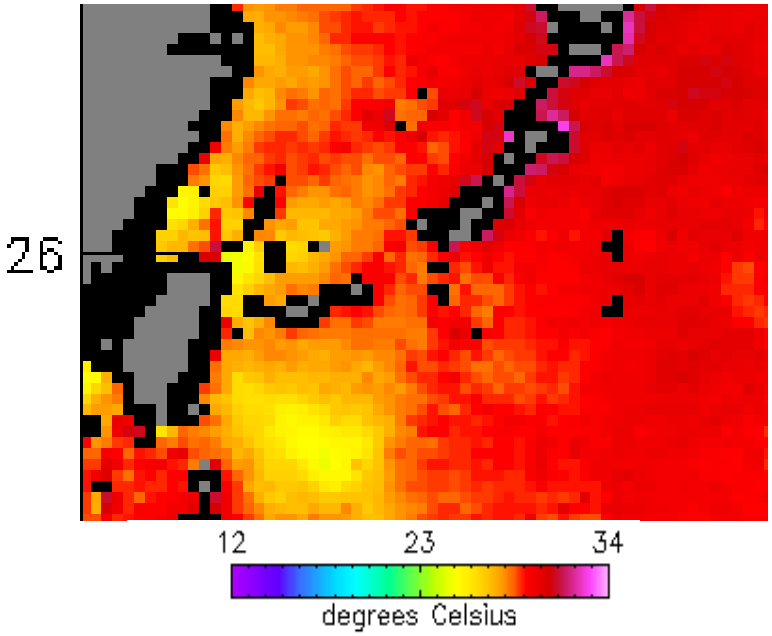

Figure 3.2-12: TMI derived SST in Okinawa Trough region on 8/21/2007.

3.2.4.4 Impact of Ocean-Wave Coupling on Currents

Improvements in surface ocean current prediction using ocean-wave coupling schemes during a typhoon are described here. Figure 3.2-13 shows the surface current field on October 6, 2007, when Typhoon Krosa crossed the Kuroshio path near northern Taiwan. Two interesting features due to wave coupling were found: 1) the enhancement of Kuroshio surface currents, and 2) the reduced coastal jet velocity near the Chinese coast. Both features contributed to the improvement of surface current simulation by incorporating more complete physics and coupling with the wave model.

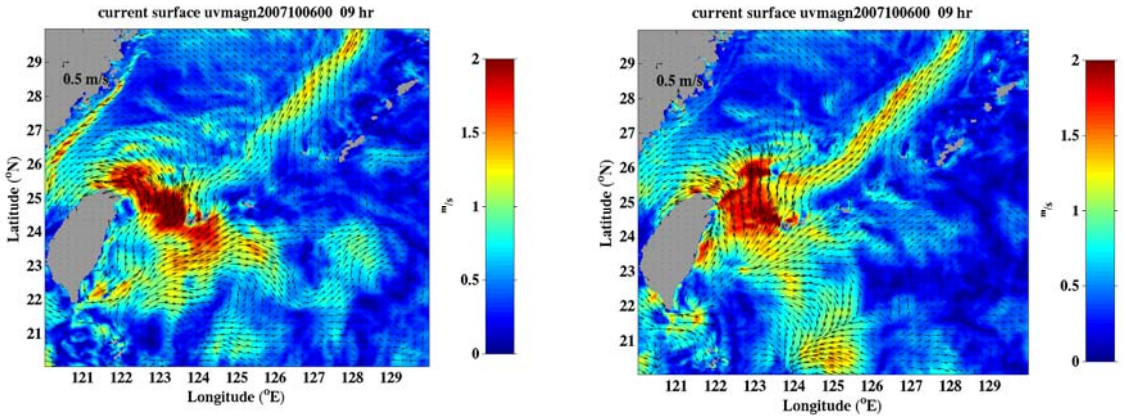

Figure 3.2-13: Surface currents in Okinawa Trough region for uncoupled (left) and 5-way coupled (right) with NCOM.

3.2.4.5 Surface Current Validation Statistics

Improvements in surface ocean currents from the COAMPS runs were evaluated by using surface velocity fields from the prediction systems to advect simulated drifters. For validation, a set of World Ocean Circulation Experiment (WOCE) drifter trajectories (1035 observations) was used to compute the average distance between actual drifter locations and the 12 hour forecast predicted values during the model time frame. This is a high-quality data set that has been hand-edited for quality control and sampling bias. The simulated drifters were inserted into the model velocity field at the start times and locations of the observed drifter trajectories. At the end of the 12 hour forecast, the difference between the final locations of the simulated and actual drifters was used to compute an average error.

Figure 3.2-14 shows a total of 14 drifter buoy trajectories in the model domain during the four month validation period. The black dots indicate the starting locations of the drifters. Table 3.2-3 shows the validation statistics comparing the COAMPS runs with drifter observations. The errors of the simulated drifters' predicted locations from the 12 hr forecast were similar for the 4-way coupled (13.16 km) and 5-way-coupled (13.13 km) runs, with both cases performing better than the uncoupled 16.66 km separation. The 5-way coupled case exhibited a slightly larger standard deviation as it incorporated wave effects and increased variability accordingly. These errors were similar to other studies that used these validation statistics (Barron et. al., 2007).

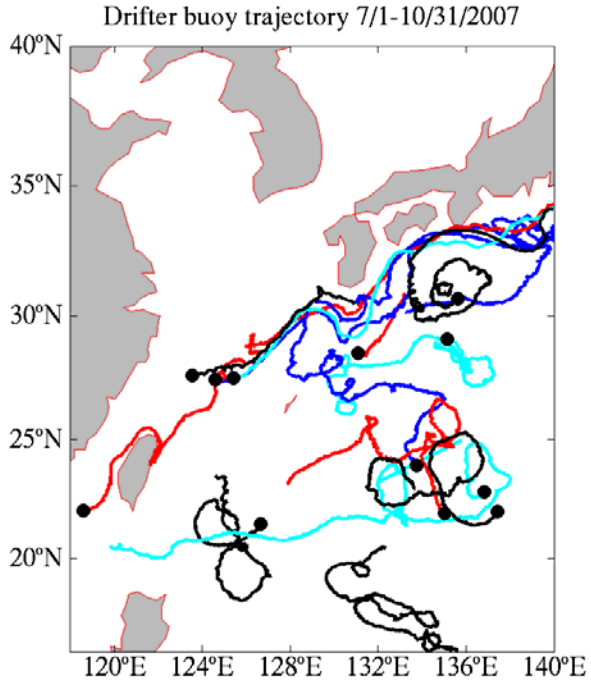

Figure 3.2-14: Trajectory paths for 14 WOCE drifter buoys from 7/1 through 10/31/2007.

Table 3.2-3: Surface current validation statistics for NCOM Okinawa Trough 24 h forecasts as compared to WOCE drifter observations. N= Number of drifter observations.

NCOM 24 hr Forecast	N	Mean (km)	Std Dev.
uncoupled	1035	16.66	11.78
4-way	1035	13.16	9.36
5-way	1035	13.13	9.70

3.2.4.6 Impact of Ocean-Wave coupling on Sonic Layer Depth and Surface Layer Trapping

The impact of ocean-wave coupling on SLD, surface layer trapping, and associated acoustic properties has been evaluated using profile observations containing both temperature and salinity. NRL's ProfParam software (Helber et al, 2008) was used to calculate SLD and associated parameters. Additional background information can be found in Smith et al. (2011). Histograms and scatter plots of the SLD and surface layer trapping are shown in Figures 3.2-15 and 3.2-16. Statistics are provided in Table 3.2-4. The narrow bell-shaped distributions in the histograms indicate overall improvement in the coupled case. The higher frequency (18% vs. 13%) at zero also shows improvement due to coupling.

Perhaps the most significant improvement in the coupled simulation over the uncoupled runs can be seen in the correlation coefficient and slope of the SLD scatter plots (Figure 3.2-16). Root mean square error and bias were also smaller. (Table 3.2-4). The ability of the coupled COAMPS to more accurately predict SLD could be attributed to 1) improved temperature prediction, 2) improved wave physics and/or 3) the improved vertical mixing turbulence scheme, all due to the incorporation of the SWAN wave model.

The coupled model also demonstrated an enhanced ability to predict acoustic related properties such as surface layer trapping of acoustic frequencies. "Stoplight maps", using red, yellow and green colors to represent surface trapping are shown in Figure 3.2-17. The green line represents true positive, where at a given frequency both the data and model indicate the presence of trapping. Red represents false positive, where observations exhibit no surface layer trapping but the model does. Yellow represents false negative where the data indicates trapping but the model fails to predict it. Black is true negative where both data and model reveal no trapping. The sum of all four occurrence percentages should equal 100% at any given frequency. Good agreement is indicated by high true positive and high true negative, along with low false positive and false negative rates. Coupling increased the true positive from 48 to 55% and reduced false positive and false negative rates, from 32% to 24% and from 8% to 5%, respectively.

Histograms were plotted to show the combinations of model- and observation-derived SLD on a 5 m resolution grid. A good agreement between the data- and model-derived SLD should have more counts concentrated along the 45° diagonal line from the lower left to upper right

corner and less spread on the plot. Figure 3.2-18 demonstrates that the coupled case produced a better overall SLD prediction.

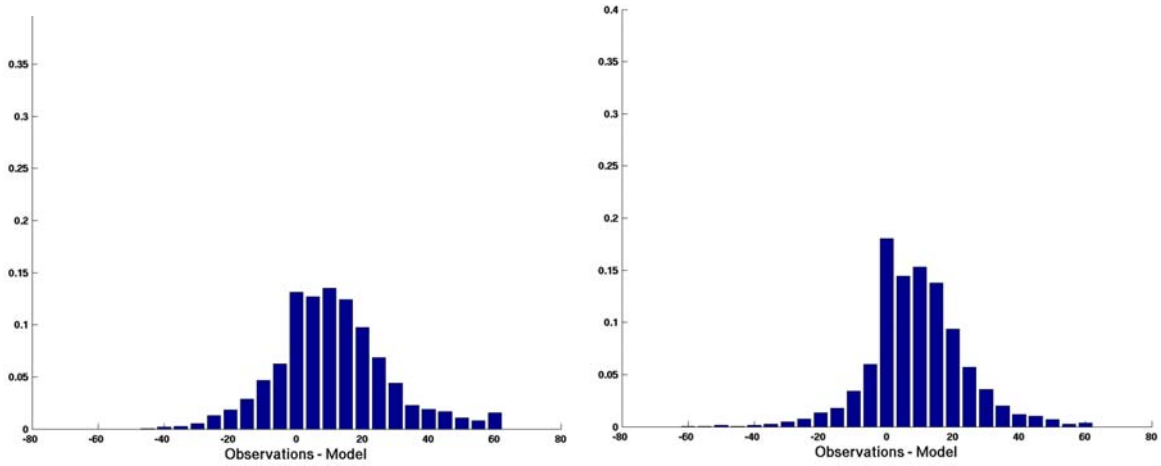

Figure 3.2-15: Histogram of observation minus model SLD differences for the uncoupled (left) and coupled (right) COAMPS 12 hr forecast.

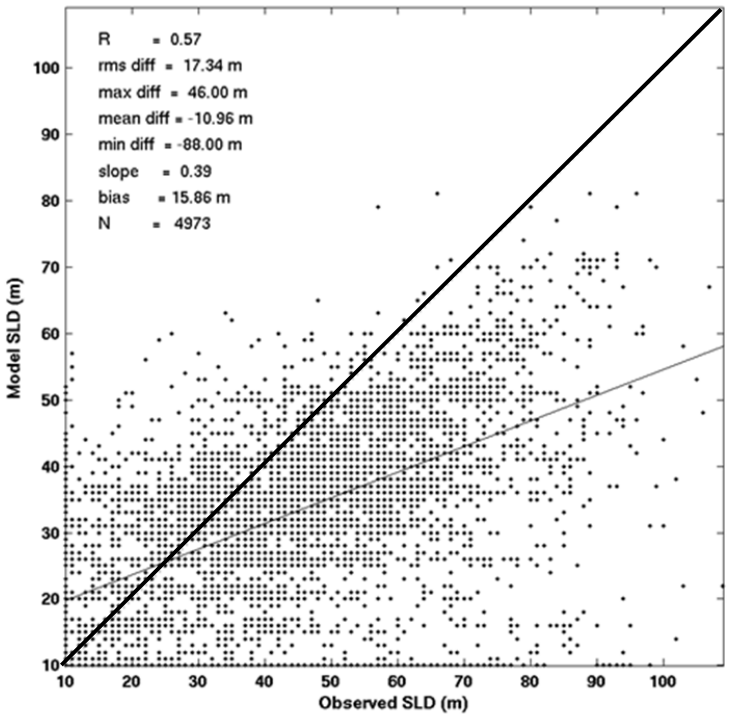

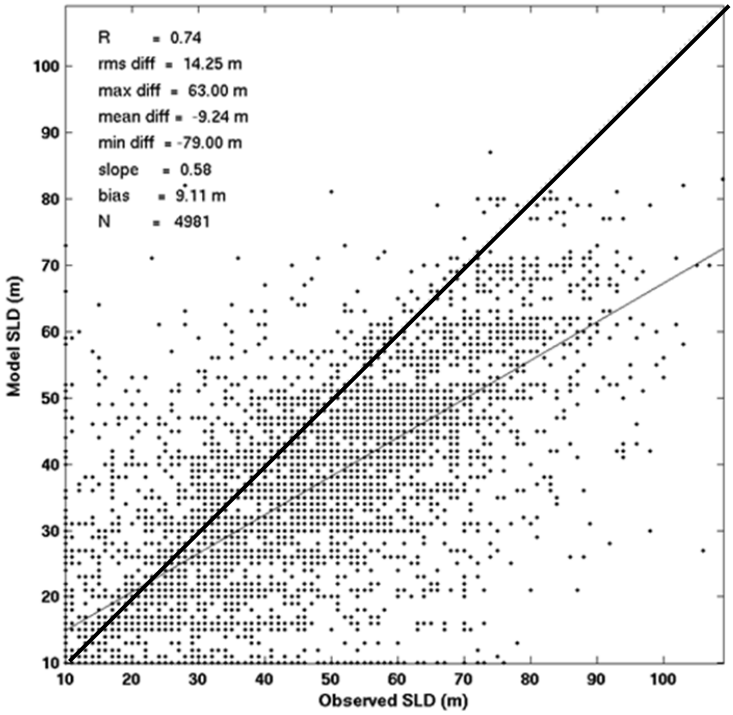

Figure 3.2-16: Scatter plot and statistics of sonic layer depth for the uncoupled (top) and coupled (bottom) COAMPS 12 hr forecast. Solid black line indicated perfect (r=1.0) agreement.

Table 3.2-4: Statistics summary of sonic layer depth.

	CC	RMSE	Mean diff	Slope	Bias	N
Uncoupled	0.57	17.34	-10.96	0.39	15.86	4973
Coupled	0.74	14.25	-9.24	0.58	9.11	4981

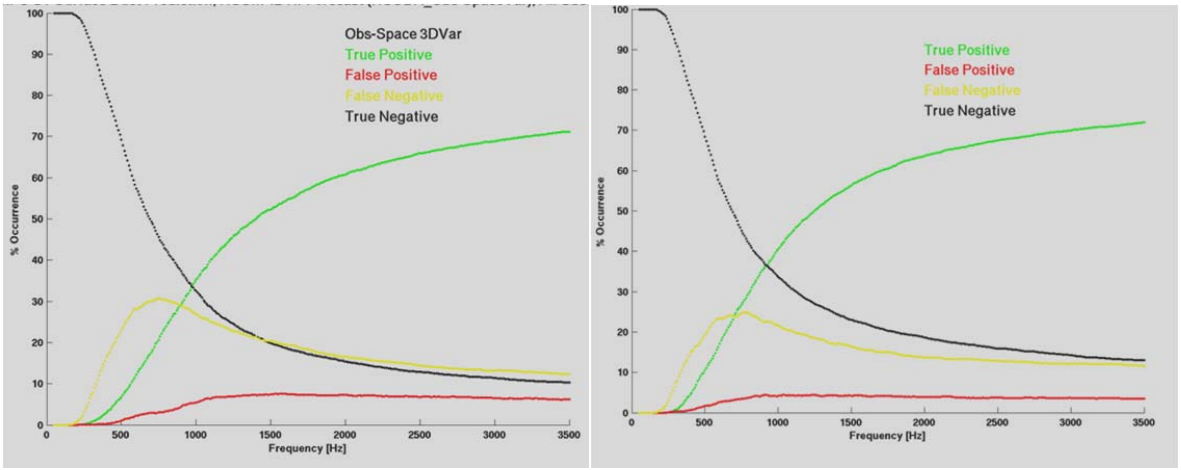

Figure 3.2-17: Uncoupled (left) and 5-way coupled (right) surface duct prediction acoustic frequencies (Hz).

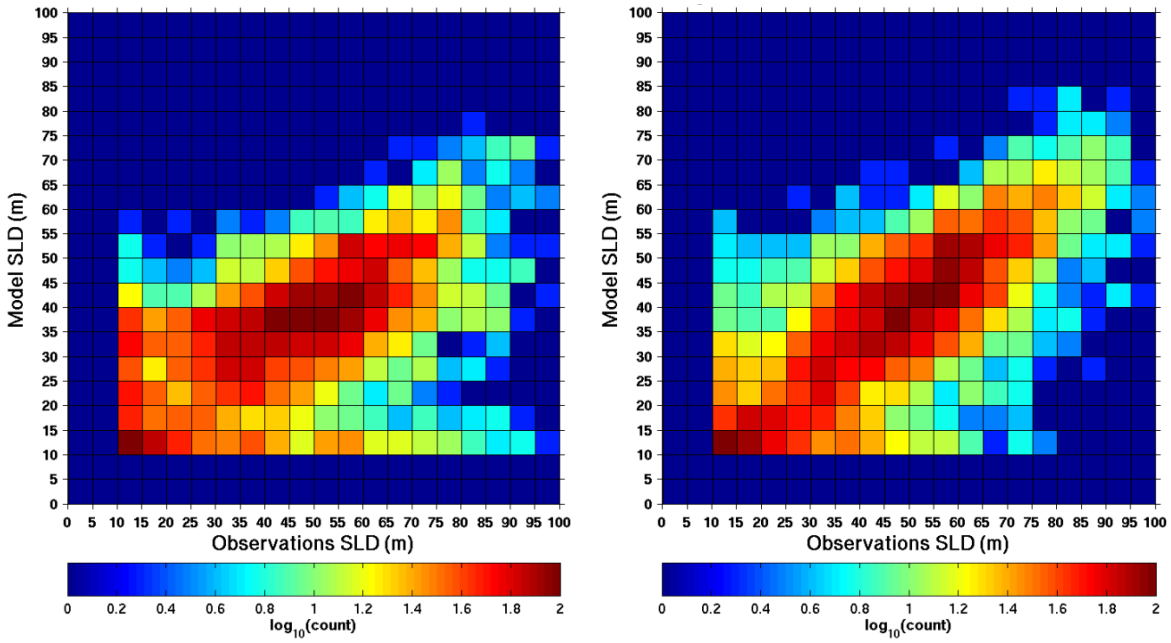

Figure 3.2-18: Sonic layer depth histogram for uncoupled (left) and 5-way coupled (right) COAMPS 12 hr forecasts.

3.3 Test Case 3: Florida Straits

3.3.1 Purpose

The purpose of Test Case 3 was to explore wave/current interactions in the Florida Straits. The velocity of the Florida Current exceeds 1.5 m/s as it flows past the Florida Keys and into the Atlantic Ocean. It has significant impact on the propagation of swell through refraction.

In order to investigate the impact of currents on the waves, local waves, growing at differing rates near the core of the boundary current, were compared to waves in weaker currents in surrounding regions. COAMPS simulations were performed with and without currents included in the SWAN wave model. To investigate the influence of waves on mixing and the role of Stokes drift, COAMPS runs were conducted both with and without wave feedback from SWAN to NCOM.

3.3.2 Test Area and Observations

The Florida Straits connect the Gulf of Mexico with the Atlantic Ocean, separating Florida and Cuba. The Florida Current, part of the Gulf Stream, flows through them. The total length of the straits exceeds 300 miles and the width varies from 60 to 100 miles. The main channel is roughly 6,000 feet deep. The core of the Florida Current lies both at and just below the surface, flowing at peak speeds of three to five knots, or 30 million cubic meters per second, along 15 to 30 miles of the coast of Florida.

The bathymetry in this area is characterized by a shallow shelf from 5 km to 15 km offshore. There is a sharp slope beyond the shelf, with depths increasing such that surface waves are no longer influenced by bathymetry.

The COAMPS model validation results were compared with in situ observations for the period from April 1 to May 18, 2005. The in situ data were collected by the Rosenstiel School of Marine and Atmospheric Sciences (RSMAS). Instruments were positioned outside of Biscayne Bay, Miami, recording waves and currents at five point locations. A summary of the data types and deployment time periods are listed in Table 3.3-1.

In situ sensors (ADCPs and buoys) provide robust and reliable wave and tide data, albeit with limited spatial coverage. The high shear area on the inshore edge of the Florida Current is well characterized by Wellen Radars (WERA). The WERA radar data blanketed the Florida Straits from Key Largo to Ft. Lauderdale, FL as a project of the Southeast Atlantic Coastal Ocean Observing System (SEACOOS) (Voulgaris et al., 2008) and the University of Miami. The WERA system uses a linear phased-array receiver and frequency modulated continuous wave (FMCW) transmission. The two high frequency Wellen radars (WERA HF), located at Crandon Park (CDN 25°42.84'N, 80°9.06'W) on Key Biscayne and North Key Largo Hammocks Biological Preserve (NKL 25°14.46'N, 80°18.48'W) were separated by a distance of approximately 55 km. The depths recorded by the instruments at the locations did not match those generated by the model at corresponding locations; model depths were overestimated on the Florida shelf. To resolve this issue, comparisons were made between observations and model values at model locations slightly west of the actual locations, where the model depth was shallower and more consistent with the measured depths of the in situ instruments. These locations are located inside the blue rectangle in the left panel of Figure 3.3-3, which is expanded in the right panel. See Gravois et al. (2012) for a comprehensive explanation of the WERA data, its spatial coverage, processing, calibration and filtering.

3.3.3 Model Setup

COAMPS was run in a fully coupled mode with three nested atmospheric grids of 18 km, 6 km and 2 km resolution, respectively. All grids had 60 vertical levels. The atmospheric model was initialized using the 0.5° NOGAPS (Hogan and Rosmond 1991), which also provided boundary conditions during the simulation. Atmospheric data assimilation using the Navy Data Assimilation System (NAVDAS) was run with a 12-hour analysis cycle. Heat flux, wind stress, and net fresh water flux were used to force NCOM.

Three wave model grids were used for this validation effort. WAVEWATCH III™ (WW3, Tolman 2009) is run on the outermost grid (wave grid 1) with wind forcing from NOGAPS archives and Digital Bathymetry Data Base (DBDB2) bathymetry. The resolution of wave grid 1 conveniently matches the wind fields in NOGAPS archives[2]. Another run is made with WW3 on wave grid 2 using boundary conditions generated from the wave grid 1. The wave grid 2 also employs DBDB2 bathymetry but is forced by COAMPS. The SWAN wave model is run on wave grid 3 fully coupled with Navy Coastal Ocean Model (NCOM) and COAMPS. The

[2] The resolution also matches the global WW3 used by the Fleet Numerical Meteorology and Oceanography Center (FNMOC)

wave grid 3 is forced at the boundaries with wave spectra from WW3 grid 2 outputs. A summary of the three grids is given below, and plotted in Figure 3.3-1.

wave grid 1: WW3
- $\Delta x = \Delta y = 0.5° \approx 55$ km
- Longitude: x = -100° to -0.5° W (260° to 359.5° E), nx =200
- Latitude: y =17° to 59° N, ny =85
- no boundary forcing

wave grid 2: WW3
- $\Delta x = 4' \approx 6.5$ km
- $\Delta y = 4' \approx 7.4$ km
- Longitude: x = -90° to -72° W (270° to 288° E), nx =271
- Latitude: y =21.2° to 40° N, ny =283
- boundary forcing from grid 1

wave grid 3: SWAN
- $\Delta x \approx 0.01° = 1$ km
- $\Delta y \approx 0.009° = 1$ km
- Longitude: x = -80. 8 to -78.8° W (279.2° to 281.2° E), nx =201
- Latitude: y =23.6° to 27.2° N, ny =401
- boundary forcing from grid 2

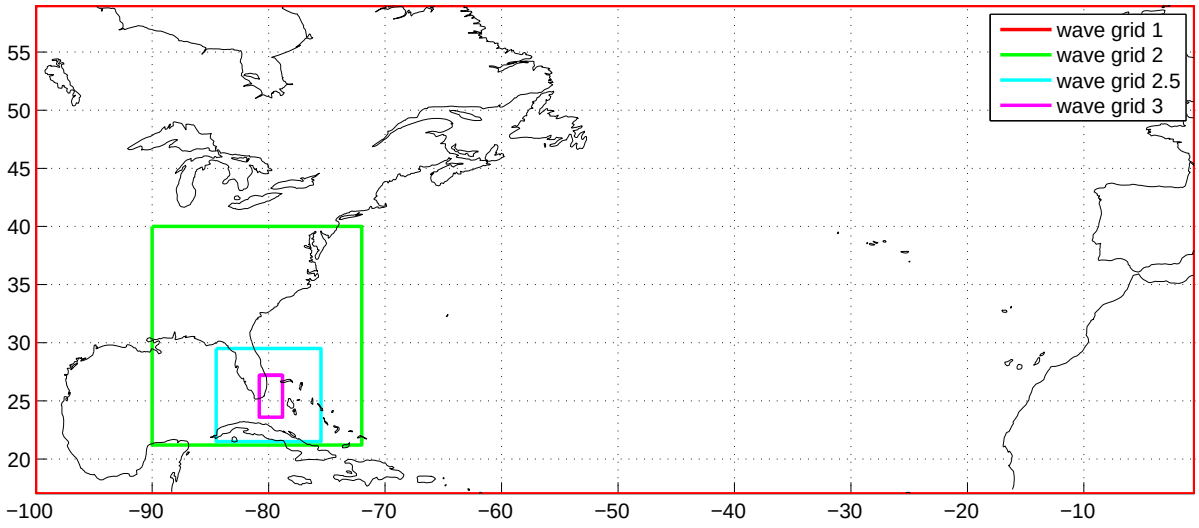

Figure 3.3-1: Geographic locations for the telescoping set of nested wave grids. Outer wave grids 1 and 2 are run on WW3 with NOGAPS and COAMPS wind forcing respectively. Inner wave grid 3 is run with SWAN as part of the fully coupled COAMPS model. Separate from the coupled model system, SWAN runs were made with grid 2.5 and grid 3 to investigate swell transmission into the in situ data area. This setup and results are not discussed here, but given in Gravois et al. 2012.

NCOM was set up with an innermost nest resolution of 1 km in the area between -80.82° to -78.8°W and 23.6° to 27.2°N (203x401 grid points). It had 50 vertical levels and eight tidal constituents, with the initial and boundary conditions provided by 1/8° global NCOM. The NCOM also contributed SSTs to the atmospheric model, and surface currents and sea level to the wave model, SWAN. As additional forcing to the ocean model, SWAN provided wave-induced stress, Stokes drift currents and bottom stress. The coupling between models was performed every six minutes. The NCOM setup is shown in Figure 3.3-2.

ocean grid 1: NCOM

- Δx = 0.03° = 3 km
- Δy = 0.027° = 3 km
- Longitude: x = -82.5° to -77.0° W (277.5° to 283.0° E), nx =185
- Latitude: y =22.9° to 29.8° N, ny =258
- boundary forcing from GNCOM

ocean grid 2: NCOM

- Δx = 0.01° = 1 km
- Δy = 0.009° = 1 km
- Longitude: x = -80. 82° to -78.8° W (279.2° to 281.22° E), nx =203
- Latitude: y =23.6° to 27.2° N, ny =401
- boundary forcing from ocean grid 1

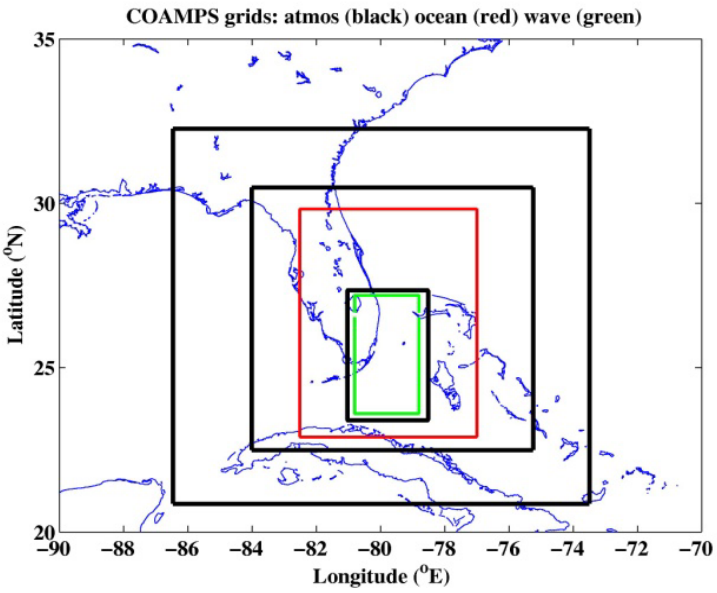

Figure 3.3-2: Area covered by model grids. Boundaries for the three atmospheric grids are shown with black lines. The red box denotes the NCOM 3 km grid. The green box denotes the identical NCOM and SWAN 1 km grids.

3.3.3.1 Explanation of validation data

Several papers describing H-F radar measurements of waves were utilized during this study. A list of these papers, along with some other relevant references, is given here:

- Haus (2007): a study of fetch-limited growth; southeast Florida; December 2005.
- Haus et al. (2010): analysis of accuracy of wave heights from WERA; southeast Florida; calibration: YD 78-99 2005; Validation: YD 100-145 2005, in situ data used.
- Ramos et al. (2009): wave heights from several radars: North Carolina (SHOWEX, DUCK94) and Chesapeake Bay (COPE3)
- Shay et al. (2007): WERA surface currents; west Florida; August and September 2003.
- Shay et al. (2008) : primarily about surface currents, with some discussion of waves at several locations: west Florida, southeast Florida, and North Carolina,
- Voulgaris et al. (2008): wave measurements, including radar; southeast Florida radar, the "Mini-Waves Cal-Val experiment", YD 75-145 2005, discussion of calibration, wave height and some directional spectra.
- Gurgel (1999), Wyatt et al. (1999, 2003), Caires (2000) : early European wave measurements with HF radar

During the period of this study in-situ data were collected RSMAS. These instruments were positioned outside of Biscayne Bay, Miami and recorded waves and currents at five locations. A summary of the data types and deployment time periods are listed in Table 3.3-1. Latitude and longitude pairs for each instrument location are given. As explained in 3.3.2, comparisons between model and in-situ measurement were done at slightly different locations to match the observed and model depths. These locations are located inside the blue rectangle in the left panel of Figure 3.3-3 which is expanded in the right panel.

Table 3.3-1: RSMAS in situ data summary.

	Start	End	Gauge	True Lat	True Lon	Model Lat	Model Lon	Depth (m)	1D spectra	2D stats	T mean	T peak
C1	03/26	05/18	RDI ADCP	25.5006	-80.1101	25.5008	-80.1173	10	yes	yes	yes	yes
C3	04/05	06/05	TAB N	25.4991	-80.1025	25.4990	-80.1108	15	no	no	yes	yes
C4	03/20	06/04	SONTEK ADP	25.4987	-80.1087	25.4987	-80.1189	8.8	no	no	yes	no
C7	04/05	05/28	TAB S	25.4358	-80.1170	25.4359	-80.1251	15	no	no	yes	yes
C8	03/26	06/04	RDI ADCP	25.4705	-80.1134	25.4707	-80.1246	9	yes	yes	yes	yes

In addition to the in situ data, field measurements were also taken by a pair of WERA HF radars operated by RSMAS. The spatial coverage of the wave height radar data extends roughly 50 km from the radar stations and spans over a 120 degree field of view centered on the bore-sight-angle. The bore-sight-angles were approximately 125° and 90° clockwise from North for the CDN and NKL stations respectively. The radar field grid spacing is regular at 1.2 km in both east-west and north-south directions. The maximum range for radar wave measurements extends less in the radial direction compared to radar ocean surface current measurements. The

WERA HF wave measurement areas are shown in the left panel of Figure 3.3-3.

Three Coastal-Marine Automated Network (CMAN) stations from the NDBC and one National Ocean Service (NOS) tide stations lie within the wave grid 3 domain and were used for validation of the model winds and tides. These NOAA stations are shown on the left panel of Figure 3.3-3.

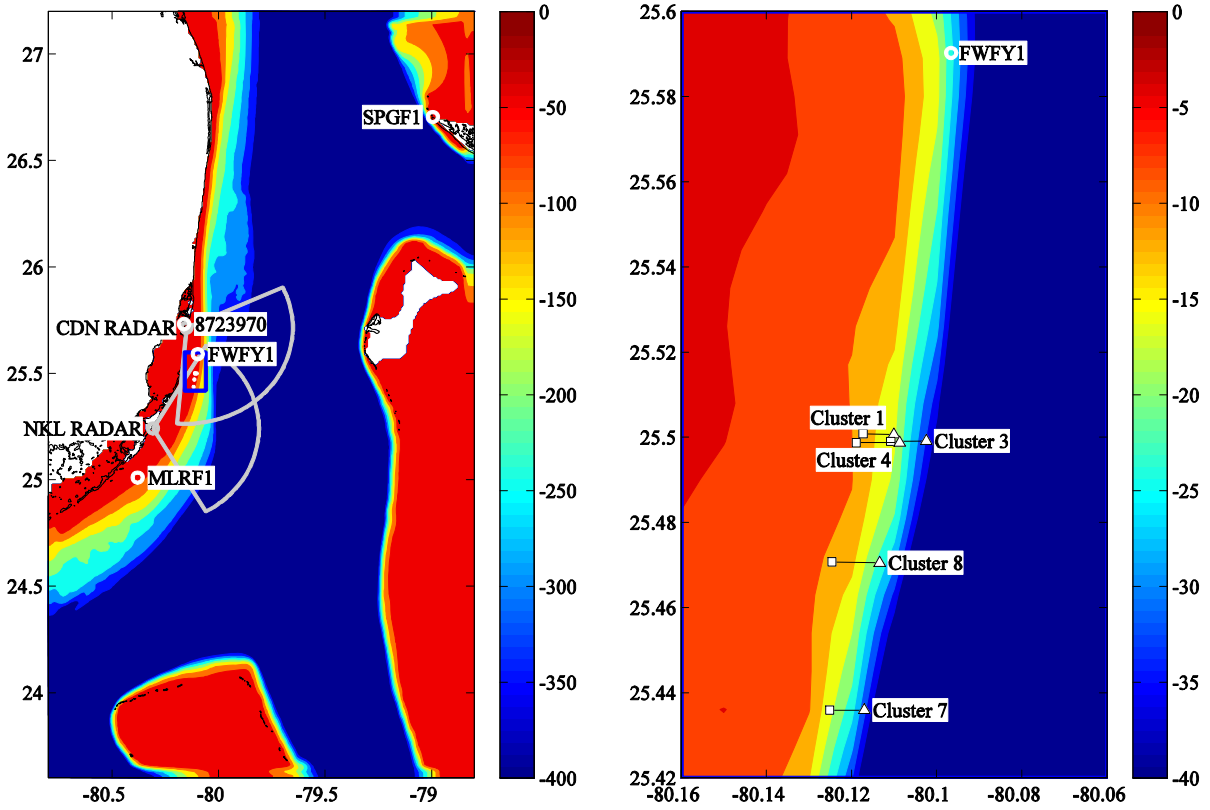

Figure 3.3-3: The left panel shows the model water depth used by grid 3 with the two WERA HF stations CDN and NKL marked with their respective swath wave sensing ranges. The NDBC CMAN stations SPGF1, FWFY1, MLRF1 and NOS tide station 8723970 are also labeled. The small blue box in the left panel is expanded in the right panel, showing each in situ location detailed in Table 3.3-1. The triangles represent the actual location and the squares are the theoretical model locations. The bathymetry is based on GEODAS coastal relief near the US coast, combined with DBDB2 offshore (Jensen et al., 2011).

3.3.4 Results

3.3.4.1 Model validation against in situ measurements

Wave height, direction and peak period from the model were compared with the measured in situ data. Tabulated statistics for the wave height comparisons are shown in Table 3.3-2 and plots of the data are shown in Figures 3.3-4 through 3.3-8. (Statistics are for the period 01-Apr-2005 00:00:00 to 15-May-2005 23:00:00). Correlations were slightly better at the TAB stations

which were in deeper water. Three notable events occur with waves approaching 1.5 m. The event starting around April 6 was captured by the model quite well. However, in the other two events occurring around April 3 and April 17 (the latter being the more significant event), the wave model over-predicts the wave height. The two over-predicted events have mean wave directions from the north-northeast (NNE) and there is a long period swell component. The April 6 event that was modeled better did not have a long period swell component and the mean wave direction was from the east, meaning that this well-predicted energy was probably wind sea generated inside the SWAN domain (grid 3).

The wave height over-prediction in the model for the two swell events (April 3 and 17) was not fully artificial; the WERA HF data also shows large waves for these events in the deeper water. This highlights the limitation of the point in situ measurements: they are not representative of offshore waves because the wave field is not homogeneous.

Perhaps the most credible explanation for the over-prediction is that the modeled waves at the in situ locations are sensitive to the wave angle at the model boundary. This was the conclusion of Rogers et al. (2007) who found for a SWAN hindcast of similar scale that even though the wave height of their boundary forcing was quite accurate, the internal sheltering (blocking) by islands and other topographic features meant that the wave direction is also critically important: so much so, in fact that the wave height predictions at sheltered locations were sometimes severely biased due to errors in the directional distribution of the (otherwise accurate) boundary forcing.

The present simulation is also expected to be very sensitive to wave direction, again because of the amount of sheltering by islands and shoals. The mean wave directions reported by the in situ instruments indicate a measured mean wave direction slightly closer to north than in the model for the April 17 event. This may have had an impact on the model's over-prediction of the waves. In the real ocean, swells propagating toward the in situ data region from a northerly direction would have been turned into the coast by refraction, and therefore not reach those instruments. The same swell field propagating toward the radar would be in deeper water and therefore more likely to reach the radar (less likely to be trapped by refraction). In the model, the swells were propagating from a less steep angle (NNE) and so could penetrate into both regions (shallower in situ data region and deeper radar region). The model depths are deeper than the actual depth near the coast, which implies that there is less refraction of swell into the coast and onto the beach than in reality.

The comparison suggests a bimodal regime in the model, with an approximate wind sea of 5 s period and swell around 10 s period. In the observations, the 10 s swell occurs much less frequently than in the model. Thus, at many times, the wave period is overpredicted by the model at the in situ locations. This is believed to be caused by the same problem which leads to overprediction of wave height during April 3 and 17; namely, that swells penetrate into the in situ region in the model, but did not reach this location in the real event.

Table 3.3-2 presents summary statistics for the period of 1 Apr – 15 May 2005 at 5 locations shown in Figure 3.3-3. Comparisons were made for the standalone wave case and when currents from NCOM were included. At all five locations, the bias and RMSE were lower when currents were included and the correlation coefficient was higher.

Table 3.3-2: Statistics of significant wave height in model vs. RSMAS in situ data. Comparisons include a case with wave-ocean coupling disabled. The time period used is the same between the two simulations. The C3 and C7 records start four days into the comparison period. Statistics are for the period 01-Apr-2005 00:00:00 to 15-May-2005 23:00:00. CC is correlation coefficient (r).

	bias	RMSE	CC
C1	0.09	0.23	0.69
C1-no currents	0.18	0.31	0.65
C3	0.08	0.23	0.74
C3-no currents	0.18	0.31	0.67
C4	0.22	0.32	0.68
C4-no currents	0.31	0.41	0.62
C7	0.04	0.19	0.80
C7-no currents	0.13	0.26	0.72
C8	0.13	0.23	0.73
C8-no currents	0.22	0.32	0.67

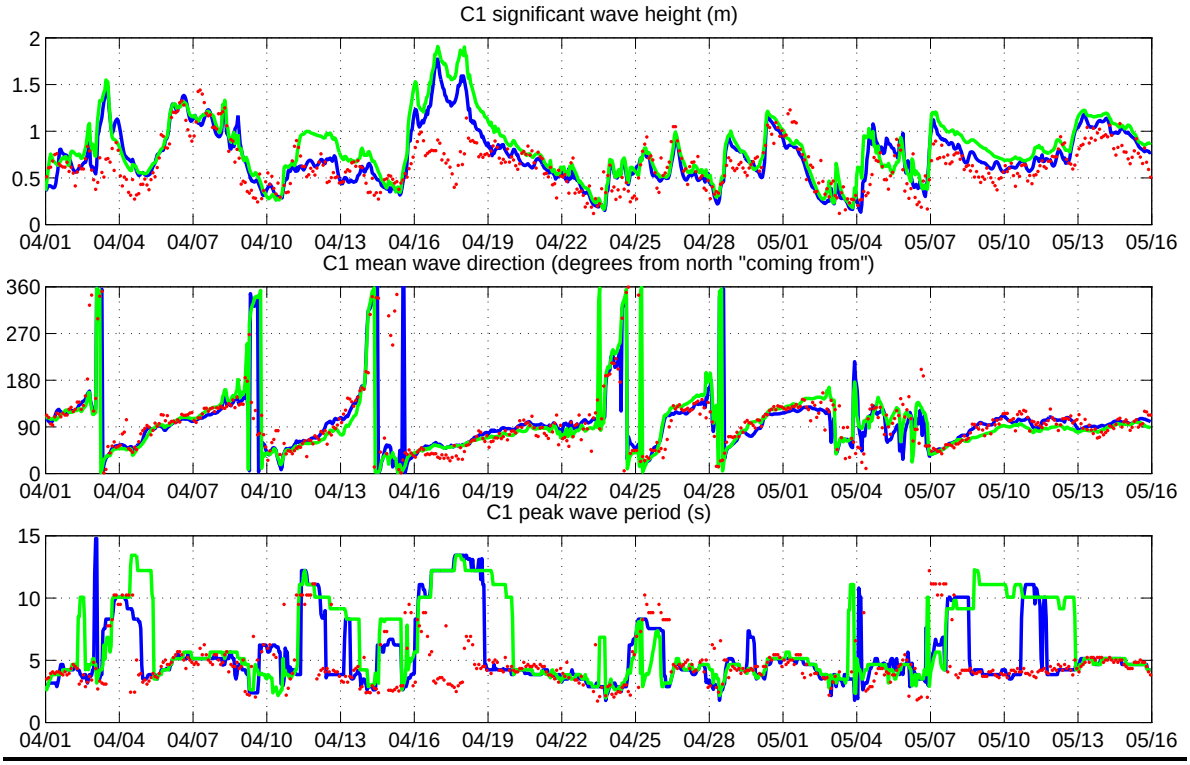

Figure 3.3-4: Model vs. in situ data for the Cluster 1 ADCP in 10 m depth. The April 3 and April 17 events were swell events with energy generated outside of grid 3. The April 6 event was a wind sea event with energy generated inside grid 3. Blue line = control model (currents ingested by SWAN), Green line = SWAN model without currents, Red line = in situ data.

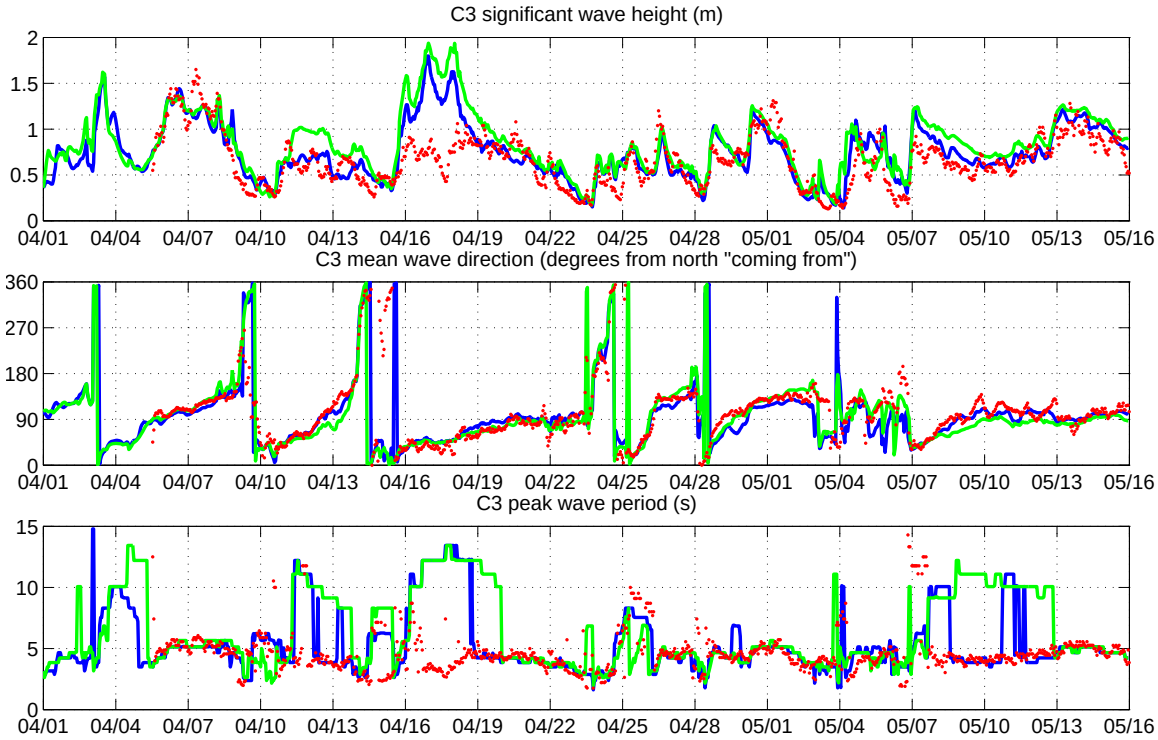

Figure 3.3-5: Model vs. in situ data for the Cluster 3 TAB in 15 m depth.

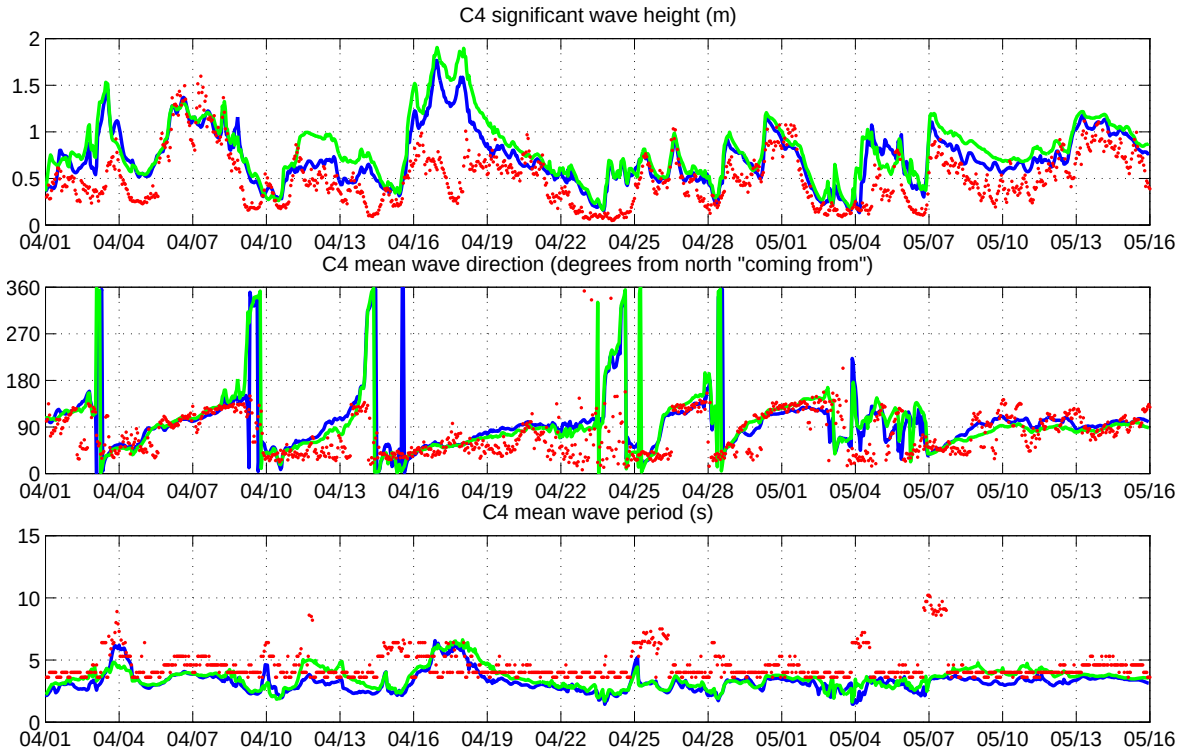

Figure 3.3-6: Model vs. in situ data for the Cluster 4 ADP in 9 m depth. Blue line = control model (currents ingested by SWAN), Green line = SWAN model without currents,

Red line = in situ data.

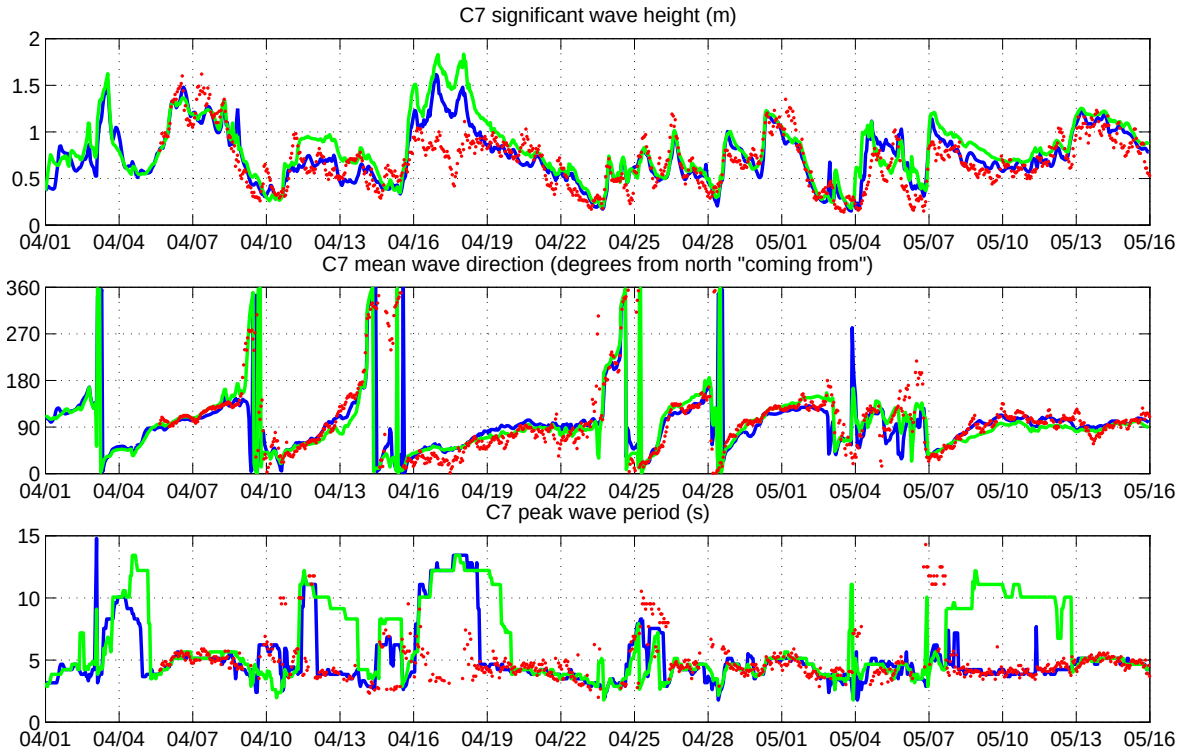

Figure 3.3-7: Model vs. in situ data for the Cluster 7 TAB in 15 m depth. Blue line = control model (currents ingested by SWAN), Green line = SWAN model without currents, Red line = in situ data.

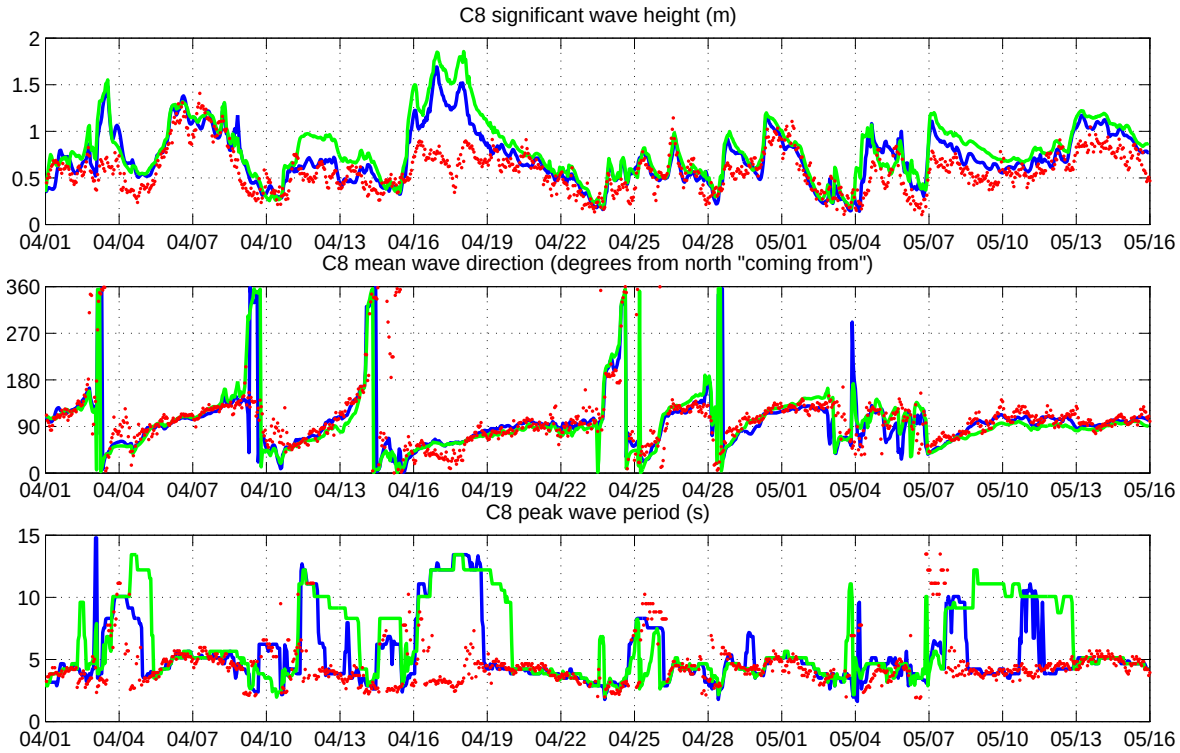

Figure 3.3-8: Model vs. in situ data for the Cluster 8 ADCP in 9 m depth. Blue line = control model (currents ingested by SWAN), Green line = SWAN model without currents, Red line = in situ data.

3.3.4.2 WERA HF Data Filtering, Calibration, and Sector Averaging

A major portion of this work was spent on processing the WERA HF wave measurements. The data was supplied by RSMAS in un-calibrated format with contaminated data points. An automated method to remove contaminated or outlier data was required prior to use in any validation. The procedure in given in Gravois et al. (2012).

After the data was passed through the quality control algorithm the data was then averaged over 1 hour period for all valid data points. After the data was filtered, the fraction of the data points remaining, relative to the original amount (see Figures 3.3-9 and 3.3-10), gives some indication of the spatial distribution of the initial data quality.

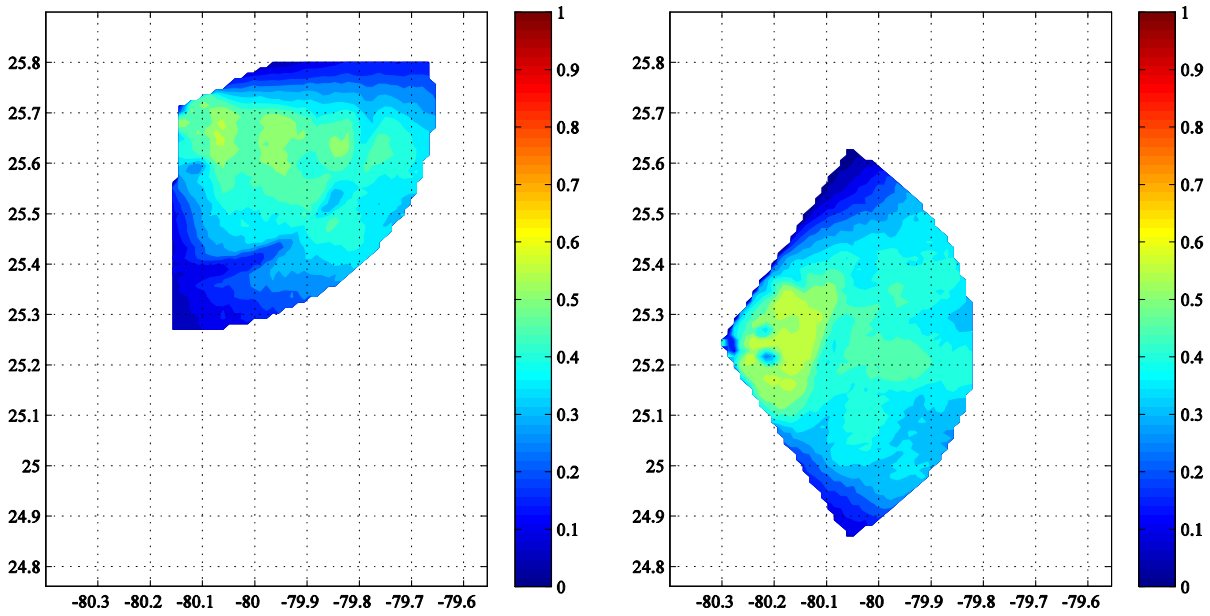

Figure 3.3-9: Fraction of radar data remaining after outlier removal for 20 minute data.

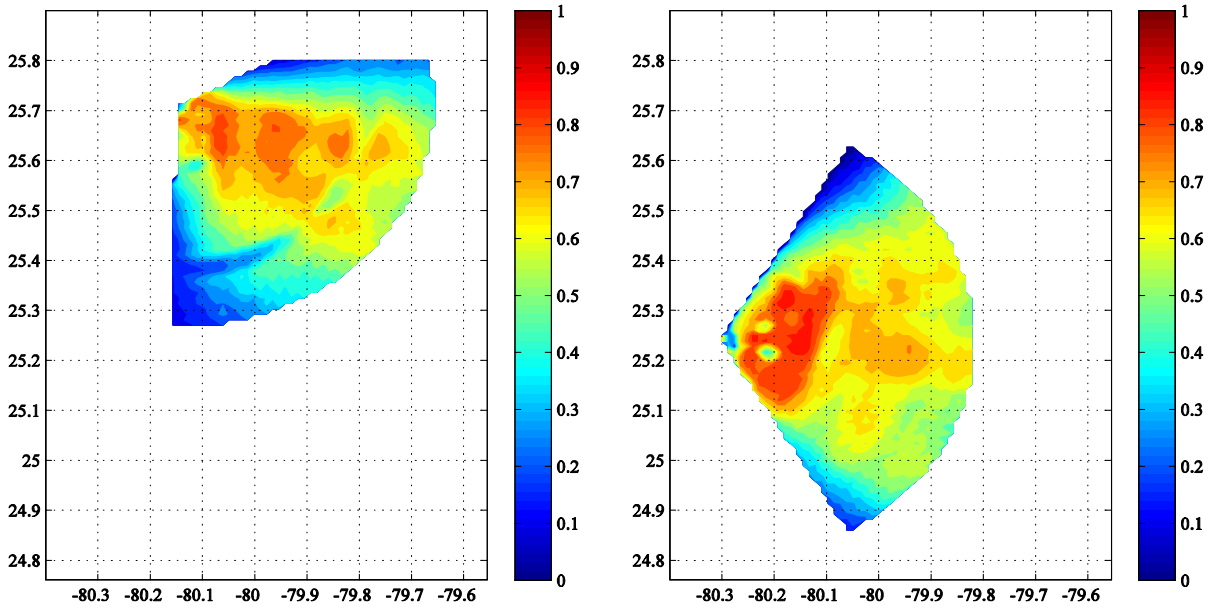

Figure 3.3-10: Fraction of radar data remaining after summing to 1 hr.

Relevant papers referenced in Section 3.3.3.1 indicate that RSMAS preferred calibration of the radar data using a best correlated location that was far separated from and in much deeper water than the in situ data used for calibration. Our preference was to use radar data co-located with the in situ data, even if it meant using radar data of lesser quality.

The in situ data cluster number 7 was used for the radar calibration. 13 radar cells within 2.5 km of the in situ location were selected for use in the calibration. These points were available for both radars and the quality control procedure was applied to both data sets for each hourly

time observation. The valid points were averaged and used to perform robust linear regression to find the best fit line in a scatter plot sense. A calibration ($slope \times radar\ value + offset$) was obtained for each radar and applied to all points. With the offset, in some rare cases radar points became negative and were reassigned to a value of zero. Plots of the robust least squares linear fits between the buoy and the radar are shown in Figure 3.3-11. The time period used for calibration is 05-Apr-2005 16:00:00 to 28-May-2005 08:00:00, which overlaps but is different from the time period for which the radar is compared to the models in Section 3.3.4.4 (01-Apr-2005 00:00:00 to 15-May-2005 23:00:00).

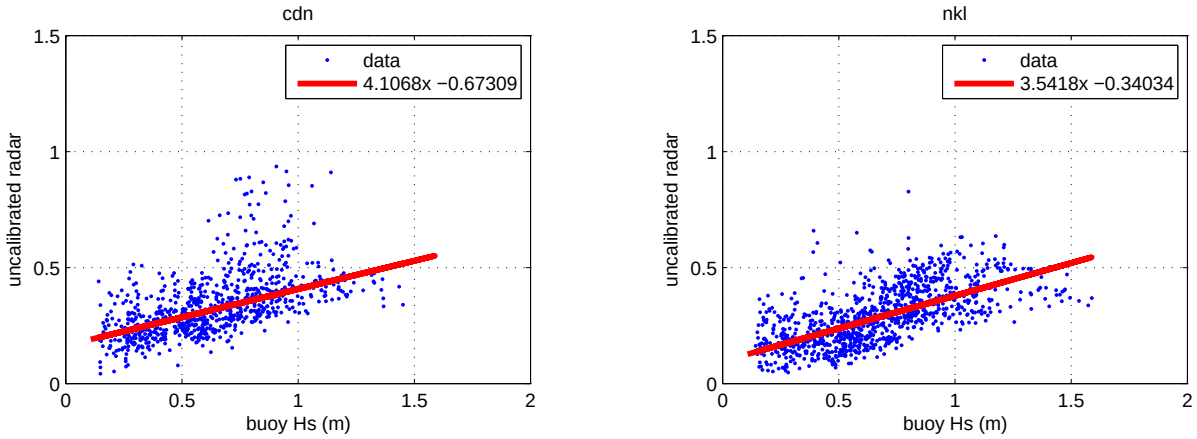

Figure 3.3-11: Plots of the robust least squares linear fits between the buoy and the radar radar at the CDN location (left) and NKL location (right).

The data required more processing after the temporal filtering and a sector averaging scheme was devised. Here we divided the radar swath areas into 6 sectors of 20° and subdivided these sectors into 5 equal areas where the full radar swath is 120° and spans radially 50 km with 1.2 km spacing between points. Hence there are 30 sectors for each of the radars with approximately 50 points in each sector.

The indices for the sectors are given by A-F for CDN and G-L for NKL with each having 5 areas, 1 through 5, increasing with distance from the center. These sectors are given in Figures 3.3-12 and 3.3-13.

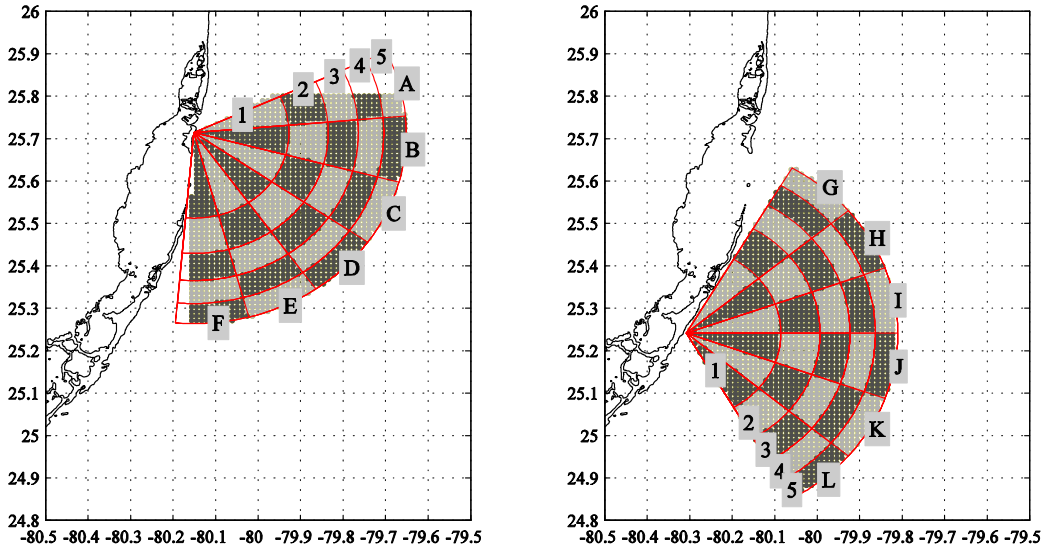

Figure 3.3-12: Radar sectors.

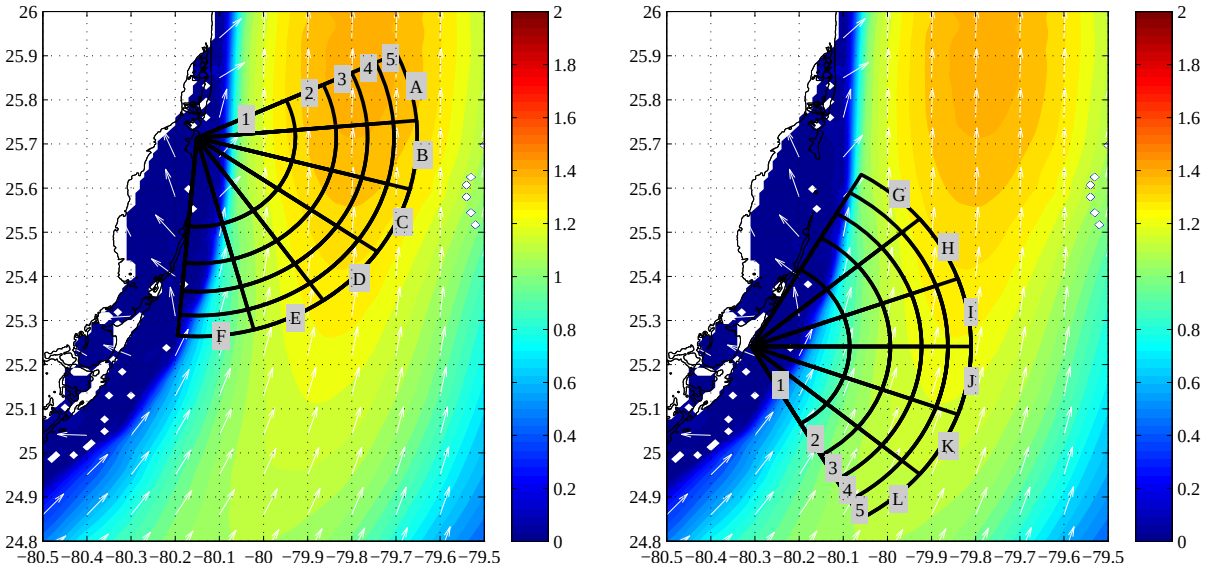

Figure 3.3-13: Radar sectors with example position of the Florida current (output from NCOM).

3.3.4.3 Model validation against radar

Refer to Gravois et al. (2012) for time series comparisons of the radar data against co-located model output. An example plot from Gravois et al. (2012) is included here as Figure 3.3-14.

In these plots, one can see that the sign of wave height bias "control" vs "no currents" alternate from deep to shallow water in sectors E through L. Specifically, for the event on April 18, the " no currents" case (green line) is higher than "with currents" (blue line "control case") in

shallow water. This reinforces what is observed in the in situ vs model comparisons. This behavior is not seen in sectors A-D, however.

Table 3.3-3 provides a summary of the error statistics from all of the plots in Gravois (2012), using the HF radar as ground truth. In several cases, the inclusion of currents results in a modest improvement to the correlation score and decrease in RMS error.

Figures 3.3-15 through 3.3-17 show the same statistics in graphical form. One worrisome feature is that the skill of the model is generally better nearer the center of the bore-sight of the radar, section in D, E, J, and K having relatively high correlation values. This suggests that the model validation skill may have more to do with the quality (or lack thereof) of the observational data than the skill of the model to reproduce spatial variability of the real ocean in the *azimuthal position relative to the radar origin*. However, on a positive note, the comparisons such as shown in Figure 3.3-14 are actually quite good.

The radar observations also help us to understand the overprediction of *in situ* wave heights for the swell events (April 3, 17), as larger waves were measured offshore by the radar for these events. This supports the argument that the overprediction is caused by errors in swell propagation direction, rather than by a general overprediction of the swell energy. This highlights the advantage that radar provides to analyze spatially non-homogeneous wave fields that are typical in the present case.

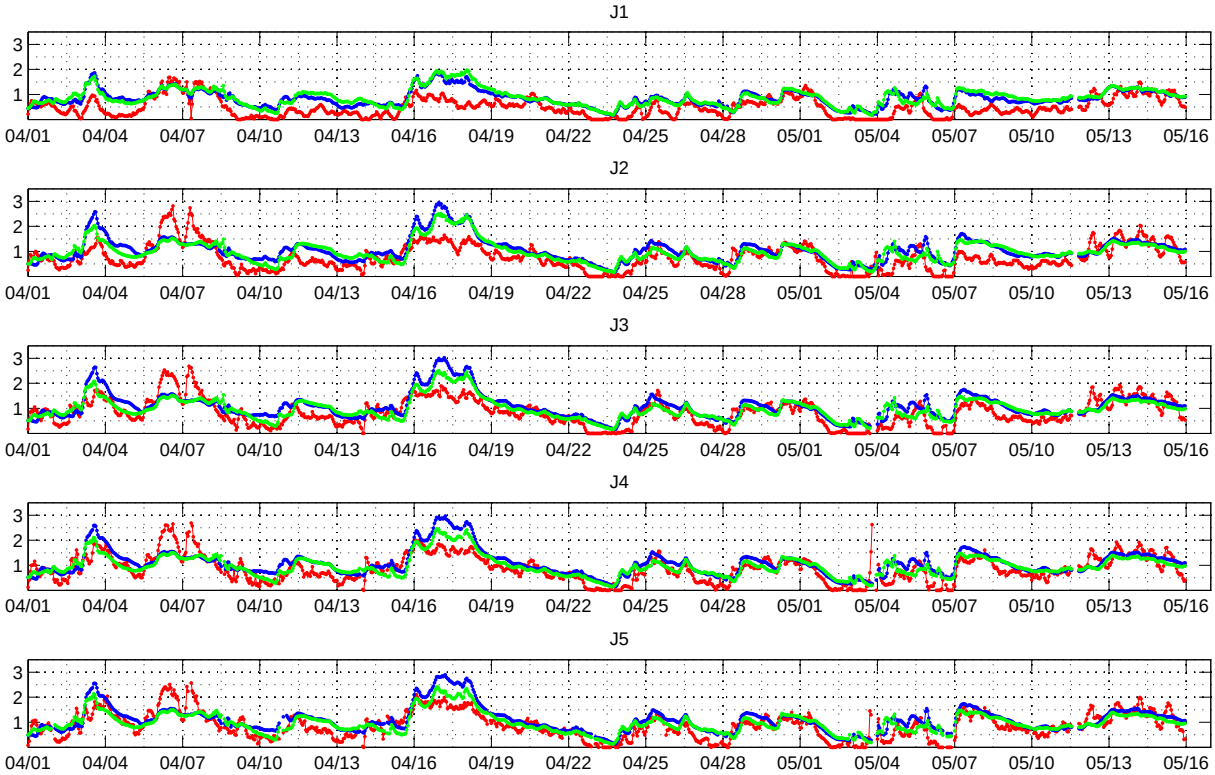

Figure 3.3-14: Example comparison of COAMPS (SWAN) fully coupled model output shown in blue vs. SWAN without currents (green) vs. calibrated radar (red). Significant wave height, in meters for the five bands within the J sector.

Table 3.3-3: Statistics of model vs. WERA data sectors. Relatively good values are shown in green and relatively poor values in red. Here, "nc" indicates the wave model simulations performed without surface currents as input. Skill is for significant wave height, in meters. Statistics are calculated for the period 01-Apr-2005 00:00:00 to 15-May-2005 23:00:00.

CDN															
	1			2			3			4			5		
	bias	rmse	r	bias	rmse	r	bias	rmse	r	bias	rmse	r	bias	rmse	r
A	0.56	0.78	0.53	0.20	0.85	0.29	0.05	0.76	0.33	0.03	0.71	0.31	0.06	0.66	0.31
A_nc	0.48	0.65	0.51	0.06	0.76	0.24	-0.06	0.71	0.31	-0.06	0.67	0.29	-0.01	0.62	0.29
B	0.62	0.77	0.67	0.49	0.66	0.72	0.31	0.58	0.63	0.37	0.57	0.65	0.37	0.55	0.67
B_nc	0.52	0.64	0.64	0.36	0.52	0.67	0.19	0.50	0.57	0.26	0.47	0.63	0.28	0.47	0.65
C	0.57	0.77	0.47	0.45	0.63	0.70	0.32	0.51	0.73	0.35	0.52	0.73	0.33	0.50	0.73
C_nc	0.49	0.65	0.49	0.31	0.48	0.69	0.19	0.42	0.69	0.22	0.42	0.71	0.20	0.42	0.71
D	0.56	0.78	0.28	0.35	0.55	0.77	0.17	0.49	0.79	0.21	0.47	0.81	0.20	0.45	0.81
D_nc	0.53	0.73	0.29	0.22	0.51	0.73	0.05	0.52	0.74	0.08	0.48	0.77	0.08	0.46	0.77
E	0.49	0.62	0.36	0.27	0.54	0.71	-0.03	0.53	0.81	0.07	0.48	0.80	0.07	0.46	0.79
E_nc	0.54	0.68	0.31	0.22	0.56	0.64	-0.10	0.63	0.71	-0.02	0.55	0.72	-0.03	0.53	0.71
F	0.34	0.44	0.38	0.07	0.48	0.51	-0.25	0.62	0.55	-0.12	0.54	0.63	-0.08	0.46	0.70
F_nc	0.45	0.54	0.34	0.14	0.51	0.44	-0.21	0.64	0.45	-0.10	0.56	0.56	-0.08	0.49	0.63
NKL															
G	0.43	0.50	0.26	0.14	0.34	0.52	0.04	0.43	0.61	0.02	0.47	0.58	-0.01	0.47	0.67
G_nc	0.49	0.57	0.19	0.21	0.40	0.45	0.05	0.45	0.55	-0.03	0.51	0.46	-0.10	0.52	0.58
H	0.38	0.44	0.65	0.29	0.45	0.66	0.23	0.45	0.72	0.20	0.44	0.74	0.19	0.43	0.75
H_nc	0.45	0.51	0.61	0.29	0.46	0.60	0.15	0.41	0.66	0.09	0.39	0.70	0.08	0.39	0.71
I	0.37	0.46	0.64	0.34	0.51	0.65	0.30	0.49	0.68	0.27	0.48	0.70	0.27	0.46	0.72
I_nc	0.42	0.51	0.58	0.28	0.47	0.61	0.20	0.42	0.66	0.16	0.39	0.68	0.15	0.38	0.70
J	0.35	0.45	0.63	0.28	0.49	0.63	0.23	0.45	0.70	0.20	0.43	0.71	0.20	0.41	0.75
J_nc	0.38	0.49	0.59	0.22	0.45	0.63	0.13	0.39	0.70	0.09	0.37	0.72	0.08	0.35	0.75
K	0.29	0.45	0.60	0.22	0.48	0.57	0.16	0.43	0.64	0.11	0.40	0.68	0.09	0.40	0.69
K_nc	0.32	0.48	0.56	0.16	0.45	0.58	0.07	0.38	0.66	0.01	0.35	0.69	-0.01	0.35	0.71
L	0.28	0.46	0.57	0.16	0.52	0.46	0.04	0.50	0.47	-0.03	0.48	0.53	-0.05	0.46	0.56
L_nc	0.31	0.49	0.52	0.13	0.50	0.46	-0.02	0.48	0.49	-0.11	0.47	0.55	-0.14	0.45	0.58

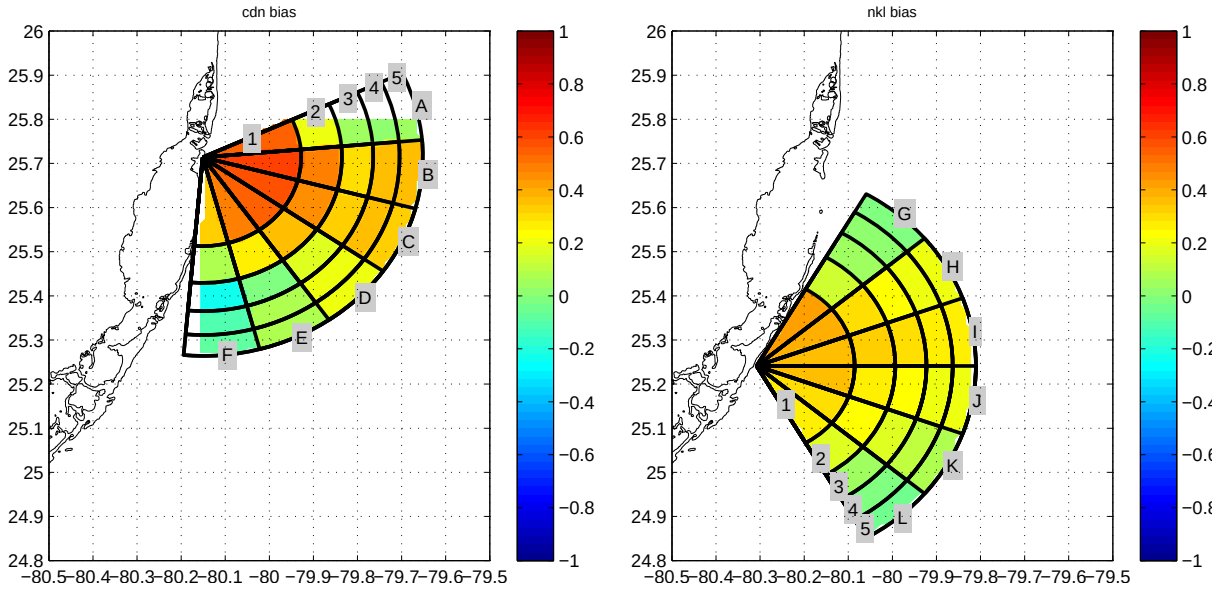

Figure 3.3-15: Bias of significant wave height, in meters.

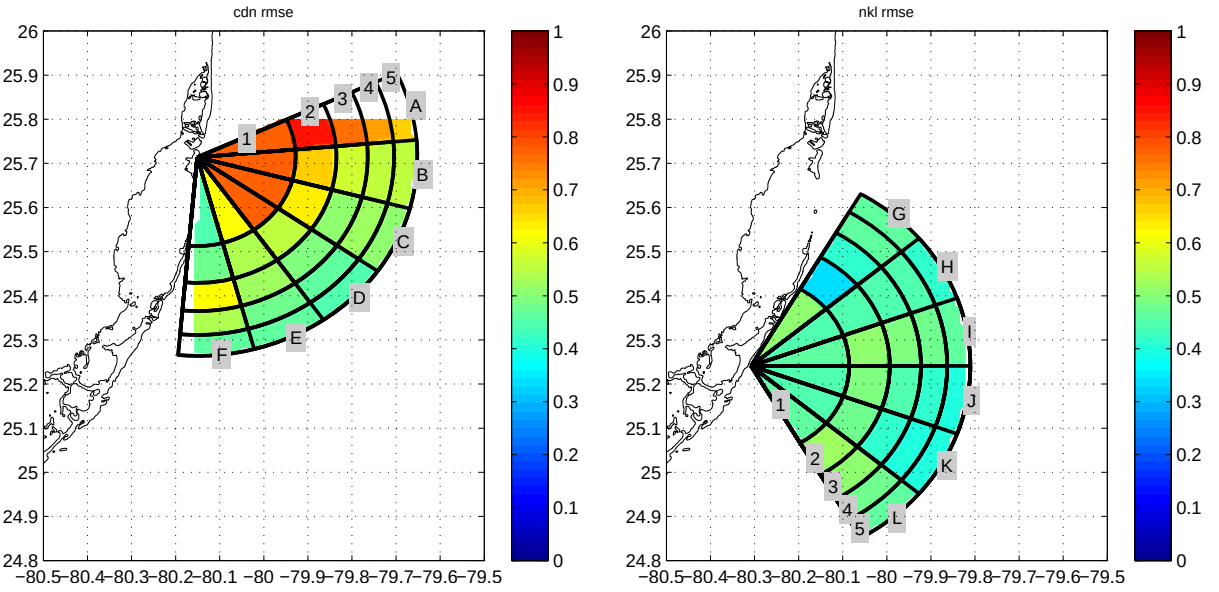

Figure 3.3-16: RMS error of significant wave height, in meters.

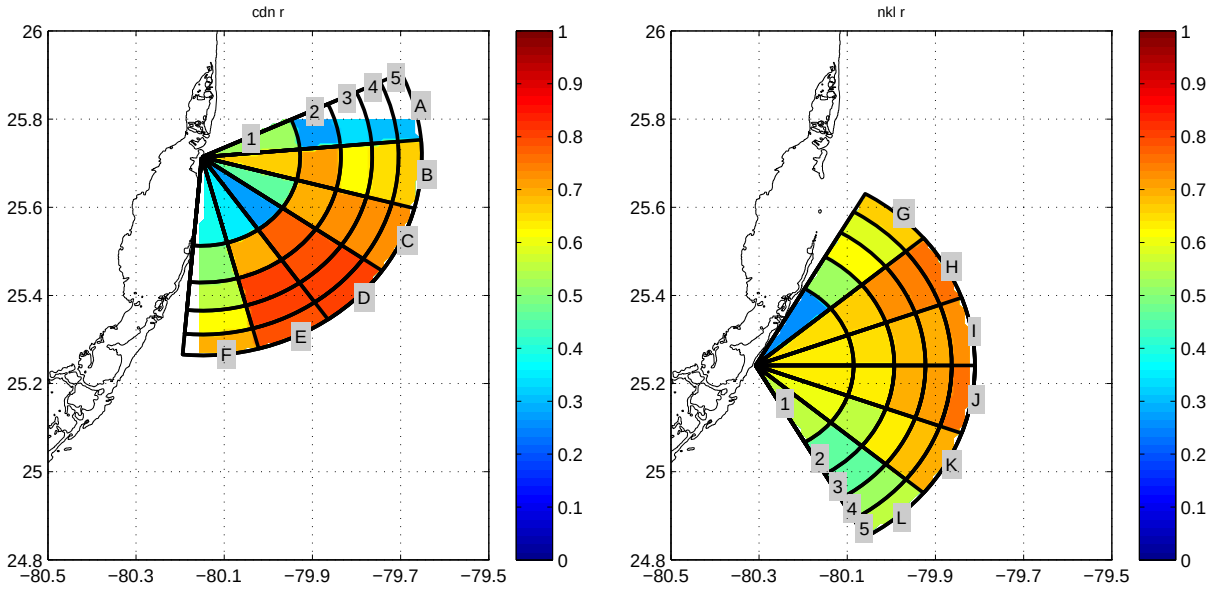

Figure 3.3-17: r statistic (correlation) for significant wave height.

3.3.4.4 Ocean Current Comparisons

Radar data were downloaded from the RSMAS website http://iwave.rmas.miami.edu/wera/efs/data for the period March 10 through May 25, 2005 1200 UTC, a total of 1992 hours. The data include position (longitude, latitude), current direction (in degrees) and hourly averaged current speed (cm/s), and the number of samples in the average. The areal coverage varies significantly with time. Figure 3.3-18 provides two examples. In the left panel is an example of a data sparse hourly average with data limited to the nearshore area near the southernmost radar site. The right panel has an example of excellent data coverage throughout the range of the radars. The non-uniform coverage and frequency of missing data at a given location made the comparison between WERA observations and COAMPS more difficult, in particular reducing the ability to investigate synoptic events over several days.

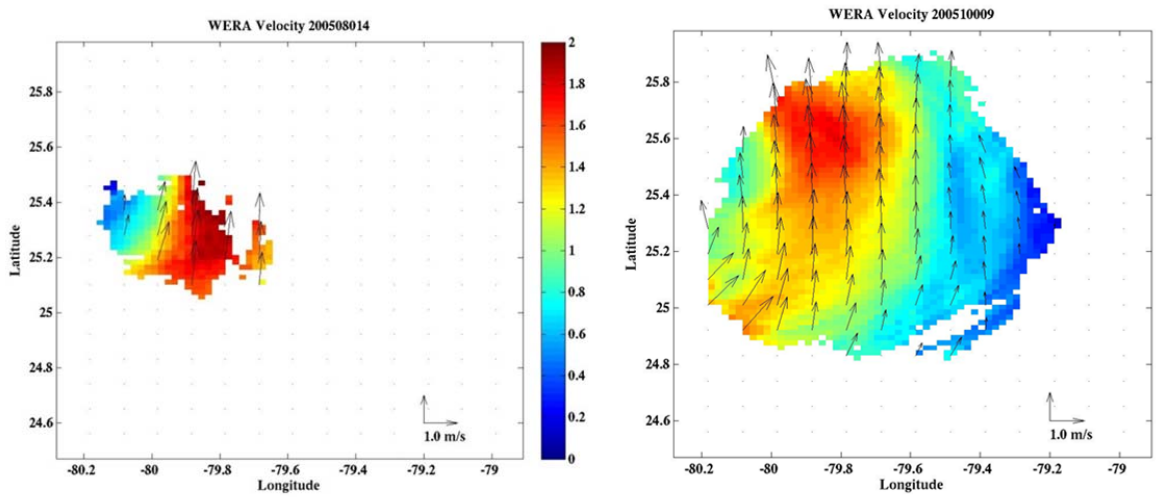

Figure 3.3-18: Surface current plots from WERA radar at March 21 (Julian day 80) at 1400 UTC (left) and at April 10 (Julian day 100) at 0900 UTC. The plots demonstrate the large variations in usable data coverage. Vectors show the current velocity and the color scale of the current speed.

There is a tendency to have better coverage from late night to early morning. However, Figure 3.3-19 shows two other examples of WERA observations where excellent coverage was obtained in the afternoon (local time is UTC - 5 hours) and very sparse coverage in the morning (right panel). It is also evident that the magnitude of the current does not impact the area coverage. The best coverage is nearest the optimal area where the radar beams intersect, around 90^{o}. For angles less than 30^{o} and larger than 120^{o} the data are discarded. Figure 3.3-20 shows the average sample size of all radar observations. The distribution of observations with time is shown in Figure 3.3-21. With the exception of days 97 and 98, where the observations were less than 50% of the average, the number of observations gathered by the radar was close to an average of 20,000 samples per day. The distribution of data, however, varied throughout the day. Figure 3.3-22 demonstrates that the data coverage was best late at night and early morning, with declining coverage until 8 pm local time. Figure 3.3-23 is similar to Figure 3.3-22, but shows the fraction of the time from Julian day 69 to 151 when useable observations were available.

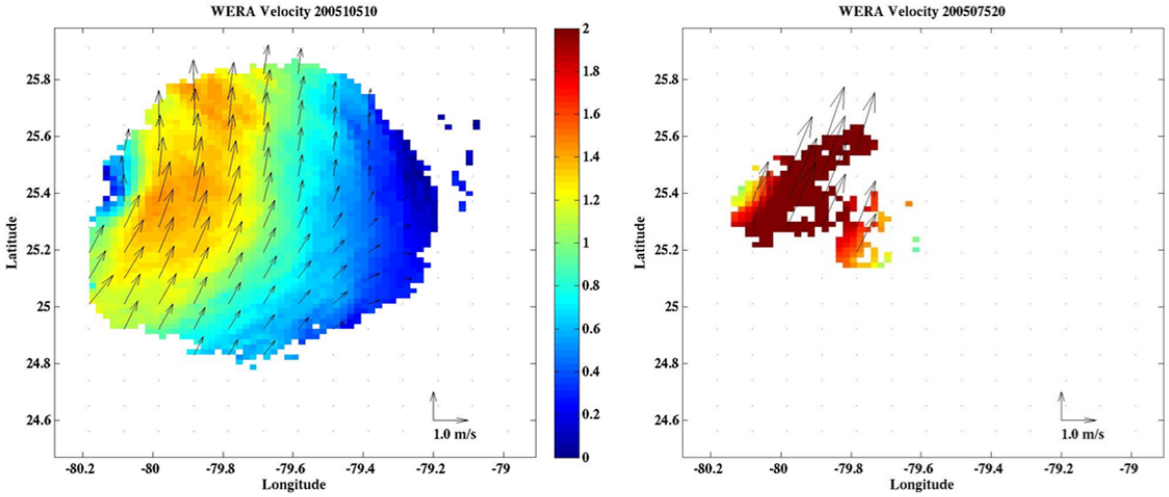

Figure 3.3-19: Surface current plots from WERA radar at April 15 (Julian day 105) at 2000 UTC (left) and at March 16 (Julian day 75) at 0900 UTC.

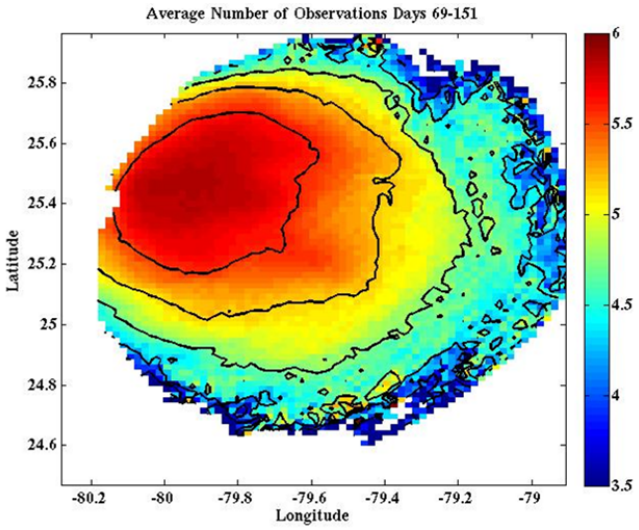

Figure 3.3-20: Average sample size from March 10 through May 25 (Julian day 69 through Julian day 151). The range is three to six samples. If less than three samples are available at a location during a sampling interval, the data are marked as missing.

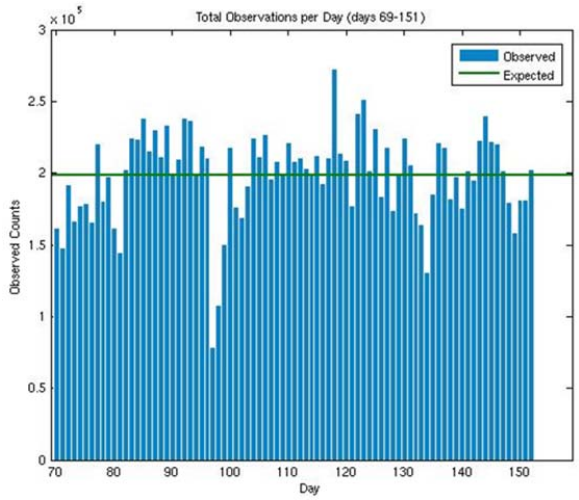

Figure 3.3-21: Total number of observations per day during Julian day 69-151 (March 10 – May 31, 2005). The green line shows the average number of daily observations.

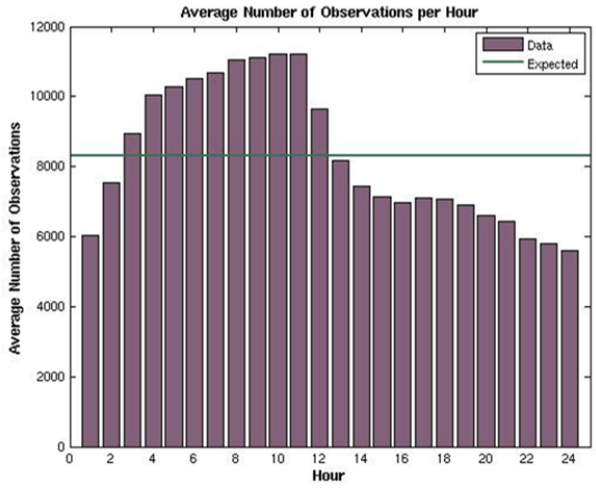

Figure 3.3-22: Average number of hourly observations during a 24 hour period. The average was computed over Julian day 69 -151. The hours are in UTC. Local time is UTC – 5.

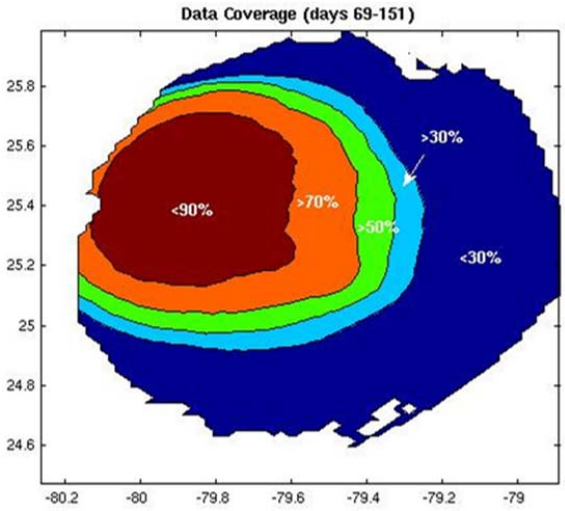

Figure 3.3-23: Data coverage in percent of time during the 83 days analyzed.

3.3.4.5 Comparisons to WERA radar currents

COAMPS (NCOM component) and WERA data were compared for a 77 day period from March 10-May 25, 2005, a time frame when both observations and model output were available. In addition to the hourly data, time series of 48 hour running mean were computed to compare the surface currents on a synoptic time scale and to filter out the diurnal and semi-diurnal tide. Twelve different areas were selected (Fig. 3.3-24) where time series of surface currents were made from model and radar observations of surface currents. Figure 3.3-25 shows the filtered time series of total current speed along latitude section A (25.4°N to 25.8°N) for four longitudes. The WERA currents were significantly stronger in section A1 near the coast. There was fairly good agreement in magnitude in section A3 near the core of the Florida Current and currents weaker than COAMPS were seen in section A4, the shear zone towards the open ocean.

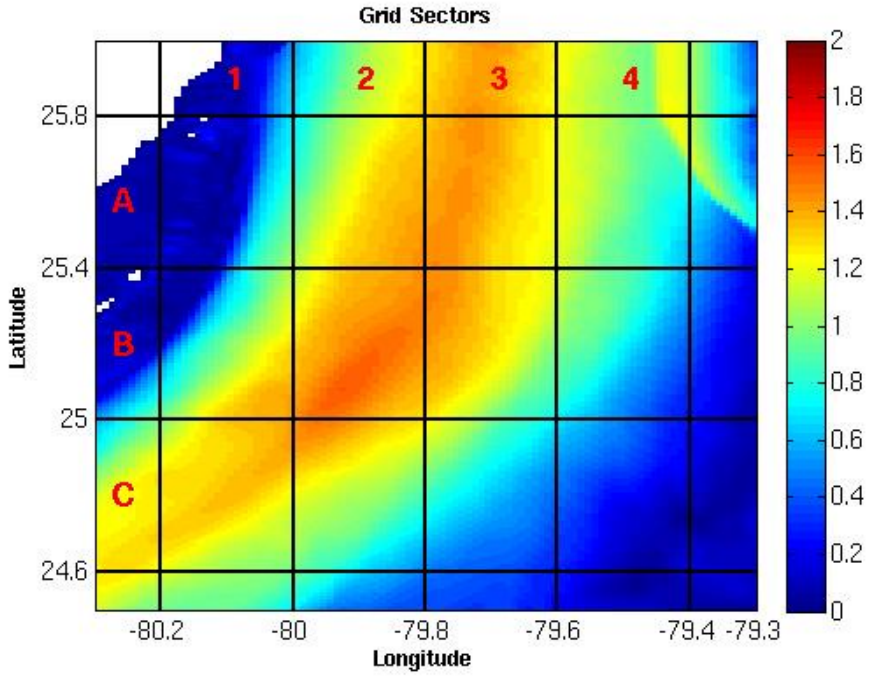

Figure 3.3-24: Map showing the 12 areas where average times series from radar and model where computed. The color shows the average current speed from COAMPS during the entire analysis period.

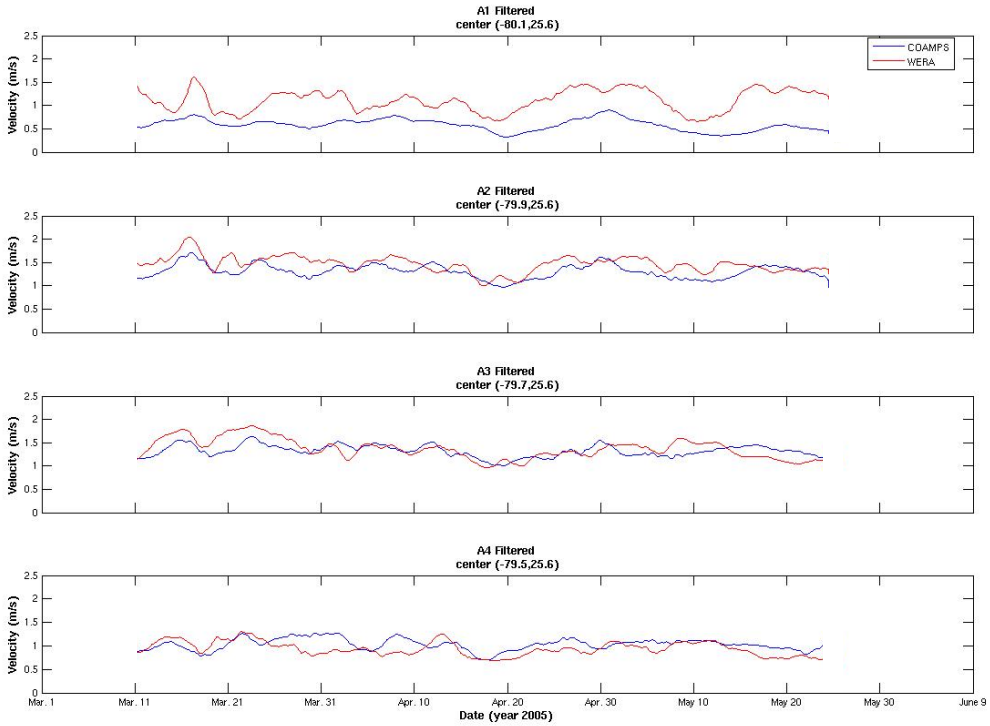

Figure 3.3-25: Time series of current speed averaged over each of the four sectors A1, A2, A3 and A4 are shown (top to bottom). The red line is WERA radar observations and the blue line is COAMPS. A 48-hour running mean filter was applied to the results.

Along latitude section B (25.0°N to 25.4°N) the same tendency is observed, with the best agreement in longitude band 3 (79.8°W to 79.6°W) (Figure 3.3-26). Latitude section C is shown in Figure 3.3-27, with the best agreement in band 4. Correlations between each velocity component and the total speed are provided in Table 3.3-3 for the 48-hour filtered data and for the hourly data in Table 3.3-4.

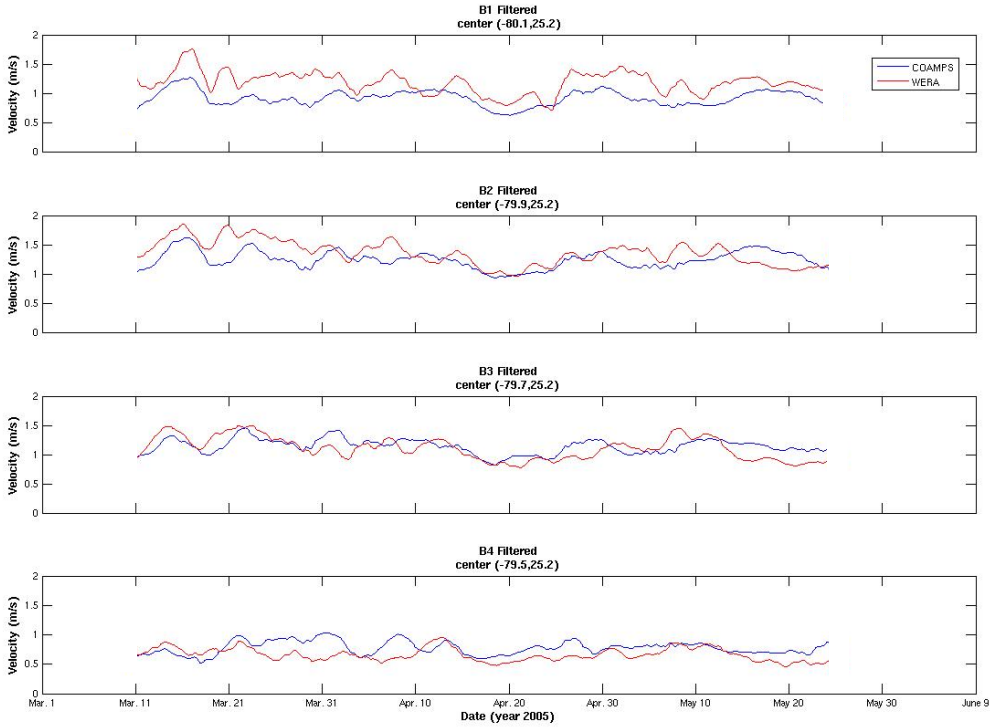

Figure 3.3-26: As Figure 3-25, but each of the four sectors B1, B2, B3 and B4 are shown.

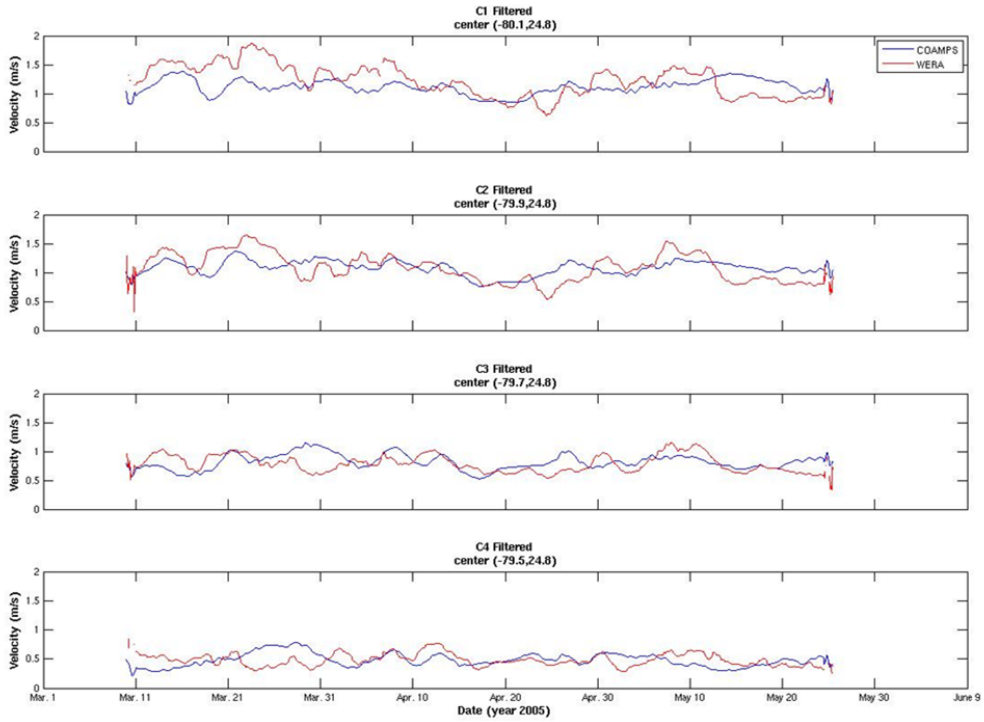

Figure 3.3-27: As Figure 3.3-26, but each of the four sectors C1, C2, C3 and C4 are shown.

Table 3.3-4: Correlation coefficient for COAMPS and WERA time series for each sector using the area average for each sector and 48-hour running mean filtered data.

		1	2	3	4
A	u	0.29	0.49	0.40	0.42
	v	0.47	0.56	0.53	0.34
	spd	0.43	0.57	0.55	0.38
B	u	0.55	0.32	0.28	0.26
	v	0.60	0.42	0.55	0.19
	spd	0.58	0.44	0.56	0.21
C	u	0.08	0.25	0.27	0.28
	v	0.26	0.51	0.22	0.03
	spd	0.26	0.51	0.16	-.17

Table 3.3-5: Correlation coefficient for COAMPS and WERA time series for each sector using the area average for each sector and 1-hour unfiltered data.

		1	2	3	4
A	u	0.23	0.43	0.39	0.34
	v	0.46	0.50	0.48	0.40
	spd	0.41	0.50	0.49	0.41
B	u	0.51	0.36	0.32	0.31
	v	0.52	0.40	0.48	0.34
	spd	0.52	0.43	0.48	0.33
C	u	0.10	0.23	0.27	0.27
	v	0.31	0.45	0.30	0.17
	spd	0.27	0.43	0.25	0.04

3.3.4.6 Impact of Waves on Currents

To better understand the impact of waves on the surface ocean currents, a qualitative examination was performed using a coupled NCOM-SWAN scheme and a NCOM-only run for two wind regimes: 1) northerly winds that opposed the Florida Current (FC) on April 3, 2005 and 2) southerly winds that flowed with the FC on April 8, 2005. Figure 3.3-28 depicts the 2 km COAMPS surface winds for these two periods. Figure 3.3-29 (northerly wind case) shows a widening of the FC near 25 °N (left) with weaker currents near the core without waves (middle panel). The right panel shows the difference in current speed. Twenty-four hour averages for April 3 are shown. Moderate winds from the south on April 8 were used for the model comparisons shown in Figure 3.3-30. In this case the FC in the coupled run was narrower, with a more intense core (left) than in the uncoupled run (middle). Overall, the inclusion of waves was found to modulate the FC with differences in the surface currents up to 0.5 m/s in daily averages. In the coastal region, where buoy observations were available, differences were small.

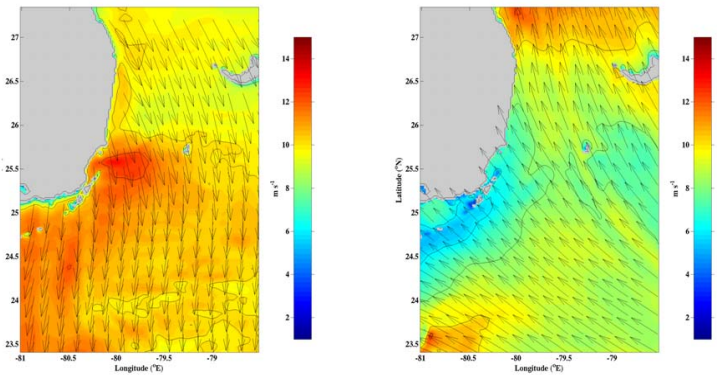

Figure 3.3-28: COAMPS 10 m winds (2 km resolution) for a) northerly wind case on April 3, 2005 1500 GMT and b) southerly wind case on April 8, 2005 1500 GMT. Color scale shows the magnitude of the wind speed.

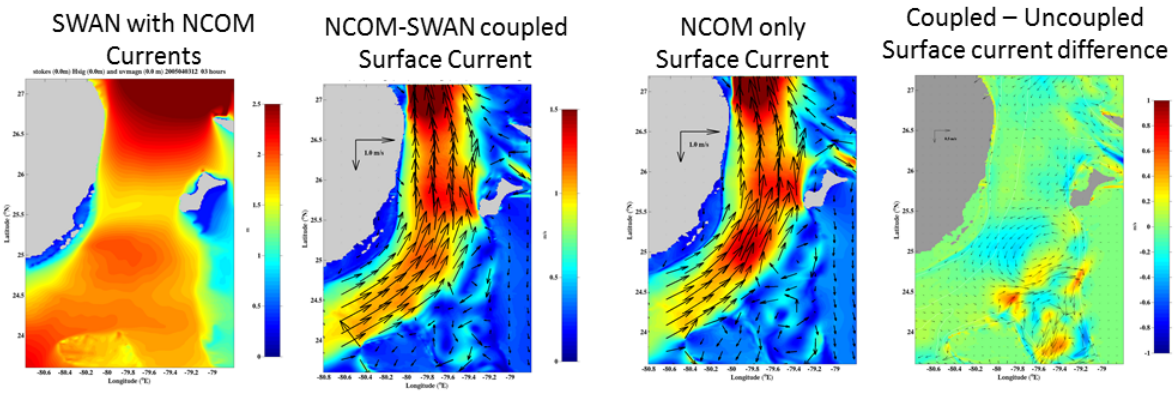

Figure 3.3-29: Surface current from NCOM_SWAN coupled run for northerly wind case on April 3, 2005 (left); SWAN significant wave height (including NCOM currents), NCOM only surface current for same date (middle); and a difference plot between the coupled and uncoupled NCOM run (right).

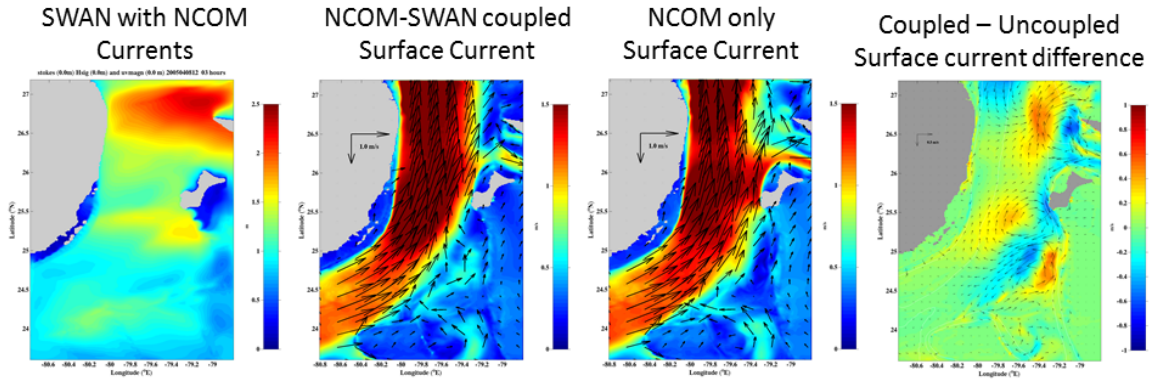

Figure 3.3-30: Same as Figure 3.3-28 except for southerly wind case on April 8, 2005 at 1500 GMT.

3.4 Test Case 4: Adriatic Sea (ACE 2003 and DART 2006)

3.4.1 Purpose

The validation period studied encompasses a portion of the Adriatic Circulation Experiment (ACE) in February 2003 and the DART (Dynamics of the Adriatic in Real-Time) field experiment that was performed in February-March 2006. Similar to the the Atmosphere/Ocean VTR, the February 2003 COAMPS runs were compared to ACE data from the winter of 2003 (Pullen et al., 2007). ACE primarily focused on downslope windstorm events called “bora” that occur during the late fall and winter in the topographic mountain gaps of the Dinaric Alps of Croatia. Bora winds traverse the Adriatic Sea in the form of mesoscale jet flows, making this region amenable to air/sea/wave interaction studies at the mesoscale level.

The DART experiment was a multi-disciplinary scientific field program of near-real-time, in situ measurement and reporting. A main objective of the DART experiment, staged in the coastal area of the western central Adriatic, is to study mesoscale instabilities arising in the Western Adriatic Current (WAC) near the Gargano Cape and in the Central Adriatic Sea, an area with intense navigation and fishing activity. The time-scales of eddies, fronts and filaments near the WAC are typically on the order of a few hours to a day. Non-linear interactions of the instabilities with internal waves and tides make operational forecasting in the area complex and challenging. The DART06 data have been used for adaptive sampling, forecast validation, and demonstration of real-time operational capabilities. The DART06 study has enhanced predictive capabilities of marginal seas with topographic controls through the production of a comprehensive dataset of atmospheric and oceanographic characteristics of the Adriatic Sea.

3.4.2 Test Area and Observations

Meteorological conditions above the Adriatic are dominated by three weather types: unperturbed weather, sirocco-related weather, or bora-related weather. The northeasterly bora winds occur more frequently in winter and in the northern Adriatic and bring cold and dry air to the Adriatic. See Pullen et al. (2007) for background information about the meteorological and oceanographic characteristics of the test area.

Ocean current data for February 2003 were obtained from Acoustic Doppler Current Profilers (ADCPs). Fourteen trawl-resistant bottom-mounted ADCPs (Perkins et al., 2000) were deployed from September 2002 to May 2003 by NRL during the ACE in conjunction with the NATO Undersea Research Centre (NURC) as a Joint Research Project (JRP) (Book et al. 2007). The specific moorings used in this validation were VR1, VR2, VR4, VR5, VR6, KB1, CP2, and CP3 (Figure 3.4-1).

The DART06 observations consisted of surface drifting floats, satellite remote sensing products, and several new Shallow-water Environmental Profiler in Trawl resistant Real-time (SEPTR) configuration moorings that held some ADCPs and two wave buoys (Figure 3.4-1).

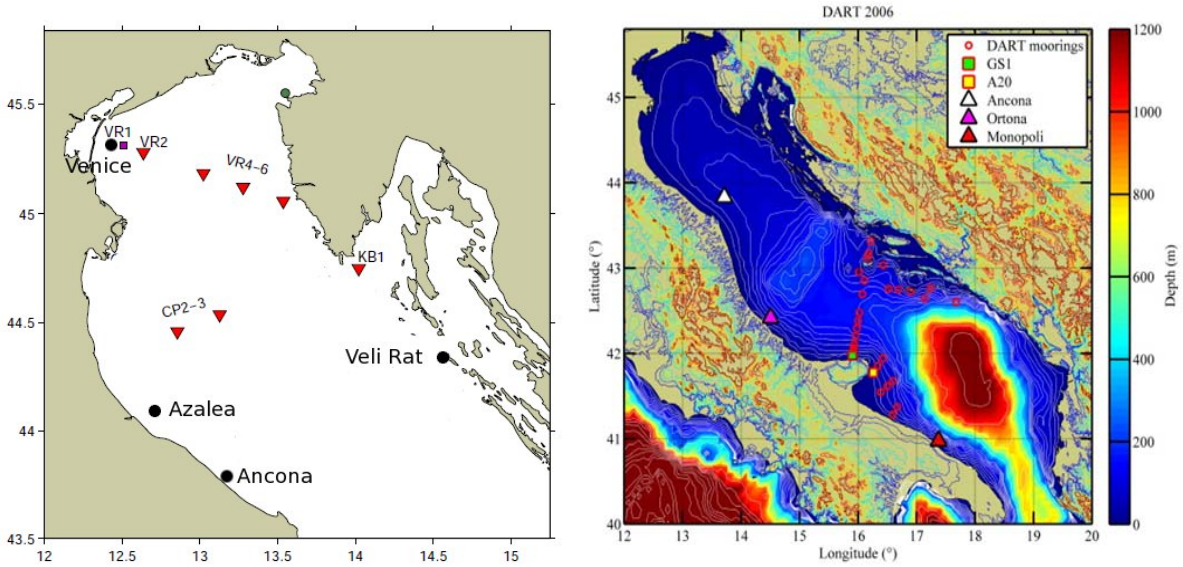

Figure 3.4-1: February 2003 ACE ADCP moorings (left). Red triangles are ADCP/tide moorings. The purple square is the JRP ADCP mooring and the wave gauge at Venice. The February/March 2006 DART deployments are shown in the figure at right, with the Ancona and Ortona (Pescara) wave buoys designated by white and purple triangles, respectively. Red circles denote ADCP/SEPTR moorings that traverse the Adriatic and run along the coastal areas of the southern Adriatic Sea.

3.4.3 Model Setup

An initial coupled air/sea/wave COAMPS run was completed to produce 15 minute, 3 km resolution wind forcing for a higher resolution Adriatic Sea NCOM run, saving on computation time and resources (Figure 3.4-2). Also, WW3 boundary conditions were produced for the DART 2006 from the initial lower-resolution simulation. The NCOM initial conditions for the high resolution DART 2006 were based on previous DART/NCOM runs to ensure a correct Adriatic Sea circulation.

Ocean to wave model coupling in COAMPS is accomplished by passing NCOM ocean currents and water levels to SWAN for wave field computation. The wave source terms in SWAN take into account the NCOM currents and water levels in calculating the SWH, peak period, and wave direction. For February 2003 (ACE) and the February-March 2006 (DART), both ocean/wave model uncoupled and coupled simulations were completed with 15 minute wind forcing from the 3 km atmospheric nest setup and preliminary run as shown in Figure 3.4-3. Included in the coupled simulations were both a one-way (o2w=t, w2o=f) and two-way (o2w=t, w2o=t) coupled simulation (o = ocean, w = wave, t = true, f = false).

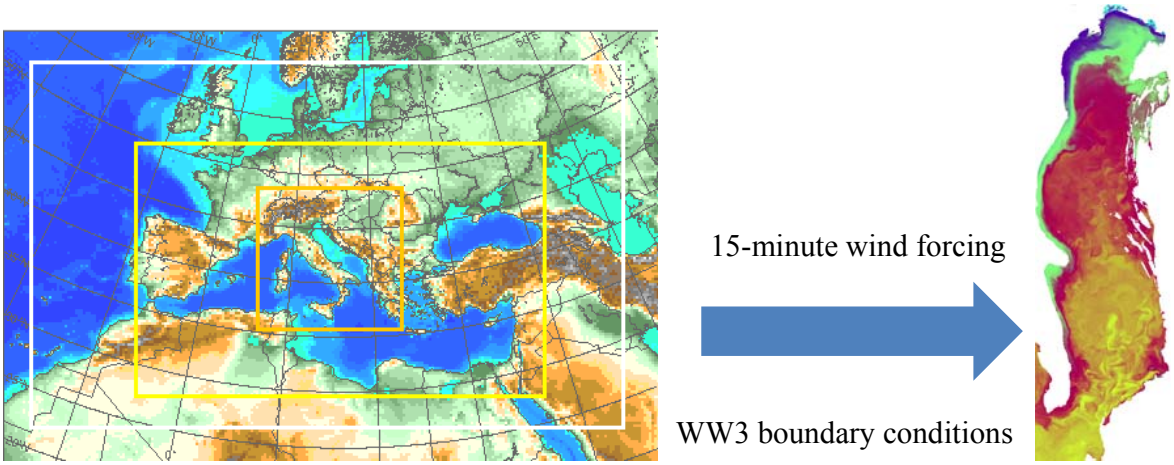

Figure 3.4-2: Atmospheric (left) and ocean/wave grid setup (right) for the Adriatic Sea. An initial COAMPS 3 km grid was setup for wind forcing, and initial and boundary conditions came from WW3 for a subsequent, higher resolution NCOM run.

3.4.4 Results

3.4.4.1 2003 ACE Ocean Model Validation

In order to test the wave to ocean model coupling in COAMPS, several experiments were performed for the February 2003 ACE period. Three two-way (o2w=t, w2o=f) ocean/wave coupled simulations and an uncoupled ocean-only simulation were performed:

1) fully-coupled ocean/wave with NCODA ocean assimilation,
2) fully-coupled ocean/wave without NCODA ocean assimilation,
3) fully-coupled ocean/wave with NCODA ocean assimilation without the wave radiation stress gradient passed to NCOM, and
4) uncoupled, without waves.

The wave radiation stress is the flux of momentum which is carried by ocean waves. As waves break, that momentum is transferred to the water column, forcing nearshore currents. Forcing due to these radiation stress gradients can be greater than forcing due to wind or other wave nonlinearities, especially near the coast. Since several of the ADCPs for ACE are located near the coast, all the ADCPs were evaluated with and without the wave radiation stress forcing in the model. This was completed to determine if the forcing was substantial enough to affect the near surface currents, especially the mean directional error (MDE) near the surface. Table 3.4-1 is a summary of statistics for both the MDE and complex correlation coefficient (CCC) (to 50 m) for each of the ADCPs from ACE for each of the model configurations above.

ADCP comparisons to model output were evaluated using techniques described in Section 3.1.4.5.

The statistical analysis of each ADCP indicate that coupling with the wave radiation stress gradients improved the MDE at most of the ADCP sites (Table 3.4-1), even in the simulation without NCODA ocean assimilation. In the fully-coupled simulation with NCODA and the wave radiation stress gradients, none of the ADCPs are shown to have the worst MDE statistical comparisons. The ADCPs with the largest MDE values (greater than 10 degrees), VR4 and KB1, were difficult to compare to NCOM modeled currents for several reasons. The KB1 ADCP is located very near the coast and currents at this location are affected not only by complex bathymetry in this area, but also by the core of the bora jet winds that frequently develop near or over KB1. The larger MDE errors at VR4 are due to the location of the double-gyre that develops from the wind stress forcing at the ocean surface in the northern Adriatic Sea during wintertime bora events. A small shift in the location of the double-gyre surface current pattern in NCOM (when compared to observations) increased the MDE errors at VR4, VR5, and VR6 substantially, making the statistical analysis difficult. It appears that for this particular time period that ocean/wave coupling improves the MDE when ocean/wave coupling is included in the simulation.

Table 3.4-1: Summary of the mean directional errors (degrees) and complex correlation coefficients (to 50 m) for each of the ADCPs for the Adriatic Sea from 2003.

Mean Directional Error	VR1	VR2	VR4	VR5	VR6	CP2	CP3	KB1
Coupled w/wave (NAVDAS and NCODA)	2.12	1.30	15.17	7.15	4.26	2.89	0.40	12.13
Coupled w/wave (NAVDAS, no NCODA)	1.78	1.74	15.65	7.32	4.34	2.98	0.78	10.53
Coupled w/wave (no wradsg exchange)	2.99	1.33	16.58	7.98	3.63	2.71	1.22	12.56
Uncoupled (ocean only)	1.75	0.54	16.30	7.86	4.76	1.69	1.23	11.14

Complex Correlation Coefficient (CCC)	VR1	VR2	VR4	VR5	VR6	CP2	CP3	KB1
Coupled w/wave (NAVDAS and NCODA)	0.47	0.59	0.53	0.60	0.50	0.49	0.68	0.40
Coupled w/wave (NAVDAS, no NCODA)	0.47	0.60	0.53	0.60	0.50	0.48	0.66	0.40
Coupled w/wave (no wradsg exchange)	0.47	0.60	0.55	0.61	0.51	0.49	0.67	0.39
Uncoupled (ocean only)	0.48	0.63	0.54	0.60	0.50	0.48	0.68	0.40

The CCC calculations are also shown in Table 3.4-1 for each of the ADCPs. Like the MDE, the CCC was depth averaged. Little difference is noted in the CCC for this particular period for all the simulations, including the uncoupled run. Overall, some improvements were noted at several of the ADCP sites when coupling was performed; however, it is still difficult to determine whether coupling between NCOM and SWAN, and vice versa, is beneficial for this particular region, and ultimately we were unable to positively determine the overall effects of ocean currents passed to the SWAN wave field during this time period due to a lack of observations. However, more wave observations were collected during the DART ’06 field campaign and additional analyses of wave to ocean model coupling is presented in Section 3.1.4.2.

3.4.4.2 Coupled and Uncoupled (Ocean/Wave) Comparisons with DART data

Comparisons of SWH in both wave buoy (Ancona and Pescara) and satellite altimeter data for both the uncoupled and coupled COAMPS simulations did not show significant statistical differences. At Ancona (Table 3.4-2), the two-way coupled simulation indicated a slightly lower mean bias (MB) and root mean square error (RMSE) for SWH when compared to the uncoupled and one-way coupled simulations. A time series (Figure 3.4-3) of SWH for the uncoupled (green) and two-way coupled (blue) simulations shows a few instances where the coupled model performed better (circles) when compared to observations (red), which helped to improve the results at Ancona. At Pescara (Table 3.4-3), the statistics show a slight improvement in the correlation coefficient in the coupled COAMPS simulations. Although the overall differences in CC, MB, and RMSE are small, there are clearly events where the two-way coupled run performs better (circled in Fig. 1-3). These improvements in individual events can be important, as they may hypothetically occur on days when naval operations take place in the area.

An improvement in the SWH in the coupled model was apparent during the period of February 15-17, 2006 (Figure 3.4-3). This period was dominated by brisk southerly wind flow ahead of the next extratropical low pressure system entering Europe. Figure 3.4-4 shows the mean SWH difference and mean NCOM-only and coupled model surface currents for the period 15 February 1200 UTC and 16 February 0000 UTC. Model output available at 15 min intervals was averaged over the 12 hour period to determine the model means. The coupled model surface currents in the domain were primarily stronger during this period than in the uncoupled model. At the Ancona Mast site (star symbol), the mean currents were slightly stronger during this period. Since the mean wind was southerly, the effective wind speed was lessened which likely contributed to slightly lower SWHs in the coupled model than in the uncoupled model. The southerly winds were anomalous, i.e., the typical wind direction for February is north to northeast.

Table 3.4-2: Significant wave height statistics for coupled and uncoupled runs at Ancona for February 5-24, 2006.

Ancona (5-24 Feb 2006)	Mean (m)	MB (m)	CC	Std Dev.	RMSE (m)
Observed	1.31			0.73	
Uncoupled (o2w=f, w2o=f)	1.13	-0.17	0.90	0.60	0.37
One-way coupled (o2w=t, w2o=f)	1.17	-0.14	0.90	0.54	0.37
Two-way coupled (o2w=t, w2o=t)	1.19	-0.12	0.91	0.56	0.34

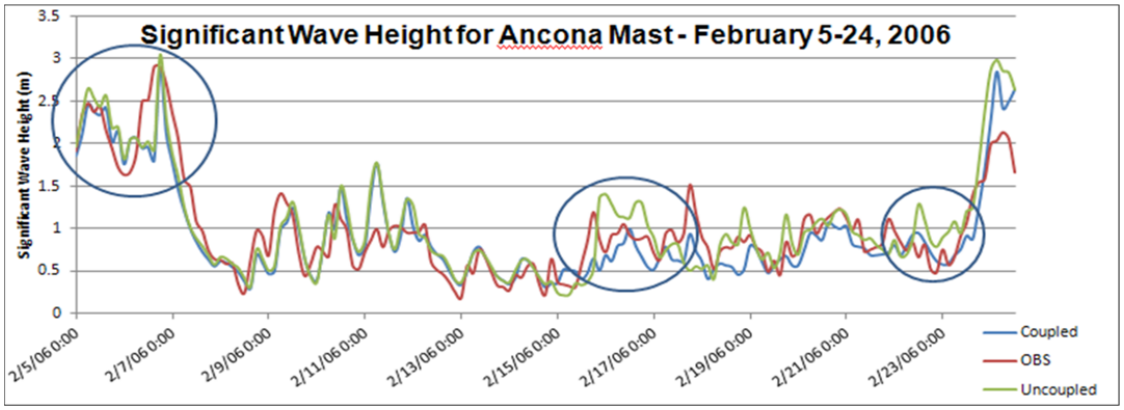

Figure 3.4-3: Bora events are captured well in the model (beginning of February). The coupled model (o2w=t, blue) showed some improvement at several distinct times during the simulation.

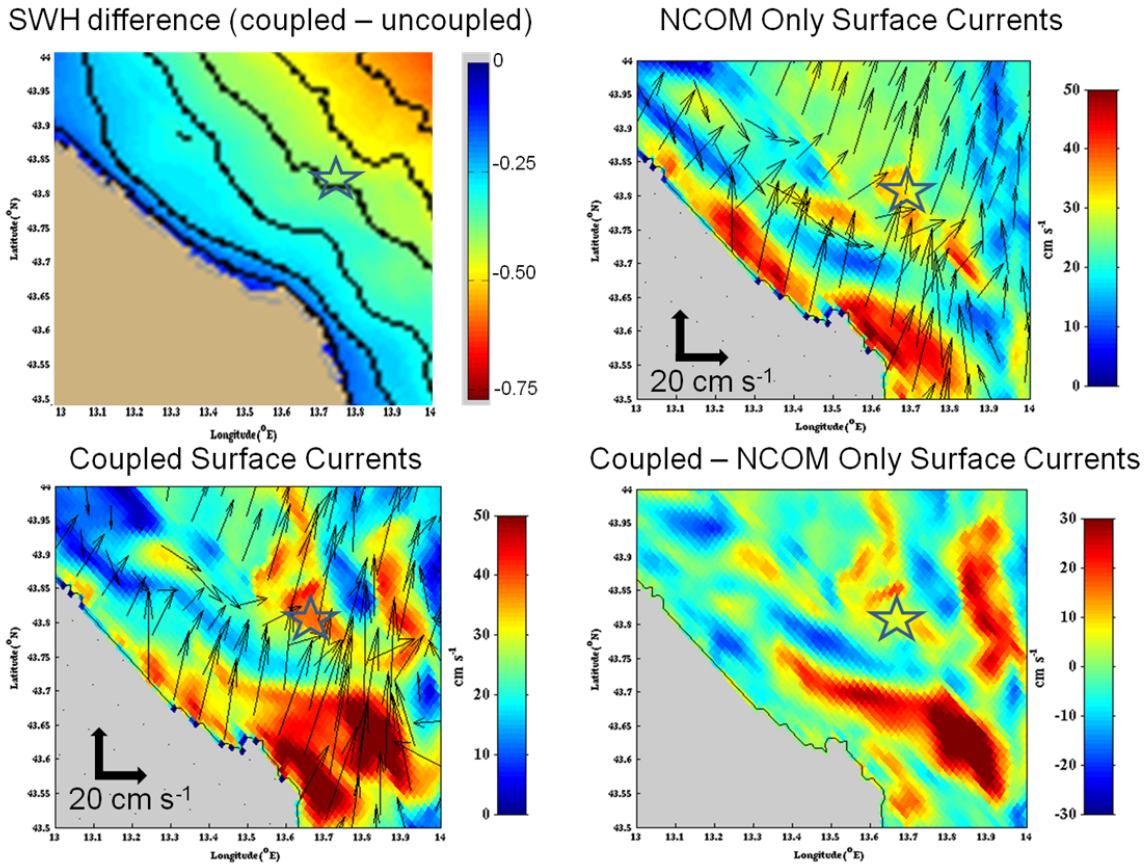

Figure 3.4-4: Mean SWH difference and mean surface currents for the period 15 February 1200 UTC to 16 February 0000 UTC 2006. The location of Ancona Mast is indicated by a star. Top left: Difference in mean SWH (m) between uncoupled and coupled model. Top right: Uncoupled (NCOM-only) mean surface current (m s^{-1}) and vectors. Bottom left: Coupled model mean surface current (m s-1) and vectors. Bottom right: The difference in the mean current surface speed between the uncoupled and coupled model.

Table 3.4-3: Significant wave height (SWH) statistics for ocean/wave coupled and uncoupled runs at Pescara for Feb 8-24, 2006.

Pescara (8-24 Feb 2006)	Mean (m)	MB (m)	CC	Std Dev.	RMSE (m)
Observed	0.68	~	~	0.35	~
Uncoupled (o2w=f, w2o=f)	0.75	0.07	0.66	0.34	0.29
One-way coupled (o2w=t, w2o=f)	0.77	0.09	0.73	0.28	0.26
Two-way coupled (o2w=t, w2o=t)	0.78	0.10	0.71	0.28	0.27

SWH comparisons of COAMPS to satellite altimeter data from bora events are shown in Figure 3.4-5. During the period of February-March 2006 there were two bora events resolved by the satellite altimeter data. GeoSat Follow-ON (GFO) captured a bora jet on February 5 over the central Adriatic Sea and ENVIronmental SATellite (ENVISAT) detected an event in the northern Adriatic Sea on March 13. Noting that the wind forcing is the same in both the one-way coupled and uncoupled simulations, the bora jets (peaks in wind speed) were resolved well; however, the magnitude of wind speed was higher in the COAMPS wind forcing, especially in the February 5 event. For both bora events, there was little statistical difference between the uncoupled and coupled simulations (Figure 3.4-6). Although the COAMPS wind forcing for these two periods was approximately 10-15 m/s in the bora jets, the effect of passing the NCOM currents and water levels to SWAN during the bora events appears to contribute little to the SWH for this particular dataset.

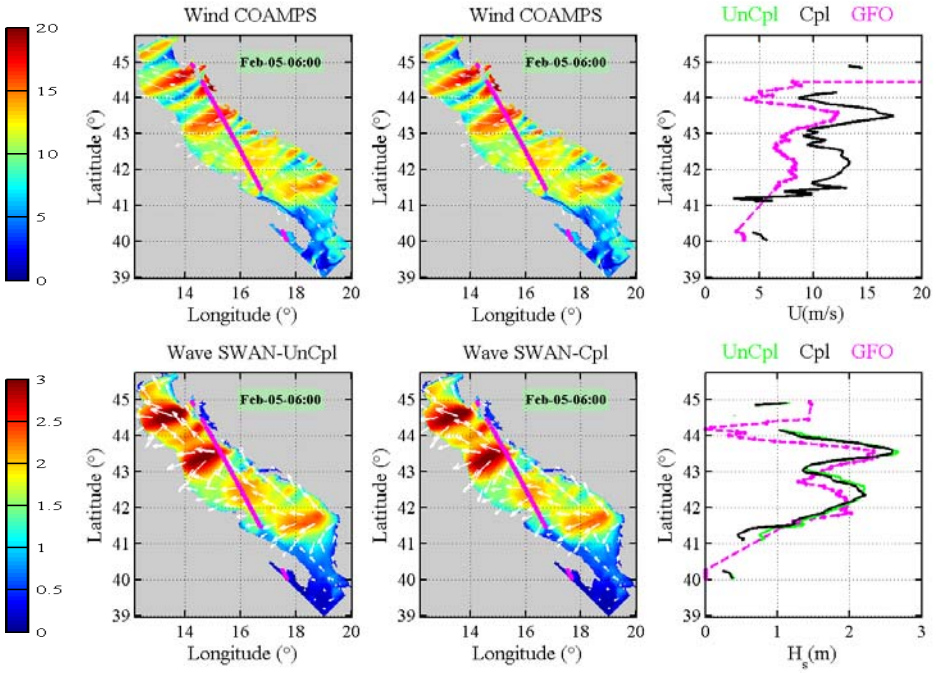

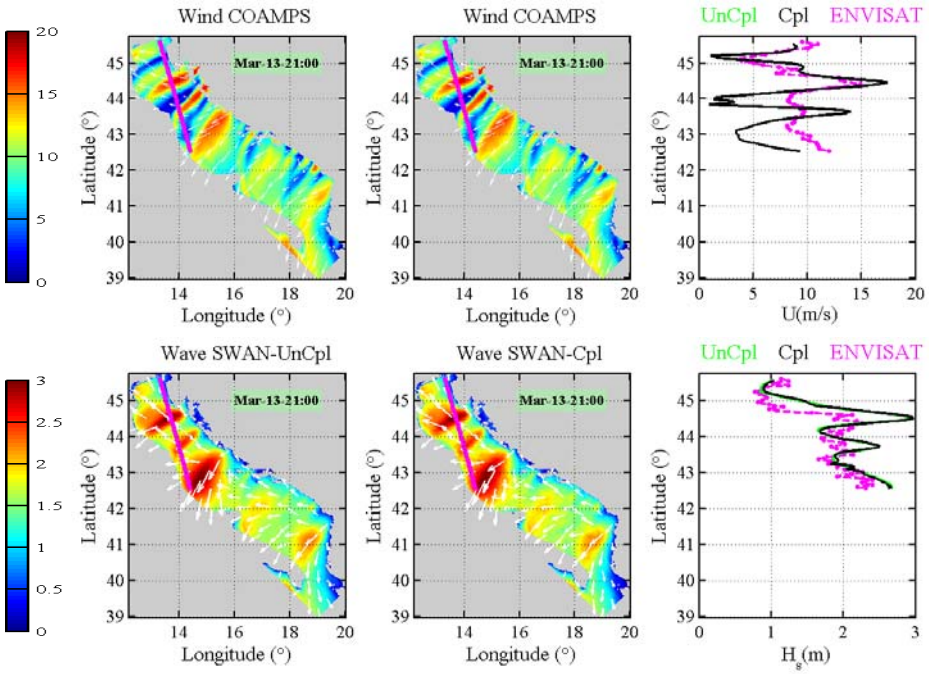

Figure 3.4-5: GFO and ENVISAT satellite altimeter passes for two Adriatic Sea bora events in February and March 2006. Uncoupled SWAN (top) and coupled COAMPS (bottom) simulations are shown. Higher significant wave heights are indicated by yellow, orange, and red.

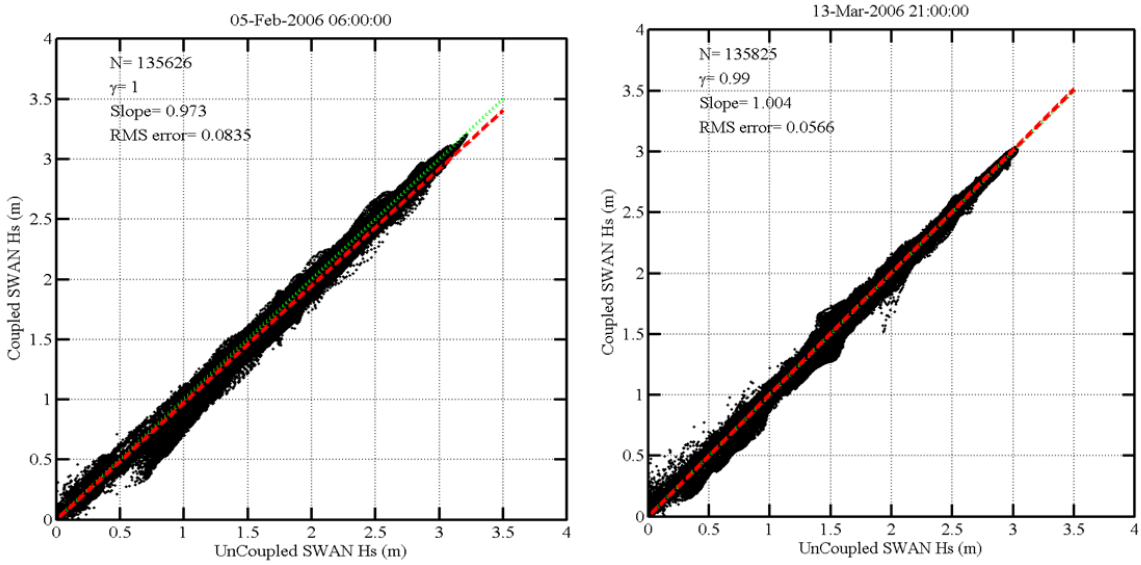

Figure 3.4-6: Scatter plot comparison of February (left) and March (right) 2006 coupled and uncoupled SWAN SWH.

3.4.4.3 Comparisons to DART drifters

COAMPS SSTs were compared to several drifters deployed during DART '06. Although tracers in NCOM are required to determine whether the model drifter track can be compared to the actual drifter track, a direct comparison of model to drifter track is shown in Table 3.4-4. Errors are expected to be larger with this type of comparison due to track errors between drifters and the model; however, a "ballpark" estimate still provides useful information. Seven DART drifters (06956, 14712, 33355, 44924, 44925, 44928, and 44930), with 6-hourly drifter observations, were compared to COAMPS SSTs.

The two drifters with the largest number of observations in March 2006 were numbered 06956 and 14712 (76 observations each). The mean SST bias for each drifter was less than 0.5°C, while the correlation coefficients (CCs) were 0.88 and 0.72, respectively. In general, the SST MB for six out of seven drifters was 0.5°C or less and the RMSE was less than 1°C (Table 3.4-4). The CCs were within an acceptable range for the drifters that had a greater number of observations. This may be due to less error in drifter tracks. However, for this type of comparison, the MB and RMSE values for each drifter comparison were sufficient to determine that the SSTs within the model domain were fairly accurate.

Table 3.4-4: Several drifters recorded SSTs and currents during DART '06 (March 2006). Overall the drifters agreed well when compared to COAMPS SSTs for the two-way ocean-wave coupled run. Observations were not compared to drifter track.

Drifter	Launch Date	N (6-hrly)	CC	RMSE	Mean Obs	Mean COAMPS	MB
06956	March 11	76	0.88	0.67	13.58	13.11	-0.47
14712	March 11	76	0.72	0.91	12.90	12.71	-0.19
33355	March 16	56	0.67	1.71	11.20	12.50	1.30
44924	March 16	56	0.86	0.74	13.80	13.30	-0.50
44925	March 19	32	0.45	0.80	13.50	13.02	-0.48
44928	March 23	24	0.22	0.57	13.91	13.87	-0.04
44930	March 23	24	0.40	0.46	14.08	13.79	0.28

4.0 TEST CASE SUMMARIES

4.1 Test Case One: Hurricane Ivan Summary

The COAMPS-TC model simulations for Hurricane Ivan showcased the state-of-the-art ESMF coupling of three independent models- the COAMPS atmospheric model, NCOM, and SWAN. The unique and comprehensive observational data set for Hurricane Ivan allowed for the evaluation of model performance based on the latest improvements of atmospheric, oceanic, and wave physics parameterization additions to COAMPS-TC. Overall, the model performance for Hurricane Ivan provided a very good study of the air-sea-wave interactions between the models, while gaining a better understanding of the primary effects of ocean-wave model coupling in high-wind conditions. The new wave input and dissipation parameterization (Babanin et al. 2010, Rogers et al. 2011) and wave drag coefficient formulation (Hwang 2011), based on field observational work, drastically improved SWAN wave properties in TC conditions. In addition, the exchange of ocean current information to SWAN further improved the TC wave field and reduced errors when compared to the classic SWAN Komen wave source terms and Wu drag coefficient formulation. Although SDC cannot be measured from the ADCPs in this study, it is more than likely that the SDC is non-negligible in such extreme TC conditions, near the surface. Further studies are necessary to truly gauge the effects of the Stokes' Drift Current on the upper-ocean mixing and current velocity in high wind conditions. Other components of wave to ocean coupling that were not examined here include bottom drag that is enhanced by wave action (Grant and Madsen 1979) and radiation stress gradients (Longuet-Higgins 1962, 1964). These may also play an important role in TC ocean-wave interaction.

4.2 Test Case Two: Okinawa Trough Summary

A wave-current interaction component in COAMPS was validated using satellite altimeter data in the Okinawa Trough and Kuroshio region during the 2007 typhoon season. Model predicted wind fields correlated well with satellite altimeter data. Coupling improved the wind magnitude slightly in terms of CC and RMSE, however, both uncoupled and coupled models tended to underestimate the wind speed. Wave heights also correlated well with the satellite altimeter data. A wave magnitude reduction in the presence of strong currents was also observed in the fully coupled scenario. Coupling also improved significant wave heights in terms of CC and RMSE. Both uncoupled and coupled models exhibited SST cooling at the typhoon's wake region, which was confirmed by the satellite derived SST fields. The coupled model showed stronger coastal upwelling than the uncoupled model. Surface current velocity fields showed some improvement in the coupled case based on drifter buoy analysis. Ocean-wave coupling also tended to enhance Kuroshio velocity and reduce coastal currents during strong wind (typhoon) events. More accurate representations of the SLD and related acoustic properties were the most significant improvements. This can be attributed to 1) more accurate temperature prediction due to air-ocean coupling, 2) incorporation of a wave model and better physics representation and 3) an improved vertical mixing turbulence scheme.

4.3 Test Case Three: Florida Straits Summary

A study of the impact of ocean currents on waves and wave impact on ocean currents was performed for the Florida Straits during the period of April 1 – May 15, 2005. The "ground truth" for wave model verification included in situ data (ADCP and buoy) and high frequency Wellen radar (WERA HF) data collected by the University of Miami. Comparisons of wave height, period and direction versus is situ data were generally very good, though some wave events were overpredicted by the model, most likely due to smaller than observed wave energy loss by refraction into the Florida coast because of limited resolution of bathymetry, and by small, directional errors in the spectral boundary forcing. Comparisons of wave heights at these locations with the inclusion of currents showed improvement as evidenced by lower RMSE, bias and higher correlation coefficients. Comparisons against WERA data showed that the inclusion of ocean currents improved the correlation coefficient at 77% of the sectors defined for both radar sites. Ocean currents from the coupled system were compared against WERA-derived ocean currents for a 77 day period from March 10 – May 25, 2005. Comparisons were mixed, with the current magnitudes from sectors A2, A3 and B1 and B3 having correlation coefficients higher than 0.5. The inclusion of waves modulates the Florida Current with differences in surface currents up to 0.5 m/s in daily averages. In the coastal region, where we had buoy observations, differences were found to be small.

4.4 Test Case Four: Adriatic Circulation Experiment (ACE) Summary

For the Adriatic Sea, little difference in SWH at the wave buoy locations was observed when ocean currents from NCOM were passed to SWAN compared to a standalone wave model run. During a bora event, the addition of the Stokes' drift current from SWAN to NCOM yielded only minor improvement at stations affected by higher winds. The passing of the wave radiation stress gradient from SWAN to NCOM provided marginally better NCOM results in coastal areas of the Adriatic Sea, but more analysis is necessary to determine the impacts of coupling in the Adriatic Sea.

5.0 CONCLUSION

Based on the validation results and findings, the following conclusions can be drawn:

- Ocean-wave coupling shows improvement and better model predictability in winds, waves, SST, currents, SLD and associated acoustic properties.
- It is necessary to implement two-way, ocean-to-wave and wave-to-ocean coupling, as we demonstrated that one-way coupling (current-to-wave only) results do not differ substantially from the uncoupled scenario.
- Current-wave model interaction showed substantial improvements in high-wind conditions.
- Overall, we found that the inclusion of currents in the SWAN hindcast studies improved the solution compared to uncoupled SWAN runs. However, we observed less impact on the surface currents when wave forcing was included. But the number of surface current observations used in this study was limited.

- The long-term test cases successfully demonstrated the capability of operational COAMPS and ESMF coupler functionality, both in model accuracy and system robustness for operational implementation.

6.0 OPERATIONAL IMPLEMENTATION

6.1 Suggestions for running the fully coupled COAMPS

Although COAMPS allows varying spatial resolution for the atmosphere, NCOM and SWAN models and the common grid, it is highly recommended that NCOM and SWAN share one common grid and projection without re-sampling.

Pay close attention to river mouths and channels (location, flux and grid size) as large SST diurnal cycles and sharp salinity gradients were found in those regions during the validation.
Investigate how and how much radiation stress and Stokes drift feed back to NCOM currents, as well as drag Cd and bottom roughness Zo specification.

It is suggested that one bathymetry file be used for NCOM (with 5 m minimum) and one for SWAN (with no minimum depth and more realistic slope) to improve model simulations of wave propagation and dissipation in the shallow regions. SWAN's feedback to currents is very sensitive to bathymetry (both gradient and depth), shoreline geometry, grid resolution, wind speed and directions, especially during hurricane forcing.

6.2 Resource Requirements

The computational time for the fully coupled COAMPS (for example, in the Okinawa Trough) is greater than that of the stand alone NCOM run due to the additional high resolution atmospheric and wave model components and the frequent coupling cycle.

- By experience, it is found that a fully coupled COAMPS model often requires a smaller time step than that required to prevent the CFL violation for the individual models, which increases computing time.
- The current decomposition and sweeping algorithm in the SWAN wave model limits the benefit of parallel processing. In this validation study, the number of CPUs in parallel runs is limited by the SWAN grid array size and orientation.
- By using a concurrent run, where atmosphere, ocean and wave models are run simultaneously on separate sets of processors, it is possible to run the fully coupled system using just a slightly increased computer wallclock time compared to a run of each of the individual model components.

6.3 Future Work

This VTR is a second in a series of Validation Test Reports for the ESMF-based COAMPS. Subsequent studies will investigate the impact of atmosphere-wave coupling and the fully coupled air-ocean-wave version of COAMPS5. A relocatable ice component will be added to

COAMPS beginning in FY13 (6.2 NRL Core funding). We anticipate validation studies for this new Arctic capability to begin in the FY15/16 timeframe.

This research is a continuation of an Office of Naval Research (ONR) sponsored National Oceanographic Partnership Program (NOPP) project that includes the Rosenstiel School of Marine and Atmospheric Science (RSMAS) at the University of Miami and the University of Rhode Island. We will examine wave-atmosphere model feedback and different NCOM ocean mixing schemes, including a new NCOM experimental scheme based on the Langmuir circulation and SDC mixing of Kantha and Clayson (2004) when the wave model is included. Turbulent mixing and upwelling studies in TCs due to SDC increasing near-surface vertical shear are also an important evaluation step in understanding ocean-wave model coupling. Future work in COAMPS-TC will continue to focus on the air-sea-wave parameterizations to improve TC track and intensity. Recent data obtained during the Impact of Typhoons on the Ocean in the Pacific (ITOP 2010) provided excellent ocean vertical temperature profiles for several TCs to evaluate SDC induced turbulence in NCOM.

7.0 ACKNOWLEDGEMENTS

This study was funded through the 6.2 NRL Core Project "Coupled Ocean-Wave Prediction System: Program Element #0602435N and the 6.2 ONR Tropical Cyclone NOPP Project. Thanks to Ed Walsh and Isaac Ginis of the University of Rhode Island for supplying the SRA data. Special thanks go to Sean Ziegeler of the User Productivity, Enhancement, Technology Transfer and Training (PETTT) group for technical assistance and to Luigi Cavaleri of the Marine Science Institute in Venezia, Italy, for providing wave buoy data for the DART '06 period. We acknowledge the insightful comments and suggestions made by the Validation Test Panel members Dr. Justin Small (NCAR), Dr. Paul Wittmann (FNMOC) and Dr. Jeikook Choi (NAVO).

We acknowledge Bill Teague and Ewa Jarosz of NRL for the ADCP data. Irina Yaremchuk, a Science and Engineering Apprenticeship Program (SEAP) summer student from Northshore High School in Slidell, LA, is also acknowledged for her data analysis. The WERA HF wave data was provided by Brian Haus from RSMAS and student involvement was made possible through the Navel Research Enterprise Internship Program. Leela Richman (NRL Student Temporary Employment Program) assisted by processing the WERA surface current data and generating graphics and comparisons for the Florida Straits test case.

The authors would like to thank David Wang and Jay Shriver at NRL for their assistance in satellite altimeter and drifter analysis. The authors also thank Pete Spence at Qinetiq NA for sonic layer depth computation and visualization. The authors thank Paul Martin for his helpful discussions concerning the implementation of wave forcing into NCOM and its effects on upper ocean mixing. The authors thank the review panel for their constructive suggestions and comments.

8.0 TECHNICAL REFERENCES

8.1 COAMPS Software Documentation

Allard, R.A., T.J. Campbell, T.A. Smith, T.G. Jensen, S. Chen, J.A. Cummings, J. Doyle, X. Hong, R.J. Small, and S.N. Carroll, (2010). Validation Test Report for the Coupled Ocean Atmosphere Mesoscale Prediction System (COAMPS) Version 5.0 NRL/MR/7322--10-9283. Oceanography Division, Naval Research Laboratory, Stennis Space Center, MS. 172 pp.

Chen, S., J. Cummings, J. Doyle, R.H. Hodur, T. Holt, C. Liou, M. Liu, A. Mirin, J. Ridout, J.M. Schmidt, G. Sugiyama, and W.T. Thompson, (2003). COAMPS Version 3 Model Description--General Theory and Equations. NRL/PU/7500--03-448, 145 pp.

Goerss, J., T. Hogan, K. Sashegvi, T. Holt, M. Rennick, T. Beeck, and P. Steinle, (2003). Validation Test Report for the NAVDAS/NOGAPS Data Assimilation System. Naval Research Laboratory, Monterey, CA. 26 pp.

Martin, P.J., C.N. Barron, L.F. Smedstad, A.J. Wallcraft, R.C. Rhodes, T.J. Campbell, C. Rowley, and S.N. Carroll, (2008a). Software Design Description for the Navy Coastal Ocean Model Version 4.0. NRL/MR/7320--08-9149, Oceanography Division, Naval Research Laboratory, Stennis Space Center, MS.

Martin, P.J., C.N. Barron, L.F. Smedstad, T.J. Campbell, A.J. Wallcraft, R.C. Rhodes, C. Rowley, T.L. Townsend, and S.N. Carroll, (2008b). User's Manual for the Navy Coastal Ocean Model (NCOM) Version 4.0. NRL/MR/7320--08-9151, Oceanography Division, Naval Research Laboratory, Stennis Space Center, MS.

Martin, P.J., (2000). A Description of the Navy Coastal Ocean Model Version 1.0. NRL Technical Report NRL/FR/7322-00-9962, 42 pp.

Smith, T.A., T.J. Campbell, R.A. Allard, and S.N. Carroll, (2012). User's Guide for the Coupled Ocean / Atmospheric Mesoscale Prediction System (COAMPS) Version 5.0., Rev. 2.0, NRL/MR/7320--12-9407, Oceanography Division, Naval Research Laboratory, Stennis Space Center, MS. 168 pp.

8.2 General Technical References

Ardhuin, F.A., B. Chapron, and T. Elfouhaily, (2004). Waves and the air-sea momentum budget: implications for ocean circulation modeling, *J. Phys. Oceanogr.* **34**: 1741-1755.

Ardhuin, F.A., A.D. Jenkins, K.A. Belibassakis, (2008). Comments on "The Three-dimensional current and surface wave equations", *J. Phys. Oceanogr.* **38**: 1340-1350.

Ardhuin, F., B. Chapron, F. Collard, (2009). Observation of swell dissipation across oceans. *Geophys. Res. Lett. 36*, L06607.

Ardhuin, F., E. Rogers, A. Babanin, J.-F. Filipot, R. Magne, A. Roland, A. van der Westhuysen, P. Queffeulou, J. M. Lefevre, L. Aouf, and F. Collard, (2010). Semi-

empirical dissipation source functions for ocean waves: Part I, definitions, calibration and validations. *J. Phys. Oceanogr.,* **40**: 1917-1941.

Babanin, A. V. and I. R. Young, (2005). Two-phase behaviour of the spectral dissipation of wind waves. Proc. Fifth Int. Symp. Ocean Waves Measurement and Analysis, Madrid, Spain, ASCE, 51.

Babanin, A.V., M.L. Banner, I.R. Young, and M.A Donelan, (2007a). Wave follower measurements of the wind input spectral function. Part 3. Parameterization of the wind input enhancement due to wave breaking. *J. Phys. Oceanogr.,* **37**: 2764-2775.

Babanin, A.V., K.N. Tsagareli, I.R. Young, D.J. Walker, (2010). Numerical Investigation of Spectral Evolution of Wind Waves. Part II: Dissipation Term and Evolution Tests, *J. Phys. Oceanogr*., **40**: 667-683.

Barron, C.N., A.B. Kara, P.J. Martin, R.C. Rhodes, and L.F. Smedstad, (2006). Formulation, implementation and examination of vertical coordinate choices in the Global Navy Coastal Ocean Model (NCOM). *Ocean Modelling*, **11**: 347-375.

Bidlot, J.-R., P. Janssen, S. Abdalla, (2007a). A revised formulation of ocean wave dissipation and its model impact. *ECMWF Tech. Rep. Memo. 509*, Reading, United Kingdom, 27 pp.

Blumberg, A.F. and G.L., Mellor, (1983). Diagnostic and prognostic numerical circulation studies of the South Atlantic Bight. *J. Geophys. Res.*, **88**: 4579-4592.

Blumberg, A.F. and G.L. Mellor, (1987). "A description of a three-dimensional coastal ocean circulation model." In: Three-Dimensional Coastal Ocean Models. N. Heaps, ed., American Union, New York, N.Y., p. 208.

Booij, N., R.C. Ris, and L.H. Holthuijsen, (1999). A third-generation wave model for coastal regions, Part I, Model description and validation, *J. Geophys. Res*., **104** (C4): 7649-7666.

Book, J.W., H. Perkins, R.P. Signell, and M. Wimbush, (2007). The Adriatic Circulation Experiment winter 2002/2003 mooring data report: A case study in ADCP data processing, NRL Memo. Rep. NRL/MR/7330-07-8999, U. S. Naval Res. Lab., Stennis Space Center, MS.

Caires, S. I. N. (2000). *Comparative study of HF radar measurements and wave model hindcasts of waves in shallow waters*, PhD thesis, U. Sheffield, 355 pp.

Cummings, J.A., (2005). Operational multivariate ocean data assimilation. *Q.J.R. Meteorol. Soc.,* **131**: 3583–3604.

Cummings, J. and S. Carroll, (2006). Software User's Manual for the Navy Coupled Ocean Data Assimilation (NCODA) System, *NRL Tech. Rpt.,* MRY-001-06, Naval Research Laboratory, Monterey, CA.

Daley, R. and E. Barker, (2000). *The NAVDAS Source Book*, Naval Research Laboratory Publication NRL/PJ/7530-01-441. NRL, Monterey, CA.

Daley, R. and E. Barker, (2001). NAVDAS—formulation and diagnostics. *Mon. Weather Rev.* **129**: 869–883.

Defant, F., (1951). Local winds, in Compendium of Meteorology, edited by T. F. Malone, Am. Meteorol. Soc., Boston, MA., pp. 655-672.

Donelan, M.A., A.V. Babanin, I.R. Young, and M.L. Banner, (2006). Wave follower measurements of the wind input spectral function. Part 2. Parameterization of the wind input. *Journal of Physical Oceanography*, **36**(8): 1672-1688

Doyle J., Y. Jin, R.M. Hodur, S. Chen, H. Jin, J.Moskaitis, A. Reinecke, P. Black, J. Cummings, E. Hendricks, T. Holt, C.-S. Liou, M. Peng, C. Reynolds, K. Sashegyi,

J. Schmidt, S. Wang, (2012). Real-Time tropical Cyclone Prediction Using COAMPS-TC. *Advances in Geosciences Taipei Review Volumes*. In press.

Egbert, G.D., and S.Y. Erofeeva, (2003). Efficient inverse modeling of barotropic ocean tides. *J. Atmos. Oceanic Tech*., 19, 183-204.

Fairall, C.W., E.F. Bradley, J.S. Godfrey, G.A. Wick, J.B. Edson and G.S. Young, (1996b). Cool-skin and warm layer effects on sea surface temperature. *J. Geophys. Res*., **101**: 1295-1308.

Fairall, C.W., E.F. Bradley, D.P. Rogers, J.B. Edson, and G.S. Young, (1996a). Bulk parameterization of air-sea fluxes for Tropical Ocean-Global Atmosphere Coupled-Ocean Atmosphere Response Experiment. *J. Geophys. Res.*, **101**: 3747-3764.Grant, W.D. and O.S. Madsen, (1979). Combined wave and current interaction with a rough bottom, *J. Geophys. Res.*, **84**: 1797-1808.

Fan, Y., I. Ginis, T. Hara, C.W. Wright, and E. J. Walsh, (2009). Numerical simulations and observations of surface wave fields under an extreme tropical cyclone. *J. Phys. Oceanogr*., **39**: 2097–2116.

Felizardo, F.C. and W.K. Melville, (1995). Correlations between ambient noise and the ocean surface wave field. *J. Phys. Oceanogr.,* **25**: 513-532

Fu, Q. and K.-N. Liou, (1993). Parameterization of the radiative properties of cirrus clouds. *J. Atmos. Sci.* **50** (13): 2008–2025.

GlobWave, http://www.globwave.org

Grant, W. D., and O. S. Madsen (1979). Combined wave and current interaction with a rough bottom, *J. Geophys. Res*., **84**(C4): 1797-1808.

Gravois, U.M., W.E. Rogers, T.G. Jensen, (2012). A Coupled Model System for Southeast Florida: Wave Model Validation Using Radar and In Situ Observations. *NRL Memorandum Report/7320—12-935.* 40pp.

Gurgel, K.W., G. Antonischki, H. Essen, T. Schlick, (1999). Wellen Radar (WERA): a new ground-wave HF radar for ocean remote sensing. *Coastal. Eng.* ,**37**(3-4): 219-234.

Harshvardhan, R. Davis, D.A. Randall, and T. G. Corsetti, (1987). A fast radiation parameterization for general circulation models. *J. Geophys. Res.*, **92:** 1009-1016.

Haus, B. K., P. A. Work, G. Voulgaris, N. K. Shay, R. Ramos and J. Martinez, (2010). Wind speed dependence of single-site wave-height retrievals from high-frequency radars, *J. Atm. and Oceanic Techn.*, **27:** 1381-1394.

Haus, B.K., (2007). Surface current effects on the fetch limited growth of wave energy, *Journal of Geophysical Res.*, **112**, C03003, doi:10.1029/2006JC003924.

Helber R.W., C. N. Barron, M. R. Carnes and R.A. Zingarelli (2008). Evaluating the sonic layer depth relative to the mixed layer depth. J. Geophys. Res. 113:C07033. Doi:10.1029/2007JC004595.

Hodur, R.M., (1997). The Naval Research Laboratory's Coupled Ocean/Atmosphere Mesoscale Prediction System (COAMPS). *Mon. Wea. Rev.,* **125**: 1414-1430.

Hogan, T., and T. Rosmond, (1991). The description of the Navy Operational Global Atmospheric Predictions System's spectral forecast model. *Mon.Wea. Rev.*, **119**: 1786-1815.

Hwang, P.A., (2011). A note on the ocean surface roughness spectrum. *J. Atmos Ocean Tech.* **28:** 436-443.

Jarosz, E., D.A. Mitchell, D.W. Wang, and W.J. Teague, (2007). Bottom-up determination of air-sea momentum exchange under a major tropical cyclone. *Science*, **315**: 1707-1709.

Jensen, T. G., W. E. Rogers, U. Gravois, T. Campbell and R. Allard, (2011). Wave -current interaction in the Florida Current in a coupled atmosphere-ocean-wave model. Oceans' 11, MTS-IEEE meeting, September 18-22, Kona, HI. Extended Abstract, 9pp.

Kain, J.S., and J.M. Fritsch, (1990). A One-Dimensional Entraining/Detraining Plume Model and Its Application in Convective Parameterization. *J of Atmos. Sci.,* **47:** 2784-2802.

Kantha LH, Clayson CA (2004). On the effect of surface gravity waves on mixing in the oceanic mixed layer. *Ocean Model* **6**:101–124.

Komen, G. J., S. Hasselmann, and K. Hasselmann, (1984) On the existence of a fully developed wind-sea spectrum, *J. Phys. Oceanogr*., **14:** 1271–1285.

Kundu, P.K., (1976). Ekman veering observed near the ocean bottom, *J. Phys. Oceanogr*., **6**: 238-242.

Kuzmic, M., I. Janekovic, J.W. Book, P.J. Martin, and J.D. Doyle, (2007). Modeling the northern Adriatic double-gyre response to intense bora wind: A revisit, *J. Geophys. Res*., **112**: C03S13, doi:10.1029/2005JC003377.

Large, W.G., J.C. McWilliams, and S.C. Doney, (1994). Oceanic vertical mixing: a review and a model with a nonlocal boundary layer parameterization. *Rev. Geophys.*, **32**: 363-403.

Longuet-Higgins, M.S. and R. W. Stewart, (1962). Radiation stresses and mass transport in surface gravity waves with application to ‘‘surf beats.’’ *J. Fluid Mech.,* **13:** 481–504.

Longuet-Higgins, M.S. and R.W. Stewart, (1964). Radiation stresses in water waves; a physical discussion, with applications, *Deep-Sea Res.*, **11**: 529-562.

Louis, J.F., (1979). A parametric model of vertical eddy fluxes in the atmosphere. *Bound. Layer Meteor*., **17**: 187-202.

Martin, P.J., G. Peggion, and K.J. Yip, (1998). “A comparison of several coastal ocean models.” NRL Report NRL/FR/7322--97-9692. Naval Research Laboratory, Stennis Space Center, MS., pp. 96.

McWilliams, J. C., P. P. Sullivan, and C.-H. Moeng, (1997). Langmuir turbulence in the ocean, *J. Fluid Mech.*, **334**: 1–30.

Mellor, G.L. and T. Yamada, (1982). Development of a turbulence closure model for geophysical fluid problems. *Rev. Geophys.,* **20** (4): 851-875.

Moon, I.-J., I. Ginis, and T. Hara, (2004b). Effect of surface waves on air-sea momentum exchange. Part II: Behavior of drag coefficient under tropical cyclones, *J. Atmos. Sci*., **61**: 2334– 2348.

Perkins, H.T., F. de Strobel, and L. Gualdesi, (2000). The Barny Sentinel Trawl-resistant ADCP bottom mount: Design, testing, and application, *IEEE J. Oceanic Eng*., **25**: 430-436.

Powell, M.D., P.J. Vickery, and T.A. Reinhold (2003). Reduced drag coefficient for high wind speeds in tropical cyclones. *Nature*, **422**: 279-283.

Powell, M.D., Ginis, I., 2006. Drag coefficient distribution and wind speed dependence in tropical cyclones. NOAA HRD-AOML report. 5 pp.

Pullen, J., J.D. Doyle, T. Haack, C. Dorman, R.P. Signell, and C.M. Lee, (2007). Bora event variability and the role of air-sea feedback, *J. Geophys. Res*., **112**: C03S18.

Ramos, R. H. C. Graber, B. K. Haus, (2009). Observation of wave energy evolution in coastal areas using HF radar. *J. Atm. and Oceanic Techn.*, **26**:1891-1909.

Rogers, W.E., A.V. Babanin, and D.W. Wang, (2011). Observation-consistent input and whitecapping-dissipation in a model for wind-generated surface waves: Description and simple calculations, *J. Atm. and Ocean Tech.,* (in press).

Rogers, W.E., J.M. Kaihatu, L. Hsu, R.E. Jensen, J.D. Dykes, K.T. Holland, (2007). Forecasting and hindcasting waves with the SWAN model in the Southern California Bight. *Coastal Eng.* **54**: 1-15.

Rogers, W.E., P.A. Hwang and D.W. Wang, (2003). Investigation of wave growth and decay in the SWAN model: three regional-scale applications, *J. Phys. Oceanogr*., **33**: 366-389.

Rutledge, S.A., and P.V. Hobbs, (1983). The mesoscale and microscale structure and organization of clouds and precipitation in midlatitude cyclones. Part VIII: A Model for the "seeder-feeder" process in warm-frontal rainbands. *J. Atmos. Sci.*, **40**: 1185-1206.

Sanford, T.B., J.F. Price, and J.B. Girton, (2011). Upper-Ocean Response to Hurricane Frances (2004) Observed by Profiling EM-APEX Floats. *J. Phys. Oceanogr.*, **41:** 1041–1056.

Shay, L. K. J. Martinez-Pedraja, T.M. Cook, and B.K. Haus, (2007). High-frequency radar mapping of surface currents using WERA. *J. Atm. Oceanic. Tech.*, **24:** 484-503.

Shay, L. K. H. Seim, D. Savidge, R. Styles, R. H. Weisberg, (2008). High frequency radar observing systems in SEACOOS: 2002-2007 lessons learned, *Marine Technology Society Journal,* **42**(3): 55-670.

Smith, S., J.A. Cummings, C. Rowley, P. Chu, J. Shriver, R. Helber, P. Spence, S. Carroll, and O. M. Smedstad, (2011). Validation test report for the Navy coupled ocean data assimilation 3D variational analysis (NCODA-VAR) system, version 3.43. NRL/MR/7320--11-9363, Oceanography Division, Naval Research Laboratory, Stennis Space Center, MS.

Snaith, H., G. Busswell, H. Sheera, F. Collard, J. Piollé, P. Queffeulou, Y. Quilfen, E. Ash, D. Cotton, D. Carter, D. Poulter, and I. Williams, (2010). GLOBWAVE: A new generation of satellite wave products, *Proceedings of OceanObs'09: Sustained Ocean Observations and Information for Society*, Venice, Italy, 21-25 September 2009, ESA Publication.

SWAN TEAM. (2006). SWAN User Manual version 40.51. Department of Civil Engineering and Geosciences, Delft university of Technology, Delft, The Netherlands, 111 pp.

Tang, C. L., W. Perrie, A. D. Jenkins, B. M. DeTracey, Y. Hu, B. Toulany, and P. C. Smith, (2007). Observation and modeling of surface currents on the Grand Banks: A study of the wave effects on surface currents, *J. Geophys. Res.*, **112**: C10025, doi:10.1029/2006JC004028.

Teague, W. J., E. Jarosz, D. W. Wang, D. A. Mitchell, (2007). Observed Oceanic Response over the Upper Continental Slope and Outer Shelf during Hurricane Ivan. *J. Phys. Oceanogr.*, **37**: 2181–2206.

Tolman, H.L., and D. Chalikov, (1996). Source terms in a third-generation wind-wave model. *J. Phys. Oceanogr*, **26**: 2497-2518.

Tsagareli, K. N., (2009). Numerical investigation of wind input and spectral dissipation in evolution of wind waves. PhD Thesis, The University of Adelaide, South Australia, 219p.

Tsagareli, K.N., A.V. Babanin, D.J. Walker, and I.R. Young, (2010). Numerical investigation of spectral evolution of wind waves. Part 1. Wind input source function. *J. Phys. Oceanogr.,* **40**(4): 656-666.

Voulgaris, G., Haus, B. K., P. Work, L. K. Shay, H. Seim, R. H. Weisberg and J. R. Nelson, (2008). Waves initiative within SEACOOS, *Mar. Tech. Soc. J.*, **42**(3): 68-80.

WAMDI Group, (1988). The WAM model- A third generation ocean wave prediction model. *J. Phys. Oceanogr*., **18**: 1775-1810.

Wright, C. W., Walsh, E. J., Vandemark, D., Krabill, W. B., Garcia, a. W., Houston, S. H., Powell, M. D., Black, P. G., Marks, F. D., (2001). Hurricane directional wave spectrum spatial variation in the open ocean. *J. Phys. Oceanogr.*, **31**: 2472–2488.

Wyatt, L. R., S. P. Thompson, and R. R. Burton, (1999). Evaluation of high frequency radar wave measurement. *Coastal Eng.*, **37**: 259-282.

Wyatt, L. R., and Coauthors, (2003). Validation and intercomparisons of wave measurements and models during the EuroROSE experiments. *Coastal Eng.*, **48**: 1-28.

Wu, J., (1980). Wind-stress coefficients over sea surface near neutral conditions: A revisit. *J. Geophys. Res.,* **10**: 727-740.

Young, I.R., M.L. Banner, M.A. Donelan, A.V. Babanin, W.K. Melville, F. Veron, and C. McCormick, (2005). An integrated study of the wind wave source term balance in finite depth water. *J. Atmos. Oceanic Technol.*, **22**: 814-828.

Young, I.R., and A.V. Babanin, (2006). Spectral distribution of energy dissipation of wind-generated waves due to dominant wave breaking. *J. Phys. Oceanogr.*, **36**(3): 376–394.

9.0 NOTES

9.1 Acronyms and Abbreviations

Acronym	Description
3D-VAR	Three-dimensional VARiational data assimilation
ACE	Adriatic Circulation Experiment
ADCP	Acoustic Doppler Current Profiler
AMSR-E	Advanced Microwave Scanning Radiometer-Earth Observing System
AUV	Autonomous Underwater Vehicle
AVHRR	Advanced Very High Resolution Radiometer
BHcpl	Babanin-Hwang NCOM/SWAN coupled simulation
BHunc	Babanin-Hwang NCOM/SWAN uncoupled simulation
CAAPS	Centralized Atmospheric Analysis and Prediction System
CAGIPS	Come and Get It Product Server
CC	Correlation Coefficient
CCC	Complex Correlation Coefficient

Acronym	Description
CDN	Crandon Park
CLIVAR	Climate Variability and Predictability
CMAN	Coastal-Marine Automated Network
COAMPS	Coupled Ocean and Atmosphere Mesoscale Prediction System
COAMPS-OS	Coupled Ocean and Atmosphere Mesoscale Prediction System- On Scene
COAMPS-TC	Coupled Ocean and Atmosphere Mesoscale Prediction System-Tropical Cyclone
CODAR	Coastal Ocean Dynamics Applications Radar
CPIES	Current-Pressure-Inverted-Echo-Sounders
CTD	Conductivity, Temperature and Depth
DART	Dynamics of the Adriatic in Real-Time field experiment
DBDB2, V	Digital Bathymetric Database, resolution 2 min, Variable resolution
DEM	Digital Elevation Model
DoE	Department of Energy
EAS	East Asian Seas
ENVISAT	ENVIronmental SATellite
ERS-2	European Remote Sensing satellite
ESMF	Earth System Modeling Framework
FC	Florida Current
FMCW	Frequency Modulated Continuous Wave
FNMOC	Fleet Numerical Meteorology and Oceanography Center
GDEM	Global Digital Elevation Map
GFO	GeoSat Follow-On
GNCOM	Global Navy Coastal Ocean Model
GOES	Geostationary Operational Environmental Satellite
GOFS	Global Ocean Forecasting System
GOM	Gulf of Mexico
GVC	General Vertical Coordinate
HF	High Frequency
HPC	High Performance Computing
HWRF	Hurrican Weather Research and Forecast system
I/O	Input/Output
IC	Inshore Countercurrent
ITOP 2010	Impact of Typhoons on the Ocean in the Pacific 2010
JAMSTEC	Japan Agency for Marine-Earth Science and Technology
JKEO	JAMSTEC Kuroshio Extension Observatory buoy
JRP	Joint Research Project
JONSWAP	Joint North Sea Wave Analysis Project

Acronym	Description
KEO	Kuroshio Extension Observatory
KESS	Kuroshio Extension System Study
KWunc	Komen-Wu NCOM/SWAN UNCoupled simulation
LBC	Lateral Boundary Condition
LCs	Langmuir cells
MB	Mean Bias
ME	Mean Error
MDE	Mean Directional Error
MLD	Mixed Layer Depth
MODAS	Modular Ocean Data Assimilation System
MVOI	Multi-variate Optimum Interpolation
MWPD	Mean Wave Propagation Direction
MYL2/2.5	Mellor-Yamada (vertical mixing) Level 2/2.5
NASA	National Aeronautics and Space Administration
NAVDAS	NRL Atmospheric Variational Data Assimilation System
NCAR	National Center for Atmospheric Research
NCEP	National Centers for Environmental Prediction
NCODA	Navy Coupled Ocean Data Assimilation
NCOM	Navy Coastal Ocean Model
NDBC	National Data Buoy Center
NKL	North Key Largo Hammocks Biological Reserve
NNE	North-northeast
NOAA	National Oceanic and Atmospheric Administration
NOGAPS	Navy's Operational Global Atmospheric Prediction System
NOPP	National Oceanographic Partnership Program
NOS	National Ocean Service
NRL	Naval Research Laboratory
NURC	NATO Undersea Research Centre
OAFlux	Object Analyzed Air-Sea Fluxes
ODAS	Ocean Data Acquisition System
ONR	Office of Naval Research
OSU	Oregon State University
PBL	Planetary Boundary Layer height
PETTT	Productivity, Enhancement, Technology Transfer and Training
POM	Princeton Ocean Model
QuikSCAT	Quick Scatterometer
RELO NCOM	RELOcatable NCOM
R/V	Research Vessel

Acronym	Description
RMSE	Root Mean Square Error
RSMAS	Rosenstiel School of Marine and Atmospheric Sciences
S	Salinity
SDC	Stokes Drift Current
SDD	Software Design Description
SEACOOS	SouthEast Atlantic Coastal Ocean Observing System
SEAP	Science and Engineering Apprenticeship Program
SeaWiFS	Sea-viewing Wide Field-of-view Sensor
SEPTR	Shallow-water Environmental Profiler in Trawl-safe, Real-time configuration
SFSU	San Francisco State University
SLD	Sonic Layer Depth
SRA	Scanning Radar Altimeter
SRTM	Shuttle Radar Topography Mission
SSH (A)	Sea Surface Height (Anomaly)
SSM/I	Special Sensor Microwave/Imager
SST	Sea Surface Temperature
SWANd	SWAN displaced
SWAN	Simulating WAves Nearshore
SWH	Significant Wave Height
SZM	Sigma/Z-level Model
T	Temperature
T/ P	TOPEX/Poseidon
TC	Tyrrhenian Current
TMI	TRMM Microwave Imager
TRBM	Trawl Resistant Bottom Mounts
TRMM	Tropical Rainstorm Measuring Mission
UTC	Coordinated Universal Time
VTR	Validation Test Report
WAC	Western Adriatic Current
WERA	Wellen Radars
WHOI	Woods Hole Oceanographic Institution
WOCE	World Ocean Circulation Experiment
WVS	Water Vapor Scaling
WW3	WaveWatch III